

UC Davis

Technical Memoranda

Title

Thin Concrete Overlay on Asphalt Pilot Project at Woodland SR 113: Initial Performance

Permalink

<https://escholarship.org/uc/item/4vj060rv>

Authors

Mateos, Angel

Harvey, John

Millan, Miguel Angel

et al.

Publication Date

2023-05-01

DOI

10.7922/G26D5R9B

# Thin Concrete Overlay on Asphalt Pilot Project at Woodland SR 113: Initial Performance

**Authors:**

Angel Mateos, John Harvey, Miguel Angel Millan, Fabian Paniagua, and Shuo Yang

Partnered Pavement Research Center (PPRC) Strategic Plan Element 3.54:  
Monitoring Performance of Concrete Overlay Projects (DRISI Task 3812)

---

**PREPARED FOR:**

California Department of Transportation  
Division of Research, Innovation, and System Information  
Office of Materials and Infrastructure

**PREPARED BY:**

University of California  
Pavement Research Center  
UC Davis, UC Berkeley





# TECHNICAL REPORT DOCUMENTATION PAGE

1. REPORT NUMBER UCPRC-TM-2023-01	2. GOVERNMENT ASSOCIATION NUMBER	3. RECIPIENT'S CATALOG NUMBER
4. TITLE AND SUBTITLE Thin Concrete Overlay on Asphalt Pilot Project at Woodland SR 113: Initial Performance		5. REPORT PUBLICATION DATE May 2023
		6. PERFORMING ORGANIZATION CODE
7. AUTHOR(S) Angel Mateos (ORCID 0000-0002-3614-2858) John Harvey (ORCID 0000-0002-8924-6212) Miguel Angel Millan (ORCID 0000-0002-9116-9076) Fabian Paniagua (ORCID 0000-0002-2385-4899) Shuo Yang (ORCID 0000-0002-2653-5199)		8. PERFORMING ORGANIZATION REPORT NO. UCPRC-TM-2023-01 UCD-ITS-RR-23-60
9. PERFORMING ORGANIZATION NAME AND ADDRESS University of California Pavement Research Center Department of Civil and Environmental Engineering, UC Davis 1 Shields Avenue Davis, CA 95616		10. WORK UNIT NUMBER
		11. CONTRACT OR GRANT NUMBER 65A0788
12. SPONSORING AGENCY AND ADDRESS California Department of Transportation Division of Research, Innovation, and System Information P.O. Box 942873 Sacramento, CA 94273-0001		13. TYPE OF REPORT AND PERIOD COVERED Technical Memorandum September 2018 to December 2020
		14. SPONSORING AGENCY CODE
15. SUPPLEMENTAL NOTES doi:10.7922/G26D5R9B		
16. ABSTRACT This report presents the initial performance of the Woodland SR 113 thin concrete overlay on asphalt (COA) project built in 2018-2019. The project comprises approximately four miles of a two-lane highway. The COA had 6 ft. transverse joint spacing, a slab thickness of 6 in., and an asphalt base that was overall in very poor condition. The performance of the project between the date of construction and October 2020 is presented in this report. The performance was evaluated by different means, including periodic visual inspections and longitudinal profiler evaluations; falling weight deflectometer (FWD) testing; real load testing (RLT), where the concrete strains under truck loading were recorded; and continuous monitoring of slab temperatures and drying shrinkage deformations. Overall, the project performed as expected. Visual inspection of the COA did not indicate any cracking, faulting, or other structural distress. FWD and RLT evaluations indicate that the COA structure has remained stable since the construction. While the smoothness varied considerably during the period evaluated in this report, the variation was caused by changes in slab curvature due to thermal gradients through the slab depth and concrete drying shrinkage.		
17. KEY WORDS rigid pavement, thin bonded concrete overlay on asphalt, thin whitetopping, rapid-strength concrete, rubberized asphalt, pavement rehabilitation		18. DISTRIBUTION STATEMENT No restrictions. This document is available to the public through the National Technical Information Service, Springfield, VA 22161
19. SECURITY CLASSIFICATION (of this report) Unclassified	20. NUMBER OF PAGES 97	21. PRICE None

Reproduction of completed page authorized

## UCPRC ADDITIONAL INFORMATION

<p>1. DRAFT STAGE Final</p>	<p>2. VERSION NUMBER 1</p>				
<p>3. PARTNERED PAVEMENT RESEARCH CENTER STRATEGIC PLAN ELEMENT NUMBER 3.54</p>	<p>4. DRISI TASK NUMBER 3812</p>				
<p>5. CALTRANS TECHNICAL LEAD AND REVIEWER(S) Dulce Rufino Feldman</p>	<p>6. FHWA NUMBER CA243812A</p>				
<p>7. PROPOSALS FOR IMPLEMENTATION Several recommendations for implementation are included in section 9.3 of this report.</p>					
<p>8. RELATED DOCUMENTS Mateos, A., Harvey, J.T., Millan, M.A., Wu, R., Paniagua, F., Cisneros, J. and Paniagua, J. 2021. <i>Concrete Overlay on Asphalt Pilot Project at Woodland SR 113: Construction</i> (Research Report: UCPRC-RR-2020-01). Davis and Berkeley, CA: University of California Pavement Research Center.</p>					
<p>9. LABORATORY ACCREDITATION The UCPRC laboratory is accredited by AASHTO resource and CCRL for the laboratory testing discussed in this report.</p>	 				
<p>10. SIGNATURES</p>					
<p>A. Mateos <b>FIRST AUTHOR</b></p>	<p>J.T. Harvey <b>TECHNICAL REVIEW</b></p>	<p>C. Fink <b>EDITOR</b></p>	<p>J.T. Harvey <b>PRINCIPAL INVESTIGATOR</b></p>	<p>D.R. Feldman <b>CALTRANS TECH. LEADS</b></p>	<p>T.J. Holland <b>CALTRANS CONTRACT MANAGER</b></p>

Reproduction of completed page authorized

## DISCLAIMER

---

This document is disseminated in the interest of information exchange. The contents of this report reflect the views of the authors who are responsible for the facts and accuracy of the data presented herein. The contents do not necessarily reflect the official views or policies of the State of California or the Federal Highway Administration. This publication does not constitute a standard, specification or regulation. This report does not constitute an endorsement by the Department of any product described herein.

For individuals with sensory disabilities, this document is available in alternate formats. For information, call (916) 654-8899, TTY 711, or write to California Department of Transportation, Division of Research, Innovation and System Information, MS-83, P.O. Box 942873, Sacramento, CA 94273-0001.

## ACKNOWLEDGMENTS

---

The authors of this report would like to thank Caltrans District 3 personnel for the support they provided for the instrumentation, construction monitoring, and initial performance evaluation of the Woodland SR 113 thin concrete overlay on asphalt project. The support provided by Resident Engineer Garrett Griffith and Woodland Maintenance Facility Supervisor Toni Romero is appreciated. The authors would also like to thank the Southwest Concrete Pavement Association. This association—and, in particular, Executive Director Charles Stuart—provided continuous support for the design and construction of the Woodland thin COA pilot. The authors would also like to thank the California Nevada Cement Association—in particular, Tom Tietz, Clay Slocum, and Nathan Forrest—for the support and technical advice provided. Similar appreciation is extended to James Mack (ACPA and Cemex) for the highly valuable technical inputs. The Caltrans technical review, led by Dulce Rufino Feldman of the Office of Concrete Pavement, and the oversight by Joe Holland of the Division of Research, Innovation and System Information (DRISI) are highly appreciated. The help that UCPRC staff and students provided in instrumenting the sections and in the monitoring and quality control of the construction is also acknowledged.

## PROJECT OBJECTIVES

---

The primary goal of Partnered Pavement Research Center (PPRC) Projects 3.39 and 3.54 is to evaluate the implementation and early field performance of thin concrete overlay on asphalt (COA) pilot projects. The investigation has two specific goals: (1) to help identify how well this treatment works under different climate, traffic, and site conditions and (2) to identify the best practices and standards for the climate, materials, and construction work zone practices in the Caltrans road network. The study's main goal will be achieved by completing the following tasks:

1. Document the site conditions and construction of the thin COA projects, and set a baseline for evaluation of the future performance of the projects.
2. Gather information about the experience of others, including Caltrans staff and contractors, involved in thin COA design and construction. This task includes the identification of any potential design and construction problems associated with the use of this technology in California.
3. Monitor the initial performance of the thin COA pilot projects.
4. Evaluate the technology choices that could not be evaluated in PPRC Strategic Plan Element (SPE) Project 4.58B (Development of Improved Guidelines and Designs for Thin Whitetopping).

Tasks 1 and 2 above were covered in a previous report, *Concrete Overlay on Asphalt Pilot Project at Woodland SR 113: Construction* (UCPRC-RR-2020-01). This report documents the construction and instrumentation of the thin COA pavement pilot project on State Route (SR) 113 in Woodland, California.

The work presented in this report covers Task 3. The initial performance of the SR 113 thin COA pilot is evaluated in terms smoothness, surface macrotexture, and structural capacity determined using the falling weight deflectometer and under traffic loading. The evaluation is supported by results from a limited coring campaign whose main goal was to determine the status of transverse joint deployment and slab-base bonding.

## EXECUTIVE SUMMARY

---

This report presents the initial performance of the Woodland SR 113 thin concrete overlay on asphalt (COA) project. The project comprises approximately four miles of a two-lane road. The north part of the project, referred to as Segment B (PM 14.760 to PM 17.580), was built in October and November 2018, and the south part, referred to as Segment A (PM 11.860 to PM 12.890), was built in April and May 2019. The monitoring of the construction of the project revealed no major design or construction issues with the concrete overlay, but it did show that the condition of the asphalt base was very poor, particularly on the north part of the project.

The thin COA has 6 ft. transverse joint spacing. The inner slabs are 6×6 ft. while the outer slabs are 6×8 ft. and provide a 2 ft. wide concrete shoulder. While the slab design thickness is 6 in., the actual slab thickness in Segment B is 1 to 3 in. thicker than the 6 in. target.

The average annual daily truck traffic (AADTT) of Segment A is around 570 (two-way), and the AADTT of Segment B is around 240. The Woodland climate is close to Mediterranean, with hot, dry summers and relatively mild, wet winters.

The performance of the project between construction and October 2020 is presented in this report. The performance was evaluated by different means:

- Periodic measurement of the smoothness with a laser inertial profiler.
- Periodic measurement of the surface macrotexture with a laser texturometer.
- Falling weight deflectometer (FWD) testing conducted on three occasions: August 2019, January 2020, and August 2020.
- Real load testing (RLT) conducted on three occasions, the same time as the FWD testing. The RLT consisted of monitoring of the strain that a truck with known axles weights produced in the COA.
- Continuous monitoring of the COA temperature by means of thermocouples installed at different depths in the concrete slabs and in the asphalt base.

- Continuous monitoring of the concrete strain caused by the hydrothermal actions (temperature changes and drying shrinkage).

The main conclusion from the evaluation of the initial performance of the SR 113 thin COA is that no structural damage has taken place. This conclusion is supported by the following findings:

- Visual inspection of the COA did not indicate any cracking, faulting, or any other structural distress.
- While the smoothness varied considerably during the period evaluated in this report, the variation was caused by changes in slab curvature due to thermal gradients through the slab depth and concrete drying shrinkage.
- FWD deflections and load transfer efficiency (LTE) remained stable between the August 2019 and August 2020 evaluations.
- The structural response of the COA under truck loading remained stable between the August 2019 and August 2020 evaluations.

Other important conclusions from the initial evaluation of SR 113 thin COA performance include the following:

- The visual inspection did not find any material-related distress.
- The visual inspection did not find slab migration.
- The smoothness of the concrete overlay indicates high diurnal and seasonal variations. The diurnal variation was caused by changes in slab curvature due to thermal gradients, and the seasonal variation was caused by changes in slab curvature due to concrete drying shrinkage.
  - The International Roughness Index (IRI) changed up to 40 in./mi during a 24-hour period.
  - The IRI changed close to 60 in./mi during one year.
  - Calculations based on *ProVAL* and slab curvature measurements with vibrating wire strain gauges (VWSGs) correspond with the high diurnal and seasonal variations of the IRI measured in the SR 113 thin COA.
- The differential drying shrinkage (top versus bottom of the slab) reached very high values, up 800  $\mu\epsilon$ , in the Woodland COA slabs. Considering that the coefficient of thermal expansion (CTE)



of the concrete (under saturated conditions, AASHTO T 336) was  $5.2 \mu\epsilon/^\circ\text{F}$ , the equivalent linear temperature difference (ELTD) that matches such differential shrinkage is  $150^\circ\text{F}$ .

- The strain measured with VWSGs in the SR 113 thin COA slabs indicates that the slabs are restricted from expanding in the longitudinal direction during the warm periods. The restriction was more severe during the second summer (2020) than during the first summer (2019).
- The surface macrotexture, quantified as mean profile depth (MPD), was around 23 mils after the construction of the concrete overlay, which was later textured with longitudinal tining. The macrotexture increased to around 30 mils after the blanket grinding and then decreased slowly due to the traffic action.
- The LTE of the transverse joints showed a clear high-low pattern with alternating joints with good and poor LTE.
  - While the LTE of the joints with good performance remains stable over 80%, the LTE of the joints with poor performance shows a strong seasonal variation and the LTE is highly affected by the mean temperature of the slabs.
  - Around 30% of the joints with poor performance show less than 70% LTE during the winter evaluation.
  - The LTE high-low pattern is partly related to the lack of deployment of some transverse joints.
  - FWD testing, complemented with visual inspection and coring, indicates that around 80% of the transverse joints deployed. The joints seemed to deploy soon after the overlay construction, and FWD testing suggests that no further transverse joint deployment occurred after the first summer.
  - The lack of transverse joint deployment is partly related to the low ratio of saw-cut depth to slab thickness, attributable to the extra thickness of the slab above the design thickness and a relatively shallow cut. The coring conducted at three locations indicates that the ratio was between 0.22 and 0.25 (smaller than the one-third target).
  - In addition to the lack of deployment of some transverse joints, the LTE high-low pattern seems to be related to a more general phenomenon: the presence of dominant joints

that absorb the opening of the adjacent joints (deployed or not deployed). Because of its larger opening, a dominant joint would show smaller LTE than the adjacent joints.

- Visual inspection of the initial transverse joint deployment indicates that the dominant joints deployed earlier than the adjacent joints.
- While the northbound and southbound lanes were paved on different days, the location of the dominant joints in the two lanes match. The matching indicates that the opening and closing of the first-paved lane transverse joints triggered the deployment of the second-paved lane transverse joints.
- FWD testing and RLT do not indicate differences between the SR 113 sections other than slightly smaller deflections in Segment B compared to Segment A, due to its higher slab thickness. However, both FWD testing and RLT indicate statistically significant differences between joints with good and poor LTE.
- The analysis of the strain measured in SR 113 thin COA sections under RLT indicates that the COA structure is performing as expected, considering the LTE high-low pattern and the lack of deployment of some of the transverse joints. Based on the measured strain, the LTE of the joints with poor LTE is much lower than the LTE measured with the FWD at the same joints.
- The analysis of the RLT strain data indicates that the structural contribution of the asphalt base bonded to the concrete slab is very little. On average, the absolute value of the strain measured under track loading at the bottom of the slabs is 83% of the absolute value of the strain measured at the top of the slabs.
- Visual examination of cores, supported with the analysis of the RLT strain data, indicates that debonding occurred at the transverse joints with poor LTE. The debonding extended around 10 to 20 in. away from the transverse joints regardless of the type of asphalt base. In the sections with rubberized gap-graded hot mix asphalt (RHMA-G) base, the debonding occurred around 0.2 to 0.4 in. below the top of the RHMA-G surface. This indicates that the upward movement of the slab from the large thermal and drying shrinking curling effects resulted in tensile stresses in the RHMA-G that were greater than its tensile strength, which was less than the tensile strength of the concrete/RHMA-G bond. In the sections with old hot mix asphalt base, the debonding took place at the concrete-asphalt interface.

- The pass of a 22-kip single axle (10% overloaded) was simulated with the Monte Carlo simulation approach. The simulation indicates that the COA tensile stresses are below 50% of the flexural strength of the concrete at the one-year age, despite the simulation assuming the lowest slab temperature (40°F) expected in the SR 113 thin COA, which resulted in the lowest expected performance of the transverse joints.

The following recommendations are based on the evaluation of the initial performance of the SR 113 thin COA:

- Consider the use of shrinkage reducing admixture (SRA), as a concrete admixture, in COA projects in dry climate regions. The use of this admixture is expected to reduce drying shrinkage to 50%, which will have a positive impact on smoothness seasonal stability and will diminish the risk of concrete cracking and transverse joint faulting.
- Closely monitor saw-cutting operations to ensure the ratio between saw-cut depth and slab thickness does not fall below one-third, particularly when the overlay thickness is at the top of the 4 to 7 in. range typically used in COA.
- Consider delaying the post-construction blanket grinding operation, if this operation needed, until one full summer has passed. Slab curvature variations due to drying shrinkage will diminish after the first drying cycle.
- Monitor seasonal variation of the IRI in other COA pilots in the Caltrans road network.
- Evaluate transverse joint LTE in other COA pilots in the Caltrans road network to determine if the LTE high-low pattern observed in the SR 113 thin COA is also present in these other pilots.

The use of tie bars and the effect of slab thickness could not be evaluated in the Woodland SR 113 thin COA pilot. It is recommended that future Caltrans COA pilots evaluate the effect of these two design variables.

# TABLE OF CONTENTS

---

<b>PROJECT OBJECTIVES .....</b>	<b>iv</b>
<b>EXECUTIVE SUMMARY .....</b>	<b>v</b>
<b>LIST OF FIGURES.....</b>	<b>xi</b>
<b>LIST OF TABLES.....</b>	<b>xiv</b>
<b>LIST OF ABBREVIATIONS .....</b>	<b>xv</b>
<b>1 INTRODUCTION.....</b>	<b>1</b>
<b>2 DESCRIPTION OF THE PROJECT.....</b>	<b>4</b>
2.1 Test Sections .....	4
2.2 Weather and Traffic .....	5
<b>3 CORING CAMPAIGN .....</b>	<b>7</b>
<b>4 VISUAL INSPECTION OF THE CONCRETE OVERLAY .....</b>	<b>14</b>
<b>5 RESPONSE OF THE CONCRETE SLABS UNDER THE HYGROTHERMAL ACTIONS .....</b>	<b>17</b>
5.1 Drying Shrinkage in the Thin COA Slabs.....	19
5.2 Apparent Coefficient of Thermal Expansion of the Thin COA Slabs.....	21
5.3 SR 113 Slabs Restriction to Expand (Expansion Locking) .....	23
5.4 Effect of Experiment Design Variables.....	27
<b>6 SMOOTHNESS OF THE CONCRETE OVERLAY .....</b>	<b>29</b>
6.1 Effect of Slab Curvature on IRI.....	30
6.2 Evolution of Slab Curvature-Corrected IRI.....	33
<b>7 SURFACE MACROTEXTURE OF THE CONCRETE OVERLAY .....</b>	<b>35</b>
<b>8 STRUCTURAL EVALUATION OF THE THIN COA SECTIONS.....</b>	<b>37</b>
8.1 Evaluation of the Thin COA Sections Under Falling Weight Deflectometer Loading.....	37
8.1.1 Falling Weight Deflectometer Sections and Evaluations .....	37
8.1.2 Structural Differences Between Sections and Evaluations .....	39
8.1.3 Backcalculation of the Structural Parameters of the Thin COA Structure .....	41
8.1.4 Load Transfer Efficiency of the Transverse Joints.....	43
8.1.5 LTE-Deflection High-Low Pattern .....	46
8.2 Transverse Joint Deployment .....	47
8.3 Ambient Environment Effects on Load Transfer Efficiency.....	50
8.4 Evaluation of the Thin COA Sections Under Truck Loading.....	52
8.4.1 Real Load Testing Evaluations .....	53
8.4.2 Processing of Strain Data .....	55
8.4.3 Structural Differences Between Sections and Evaluations .....	62
8.4.4 Evaluation of the Structural Contribution of the Asphalt Base.....	65
8.4.5 Modeling Thin COA Structural Response Under Truck Loading.....	67
8.4.6 Monte Carlo Simulation of the Concrete Tensile Stresses Under Truck Loading.....	71
<b>9 CONCLUSIONS AND RECOMMENDATIONS .....</b>	<b>74</b>
9.1 Conclusions .....	74
9.2 Recommendations .....	77
<b>10 REFERENCES .....</b>	<b>79</b>

# LIST OF FIGURES

---

Figure 1.1: Layout of the Woodland thin COA pilot. ....	3
Figure 1.2: Woodland thin COA pilot. ....	3
Figure 2.1: Thin COA project test sections. ....	5
Figure 3.1: Transverse joint deflection pattern example (FWD Section B-NB3, FWD loading 15.7 kips, August 2019 evaluation, around 9 months after Segment B overlay construction).....	7
Figure 3.2: Transverse joint LTE pattern example (FWD Section B-NB3, FWD loading 15.7 kips, August 2019 evaluation, around nine months after Segment B overlay construction).....	8
Figure 3.3: Transverse joint deflection pattern example (FWD Section A-NB3, FWD loading 15.7 kips). ....	9
Figure 3.4: Transverse joint deflection pattern example (FWD Section B-NB3, FWD loading 15.7 kips). ....	9
Figure 3.5: Transverse joint deflection example (FWD Section A-SB1, FWD loading 15.7 kips). ....	10
Figure 3.6: Coring layout.....	10
Figure 3.7: Undeployed transverse joints, showing no debonding. ....	11
Figure 3.8: Deployed transverse joints, also showing slab/base debonding. ....	12
Figure 4.1: Typical appearance of the concrete overlay. ....	15
Figure 4.2: No faulting at transverse joint. ....	15
Figure 4.3: Popout. ....	16
Figure 4.4: Low-severity spalling.....	16
Figure 5.1: Instrumentation layout. ....	17
Figure 5.2: Location of instrumented points (IP).....	18
Figure 5.3: Trial slab instrumentation layout. ....	18
Figure 5.4: Drying shrinkage of the trial slabs. ....	19
Figure 5.5: Mean drying shrinkage of SR 113 slabs. ....	20
Figure 5.6: Differential drying shrinkage of SR 113 slabs. ....	21
Figure 5.7: Apparent CTE of the trial slabs.....	22
Figure 5.8: Example of slab expansion/contraction during warm season (SR 113, IP A21).....	23
Figure 5.10: Example of slab expansion/contraction during warm season (SR 113, IP A31).....	24
Figure 5.11: Example of slab expansion/contraction during cold season (SR 113, IP A21). ....	24
Figure 5.12: Example of slab expansion/contraction during cold season (SR 113, IP A22). ....	25
Figure 5.13: Example of slab expansion/contraction during cold season (SR 113, IP A31). ....	25
Figure 5.14: Slab restriction effect on apparent CTE (SR 113, average all instrumented points [IP])....	26
Figure 5.15: Strain measured in SR 113 slabs (average all IP). ....	27
Figure 6.1: Evolution of IRI.....	30
Figure 6.2: Example of impact of slab temperature gradient on IRI (Section A3, North). ....	31
Figure 6.3: Example of diurnal evolution of IRI and ELTD; Section A3, North, evaluation Post-Grinding (14 months). ....	32
Figure 6.4: Example of diurnal evolution of IRI and slab curvature; Section A3, North, evaluation Post-Grinding (14 months).....	32
Figure 6.5: Example of impact of slab curvature on IRI (Section A3, North). ....	33

Figure 6.6: Evolution of slab curvature-corrected corrected IRI. ....	34
Figure 7.1: Evolution of the mean profile depth (MPD). ....	35
Figure 7.2: Grinded concrete surface. ....	36
Figure 8.1: Example of FWD section layouts. ....	38
Figure 8.2: Deflection at slab center (FWD loading = 15.7 kips). ....	39
Figure 8.3: Deflection at transverse joint (FWD loading = 15.7 kips). ....	40
Figure 8.4: Transverse joint LTE (FWD loading = 15.7 kips). ....	40
Figure 8.5: Backcalculated thickness of the slab-base bilayer structure. ....	42
Figure 8.6: Backcalculated modulus of subgrade reaction of the subbase-subgrade system. ....	43
Figure 8.7: Seasonal evolution of transverse joint LTE. ....	44
Figure 8.8: LTE histogram. ....	44
Figure 8.9: LTE measured in 4.58B thin COA sections with 6x6 slabs (pre-HVS testing evaluation). ....	45
Figure 8.10: Comparison between LTE of SR 113 and 4.58B thin COA sections with 6x6 slabs. ....	46
Figure 8.11: LTE high-low pattern (all FWD sections, three evaluation). ....	47
Figure 8.12: LTE histogram of joints with good and poor LTE performance. ....	47
Figure 8.13: FWD assessment of joint deployment (left, FWD Section B-NB3; right, Section A-SB1). ..	48
Figure 8.14: LTE histogram of joints with poor LTE performance. ....	49
Figure 8.15: Early joint deployment and LTE comparison. ....	50
Figure 8.16: Example of LTE variation versus slab temperature (FWD Section B-N3, Winter 2019-20 evaluation). ....	51
Figure 8.17: Example of LTE variation versus slab temperature (FWD Section B-N3). ....	52
Figure 8.18: Instrumentation layout. ....	53
Figure 8.19: Location of instrumented points (IP). ....	54
Figure 8.20: Experiment truck passing over instrumented slab (IP A21). ....	55
Figure 8.21: Example of data collected with resistive strain gauges (Section A2, IP A21, Pass 01, Summer 2019). ....	56
Figure 8.22: Example of data collected with resistive strain gauges (Section A2, IP A22, Pass 01, Summer 2019). ....	56
Figure 8.23: Example of data collected with resistive strain gauges (Section A3, IP A31, Pass 01, Summer 2019). ....	57
Figure 8.24: Example of data collected with resistive strain gauges (Section A3, IP A32, Pass 33, Summer 2019). ....	57
Figure 8.25: Peak strain registered under the drive axle of the truck (Section A2, IP A21, Summer 2019). ....	58
Figure 8.26: Peak strain registered under the drive axle of the truck (Section A2, IP A22, Summer 2019). ....	59
Figure 8.27: Peak strain registered under the drive axle of the truck (Section A3, IP A31, Summer 2019). ....	60
Figure 8.28: Peak strain registered under the drive axle of the truck (Section A3, IP A32, Summer 2019). ....	61
Figure 8.29: Layout of the different types of joints. ....	63
Figure 8.30: Midday (ELTD = 0) peak strain registered under truck second axle. ....	64
Figure 8.31: ANOVA table of midday (ELTD = 0) peak strain registered under truck second axle at the bottom of the concrete slabs ....	65

Figure 8.32: Comparison between peak strains registered under truck second axle at slab bottom and asphalt base (Section A2, IP A21, Summer 2020).....	66
Figure 8.33: Comparison between model and measured peak strain for joints with good LTE (Summer 2019). .....	69
Figure 8.34: Comparison between model and measured peak strain for joints with poor LTE (Summer 2019). .....	69
Figure 8.35: Comparison between model and measured peak strain for undeployed joints (Summer 2019). .....	70
Figure 8.36: Comparison between FWD LTE and effective LTE under truck loading for joints with poor LTE. ....	71
Figure 8.37: Monte Carlo simulation of 22-kip single axle running on SR 113 thin COA during minimum TPCC conditions (TPCC = 40°F, 1-year age) .....	73

## LIST OF TABLES

---

Table 6.1: Smoothness Evaluations of SR 113 Thin COA Project.....	29
Table 8.1: Location of FWD Sections.....	38
Table 8.2: FWD Evaluations Dates .....	38
Table 8.3: Real Load Testing Evaluation Dates.....	54



## LIST OF ABBREVIATIONS

---

AADTT	Average annual daily truck traffic
ANOVA	Analysis of variance
APP	Approach
COA	Concrete overlay on asphalt
CTE	Coefficient of thermal expansion
ELTD	Equivalent linear temperature difference
FEM	Finite element method
FWD	Falling weight deflectometer
HMA	Hot mix asphalt
IP	Instrumented point
IRI	International Roughness Index
LTE	Load transfer efficiency
LTPP	Long-Term Pavement Performance
LVE	Leave
MPD	Mean Profile Depth
MRI	Mean Roughness Index
PM	Post mile
PPRC	Partnered Pavement Research Center
RH	Relative humidity
RHMA-G	Rubberized gap-graded hot mix asphalt
RLT	Real load testing
SR	State Route
SRA	Shrinkage reducing admixture
TPCC	Temperature of portland cement concrete
UCPRC	University of California Pavement Research Center
USP	Unrestrained shrinkage prism
VWSG	Vibrating wire strain gauge

## SI\* (MODERN METRIC) CONVERSION FACTORS

APPROXIMATE CONVERSIONS TO SI UNITS				
Symbol	When You Know	Multiply By	To Find	Symbol
<b>LENGTH</b>				
in.	inches	25.40	millimeters	mm
ft.	feet	0.3048	meters	m
yd.	yards	0.9144	meters	m
mi.	miles	1.609	kilometers	km
<b>AREA</b>				
in <sup>2</sup>	square inches	645.2	square millimeters	mm <sup>2</sup>
ft <sup>2</sup>	square feet	0.09290	square meters	m <sup>2</sup>
yd <sup>2</sup>	square yards	0.8361	square meters	m <sup>2</sup>
ac.	acres	0.4047	hectares	ha
mi <sup>2</sup>	square miles	2.590	square kilometers	km <sup>2</sup>
<b>VOLUME</b>				
fl. oz.	fluid ounces	29.57	milliliters	mL
gal.	gallons	3.785	liters	L
ft <sup>3</sup>	cubic feet	0.02832	cubic meters	m <sup>3</sup>
yd <sup>3</sup>	cubic yards	0.7646	cubic meters	m <sup>3</sup>
<b>MASS</b>				
oz.	ounces	28.35	grams	g
lb.	pounds	0.4536	kilograms	kg
T	short tons (2000 pounds)	0.9072	metric tons	t
<b>TEMPERATURE (exact degrees)</b>				
°F	Fahrenheit	(F-32)/1.8	Celsius	°C
<b>FORCE and PRESSURE or STRESS</b>				
lbf	pound-force	4.448	newtons	N
lbf/in <sup>2</sup>	pound-force per square inch	6.895	kilopascals	kPa
APPROXIMATE CONVERSIONS FROM SI UNITS				
Symbol	When You Know	Multiply By	To Find	Symbol
<b>LENGTH</b>				
mm	millimeters	0.03937	inches	in.
m	meters	3.281	feet	ft.
m	meters	1.094	yards	yd.
km	kilometers	0.6214	miles	mi.
<b>AREA</b>				
mm <sup>2</sup>	square millimeters	0.001550	square inches	in <sup>2</sup>
m <sup>2</sup>	square meters	10.76	square feet	ft <sup>2</sup>
m <sup>2</sup>	square meters	1.196	square yards	yd <sup>2</sup>
ha	hectares	2.471	acres	ac.
km <sup>2</sup>	square kilometers	0.3861	square miles	mi <sup>2</sup>
<b>VOLUME</b>				
mL	milliliters	0.03381	fluid ounces	fl. oz.
L	liters	0.2642	gallons	gal.
m <sup>3</sup>	cubic meters	35.31	cubic feet	ft <sup>3</sup>
m <sup>3</sup>	cubic meters	1.308	cubic yards	yd <sup>3</sup>
<b>MASS</b>				
g	grams	0.03527	ounces	oz.
kg	kilograms	2.205	pounds	lb.
t	metric tons	1.102	short tons (2000 pounds)	T
<b>TEMPERATURE (exact degrees)</b>				
°C	Celsius	1.8C + 32	Fahrenheit	°F
<b>FORCE and PRESSURE or STRESS</b>				
N	newtons	0.2248	pound-force	lbf
kPa	kilopascals	0.1450	pound-force per square inch	lbf/in <sup>2</sup>

\*SI is the abbreviation for the International System of Units. Appropriate rounding should be made to comply with Section 4 of ASTM E380. (Revised April 2021)

# 1 INTRODUCTION

---

Thin concrete overlay on asphalt (COA), formerly known as thin whitetopping, is a pavement rehabilitation technique that consists of placement of a 4 to 7 in. thick concrete overlay on an existing flexible or composite pavement. This technique, an alternative to conventional concrete overlay construction, has been used frequently on highways and conventional roads in several US states as well as in other countries, but its use in California has been very limited.

Under Partnered Pavement Research Center Strategic Plan Element (SPE) Project 4.58B, the thin COA technique was evaluated using accelerated loading applied by a Heavy Vehicle Simulator (HVS) from 2014 to 2017. That research project's main conclusion was that a "well-designed and well-built 6x6 thin bonded concrete overlay placed on top of an asphalt base that is in fair to good condition can potentially provide 20 years of good serviceability on most of California's non-interstate roadways" (1,2). Based on that evaluation, Caltrans decided to implement the technique in the field, and several Caltrans districts proceeded with thin COA pilot projects. District 3 implemented the technique in the rehabilitation of State Route 113 (SR 113), and District 8 implemented it for State Route 247 (SR 247). The initial performance of the District 3 thin COA project, located in Woodland, California, is documented in this report.

The Woodland thin COA pilot site extended over approximately four miles of SR 113, between PM 11.860 and PM 12.890 and between PM 14.760 and PM 17.580 (Figure 1.1). SR 113 is a two-lane road (Figure 1.2) in these areas. The north part of the project, referred to in this report as Segment B (PM 14.760 to PM 17.580), was built in October and November 2018, while the south part, referred to as Segment A (PM 11.860 to PM 12.890), was built in April and May 2019.

This report documents the initial performance of the Woodland SR 113 thin COA pilot project, including the following topics:

- Chapter 2 briefly describes the project, including test sections, construction, traffic, and weather conditions. These topics are covered in detail in a previous report UCPRC report, *Concrete Overlay on Asphalt Pilot Project at Woodland SR 113: Construction (3)*.

- Chapter 3 presents the outcomes of a limited coring campaign conducted in August 2020. The main goal of the coring campaign was to assess the level of deployment of the COA transverse joints. It served also to determine the condition of the slab-asphalt base bonding.
- Chapter 4 presents the outcomes of the visual inspection of the COA conducted in December 2020. No cracking or any other sign of structural damage was observed during this evaluation.
- Chapter 5 presents the outcomes of the analysis of the structural response of the slabs measured under the hydrothermal actions (thermal and drying shrinkage actions). Data collected with thermocouples, vibrating wire strain gauges (VWSGs), and relative humidity (RH) sensors are the basis of the analysis presented in Chapter 5.
- Chapter 6 presents the evaluation of the concrete overlay smoothness. The smoothness was measured with a laser profiler after the construction of the concrete overlay, after the grinding operation, and then periodically during the initial evaluation period covered in this report (up to the second half of 2020).
- Chapter 7 presents the evaluation of the concrete overlay surface macrotexture. The surface macrotexture was measured with a laser texturometer after the construction of the concrete overlay, after the grinding operation, and then periodically during the initial evaluation period covered in this report (up to the second half of 2020).
- Chapter 8 presents the evaluation of the structural capacity of the COA. Deflection measured under falling weight deflectometer (FWD) loading and strain measured with resistive strain gauges under truck loading (real load testing) were analyzed. FWD and real load testing (RLT) were conducted three times: August 2019, January 2020, and August 2020.
- Chapter 9 presents conclusions and recommendations based on the study findings.

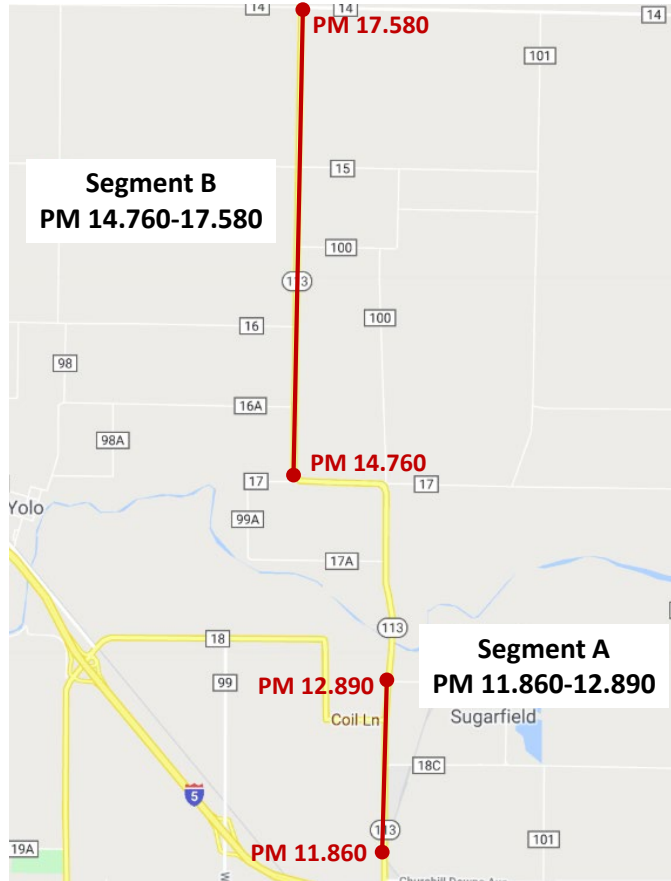


**Figure 1.1: Layout of the Woodland thin COA pilot.**



**Figure 1.2: Woodland thin COA pilot.**

## 2 DESCRIPTION OF THE PROJECT

---

### 2.1 Test Sections

The Woodland SR 113 project design builds on the successful evaluation of a thin COA project with half-lane width slabs (6×6 ft.) built for an earlier Caltrans research project (1,2). The main design features of the Woodland SR 113 concrete overlay are the following:

- Transverse joint spacing: 6 ft.
- Slab width: 6 ft. for interior slabs and 8 ft. for exterior slabs (2 ft. widened slabs)
- Slab thickness: 0.5 ft. (6 in.)
- Undoweled (except for transverse construction joints)
- Tie bars at all longitudinal joints
- Unsealed joints with cuts 1/8 in. wide and 2 in. deep

The project included the following three structural sections (Figure 2.1) that differ from one another in the asphalt base:

- Sections A1 and A3, with 0.17 to 0.42 ft. ( 2 to 5 in.) thick old HMA base
- Section A2, with 0.13 ft. (1.5 in.) thick rubberized gap-graded hot mix asphalt (RHMA-G) overlay on top of the milled old HMA (total asphalt thickness of Section A2 is similar to Sections A1 and A3)
- Section B, with 0.08 to 0.25 ft. (1 to 3 in.) thick old HMA base

Asphalt base thickness values in this list and shown in Figure 2.1 were determined from cores that were extracted from between the wheelpaths. At the shoulder edge of the pavement, the asphalt base was either thinner or nonexistent. Further, the condition of the asphalt base that remained after milling was very poor. Cracking and areas of delamination were present throughout the project area. Due to the poor condition of the asphalt base, the Woodland SR 113 overlay is not expected to work as a composite concrete-asphalt structure but instead as short concrete slabs resting on the base. Details of the condition of the asphalt base are included in the previous UCPRC thin COA study report (3).

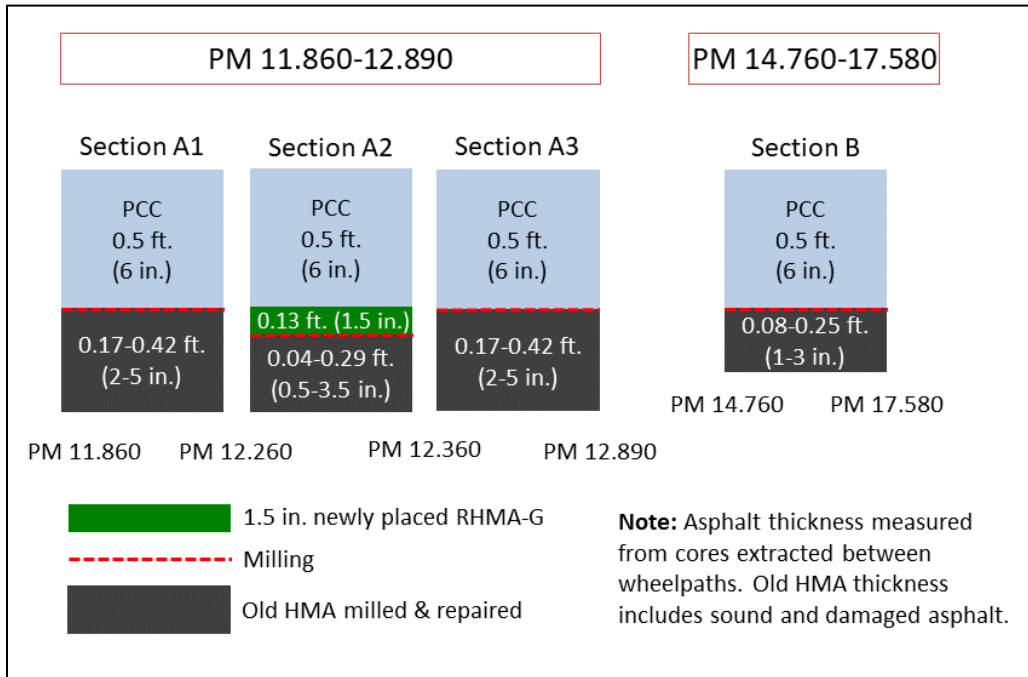


**Figure 2.1: Thin COA project test sections.**

The concrete mixture was designed to provide flexural strength of 450 psi (the project special provisions requirement for opening to traffic) in 24 hours. The mixture included Type II/V portland cement (574 lb./cy) and Class N fly ash (15% total cementitious materials). The ratio of water to total cementitious materials was 0.43. The mixture design slump was 2±0.5 in., which is a low value compatible with slipform paving. Details of the mixture design and laboratory testing results (modulus of elasticity, compressive strength, flexural strength, coefficient of thermal expansion [CTE], and drying shrinkage) are included in the previous UCPRC thin COA study report (3).

## 2.2 Weather and Traffic

The city of Woodland, California, is in Yolo County, in the Inland Valley climate region (4). This region has a climate that is similar to a Mediterranean climate, with hot, dry summers and relatively mild, wet winters. The city’s average annual mean temperature is 61°F, with mean monthly values that range from 47°F in December to 77°F in July. Woodland’s average annual mean rainfall is 10 in., and its wet

season generally runs from November through April while its driest period generally lasts from June to September.

The traffic volume of the project's south and north parts differ: the south part (PM 11.860 to PM 12.890, Segment A) supports more traffic than the north one (PM 14.760 to PM 17.580, Segment B). The average annual daily truck traffic (AADTT) of Segment A is about 570 (two-way), and Segment B's AADTT is about 240.



### 3 CORING CAMPAIGN

The structural capacity of the thin COA was periodically evaluated with the falling weight deflectometer (FWD). A total of 20 “FWD sections” were selected for periodic evaluation, with each FWD section comprising five consecutive slabs. Half of the FWD sections were in Segment A and the other half in Segment B (the location of the 20 FWD sections is shown in Table 8.1; each FWD section is assigned a unique code—e.g., “FWD Section B-NB3” corresponds to the third FWD section in Segment B northbound direction). The FWD evaluation showed an alternating high-low deflection pattern, shown in Figure 3.1. The deflection pattern was due to alternating transverse joints with good and poor load transfer efficiency (LTE). Figure 3.1 and Figure 3.2 are examples from the first evaluation (August 2019, around nine months after Segment B overlay construction) of FWD Section B-NB3, located in Segment B in the northbound direction. A similar pattern was observed in most of the 20 FWD sections. This pattern raised the question of whether all the transverse joints had deployed. To answer that question, a coring campaign was conducted in August 2020. The design and results of the coring campaign are presented in the following discussion.

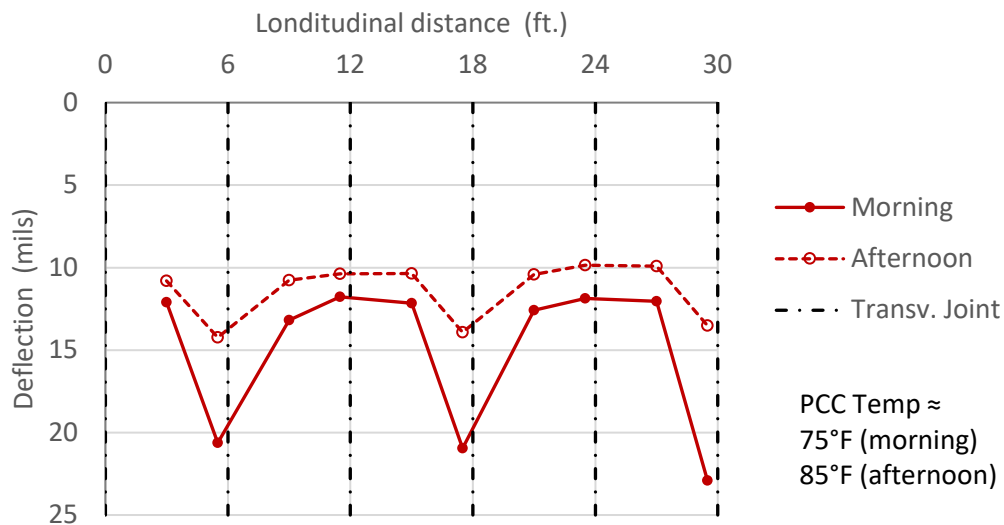


**Figure 3.1: Transverse joint deflection pattern example (FWD Section B-NB3, FWD loading 15.7 kips, August 2019 evaluation, around nine months after Segment B overlay construction).**

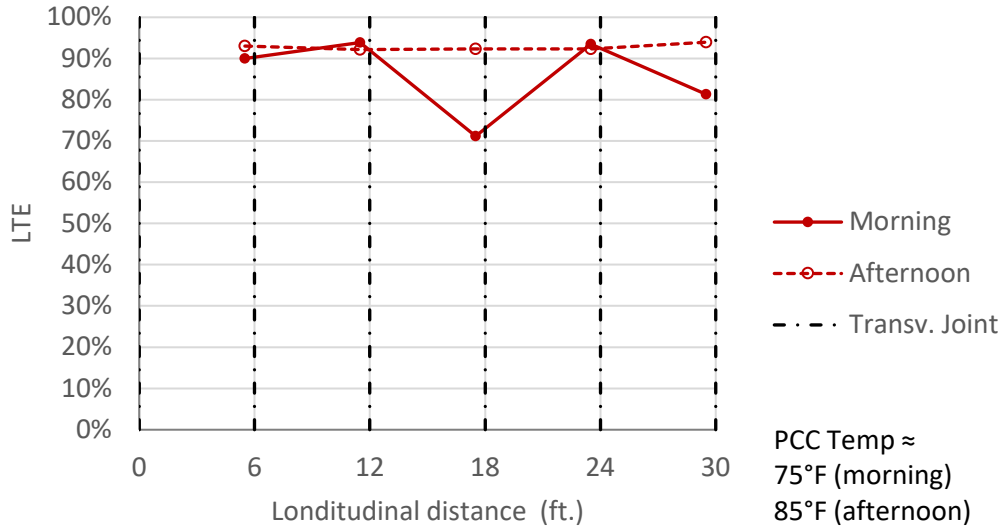


**Figure 3.2: Transverse joint LTE pattern example (FWD Section B-NB3, FWD loading 15.7 kips, August 2019 evaluation, around nine months after Segment B overlay construction).**

Three FWD sections were selected for coring. Two of the sections, A-NB3 and B-NB3, showed a very clear deflection and LTE high-low pattern. In these two sections, the deflection measured at the joints with good LTE was similar to the deflection measured at the center of the slabs (between the transverse joints), shown in Figure 3.3 and Figure 3.4. The deflections measured in the third FWD section, A-SB1, also showed a high-low pattern, shown in Figure 3.5, but were not as distinct as in the other two FWD sections.

A pair of consecutive transverse joints was selected for coring in each of the three FWD sections. The pair of consecutive transverse joints selected for the three FWD sections are shown in Figure 3.3 to Figure 3.5 with either dashed or dotted lines. The dashed line corresponds to the transverse joint with poor LTE and the dotted line corresponds to the transfer joint with good LTE. The FWD deflections measured at the joint with poor LTE (dashed line) were relatively high and were highly impacted by testing time and season. The deflections at the other joint with good LTE (dotted line) were relatively low and presented little variation in terms of testing time and season.

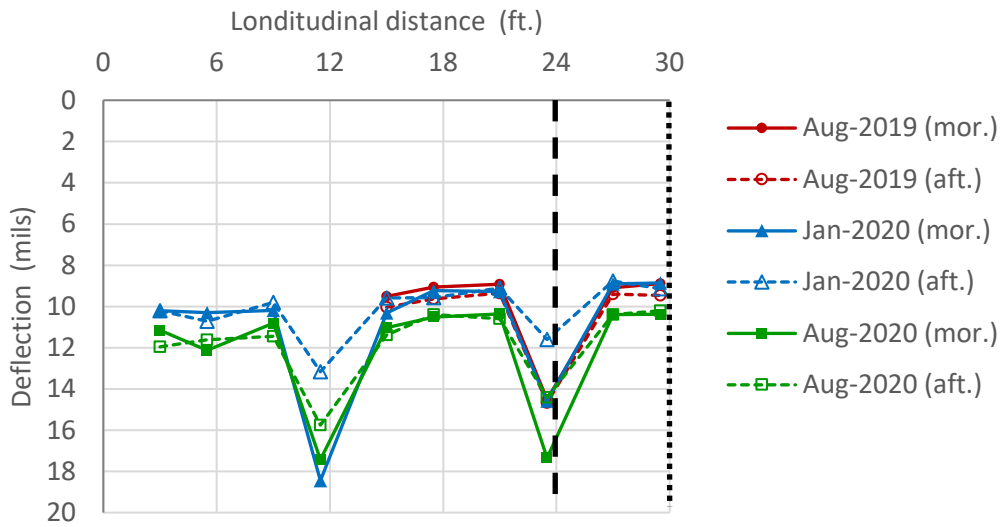


Figure 3.3: Transverse joint deflection pattern example (FWD Section A-NB3, FWD loading 15.7 kips).

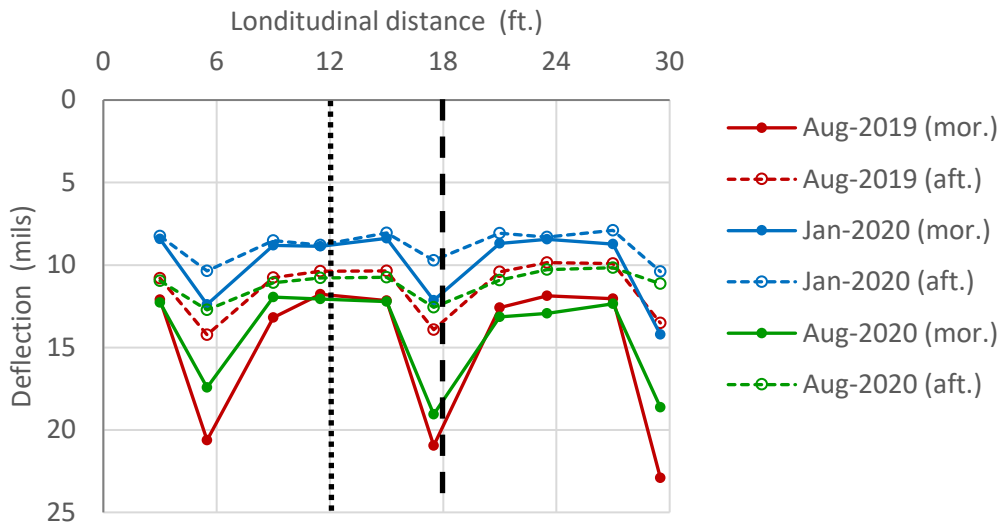
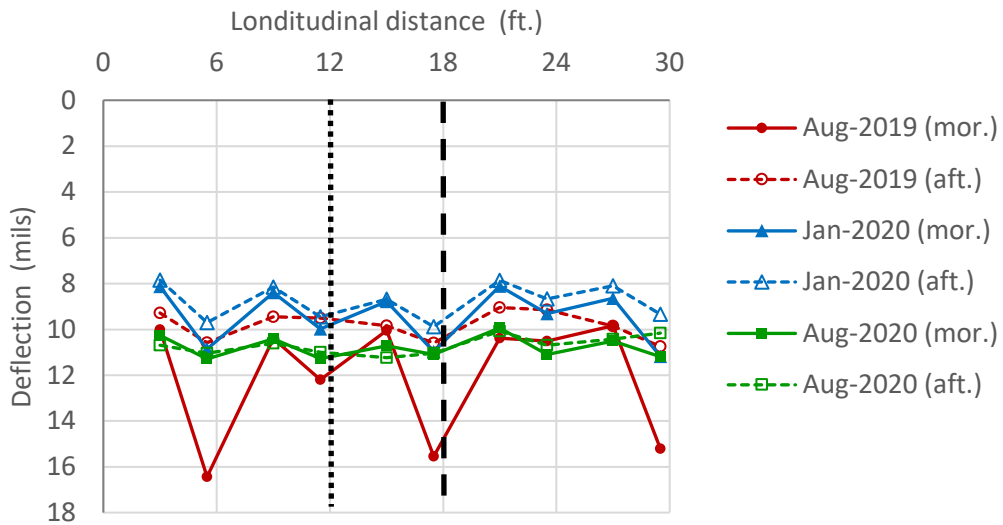
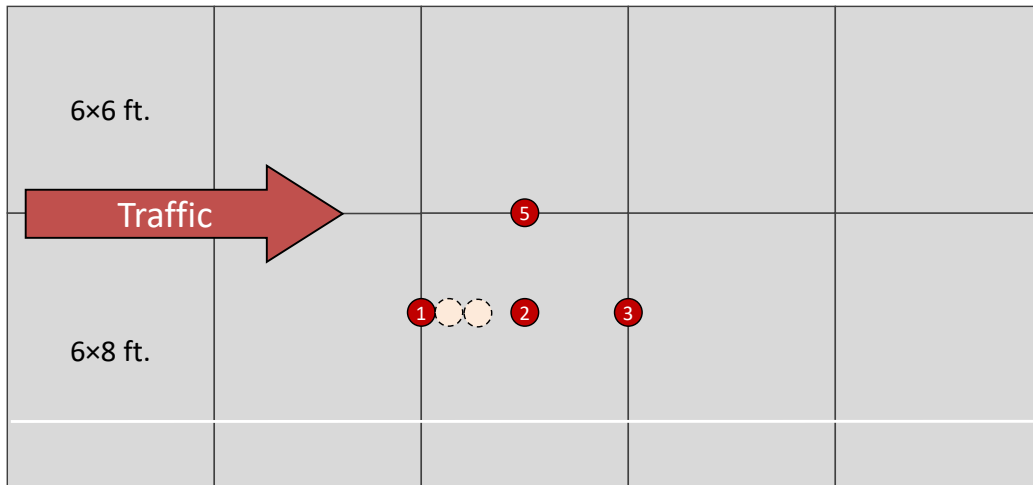


Figure 3.4: Transverse joint deflection pattern example (FWD Section B-NB3, FWD loading 15.7 kips).



**Figure 3.5: Transverse joint deflection example (FWD Section A-SB1, FWD loading 15.7 kips).**

A core was extracted at each of the two transverse joints selected in each of the sections. If the coring revealed that the concrete and asphalt were debonded, a series of adjacent cores was extracted to assess the extent of the debonding (see cores adjacent to Core 1 in Figure 3.6). Cores were also extracted at the slab center (Core 2) and longitudinal joint (Core 5), shown in Figure 3.6.



**Figure 3.6: Coring layout.**

The visual inspection of the cores resulted in the following observations:

1. The longitudinal joint deployed in the three sections that were evaluated.

2. The transverse joints with good LTE in Section A-NB3 and Section B-NB3 had not deployed, shown in Figure 3.7.
3. The transverse joints with poor LTE in Section A-NB3 and Section B-NB3 had deployed, shown in Figure 3.8. The concrete slab and asphalt base were debonded at these joints. In Section A-NB3, with the RHMA-G base, the debonding took place about 0.2 to 0.4 in. below the top of the RHMA-G surface, shown in Figure 3.8 (left). In Section B-NB3, with the old HMA base, the debonding took place at the concrete-asphalt interface, shown in Figure 3.8 (right). The coring revealed that the debonding extended about 10 to 20 in. away from the transverse joints regardless of the type of asphalt base.
4. The two transverse joints of Section A-SB1 had deployed. The concrete and asphalt base were debonded at both transverse joints, though the extension of the debonding was much larger (about 15 in.) at the joint with poor LTE than at the joint with good LTE. In both cases, the debonding occurred at the concrete-asphalt interface. The asphalt base in this section was old HMA.



FWD Section A-NB3

FWD Section B-NB3

**Figure 3.7: Undeployed transverse joints, showing no debonding.**

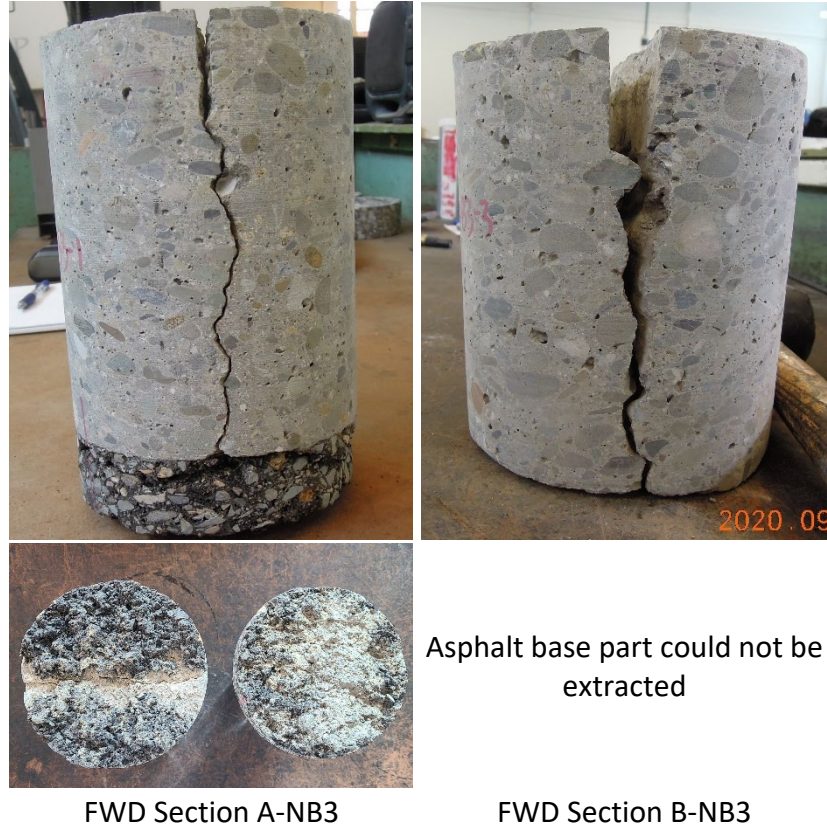


**Figure 3.8: Deployed transverse joints, also showing slab/base debonding.**

The coring showed debonding at the transverse joints that deployed in FWD Section A-NB3 and Section B-NB3, with a 12 ft. effective slab length. This finding agrees with the debonding observed in the thin COA sections with 12×12 ft. slabs that were evaluated in a previous Caltrans research project (1). In the thin COA sections for that study, with RHMA-G base, the debonding took place about 0.2 to 0.4 in. below the top of the RHMA-G surface, just as in the SR 113 Section A-NB3. This indicates that the upward movement of the slab from the large thermal and drying shrinking curling effects resulted in tensile stresses in the RHMA-G that were greater than its tensile strength, which was less than the tensile strength of the concrete/RHMA-G bond.

The coring showed that California is not free of an issue that has been reported in other states such as Minnesota (5), where not all the transverse joints of the thin COA with short slabs (about 6 ft. long) deploy. In the SR 113 thin COA project, the lack of transverse joint deployment resulted in effective slabs that were 12 ft. long rather than the intended 6 ft. The coring showed also that even if the

transverse joints deploy, as occurred with FWD Section A-SB1, the LTE may still present a clear high-low pattern (alternating transverse joint good and poor LTE), shown in Figure 3.5.

Another observation from the coring campaign is that the transverse joint cutting was relatively shallow, from 1.5 to 1.8 in. rather than the 2.0 in. target. On the other hand, the overlay thickness was greater than the 6 in. target. The outcome is that the ratio saw-cut depth to slab thickness was between 0.22 and 0.25 (i.e., smaller than the one-third target). These small ratios have contributed to the lack of transverse joint deployment.

## 4 VISUAL INSPECTION OF THE CONCRETE OVERLAY

---

A detailed visual inspection was conducted in December 2020. Overall, the condition of the project was excellent, shown in Figure 4.1. The summary of the visual inspection is as follows:

- No cracking was observed.
- No panel migration was observed.
- No slab rocking was observed.
- Faulting was not noticeable, shown in Figure 4.2.
- No fines pumping was observed at the transverse joints.
- No material-related distresses were observed.
- Some popouts were detected at the north end of Segment B (Figure 4.3). These popouts were detected a few weeks after the overlay construction, and they remain unchanged. They were most likely related to dirt and debris in the concrete mixture. The concrete may have been contaminated during the paving operation as the paving crew shoveled spilled-over concrete from outside the shoulder back into the paving section. This practice is not recommended, and it was noticed occasionally during the construction of the SR 113 thin concrete overlay.
- Low-severity spalling was noticed at some transverse joints (Figure 4.4), particularly at Segment A in the northbound lane. None of the joints would have been rated as “affected by spalling” based on the Federal Highway Administration Long-Term Pavement Performance (LTPP) program’s distress identification manual (6) since the length affected by spalling was minor, much less than 10%.





**Figure 4.1: Typical appearance of the concrete overlay.**



**Figure 4.2: No faulting at transverse joint.**



**Figure 4.3: Popout.**



**Figure 4.4: Low-severity spalling.**

## 5 RESPONSE OF THE CONCRETE SLABS UNDER THE HYGROTHERMAL ACTIONS

The Woodland SR 113 thin COA sections were instrumented with sensors to measure the response of the slabs under hydrothermal actions (thermal and drying shrinkage actions). Thermocouples, relative humidity (RH) sensors, and vibrating wire strain gauges (VWSGs) were installed at several depths, shown in Figure 5.1. The instrumentation shown in Figure 5.1 was installed at three locations, two in Section A2 and one in Section A3, shown in Figure 5.2. Details of the instrumentation installation can be found in a prior thin COA study report (3).

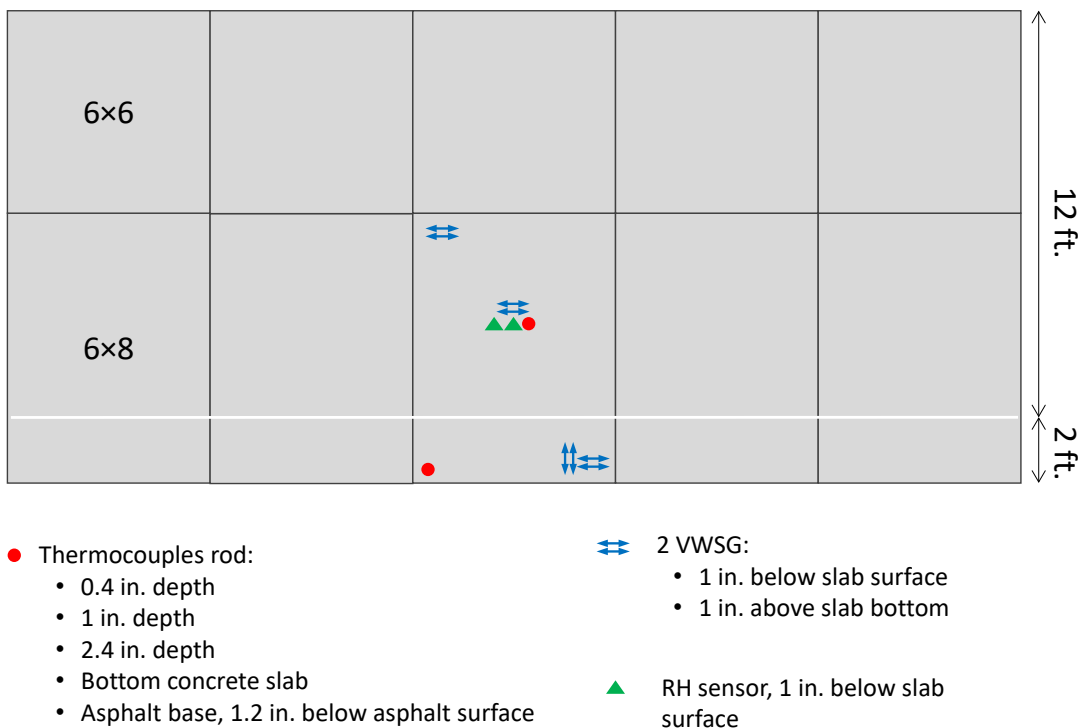


**Figure 5.1: Instrumentation layout.**

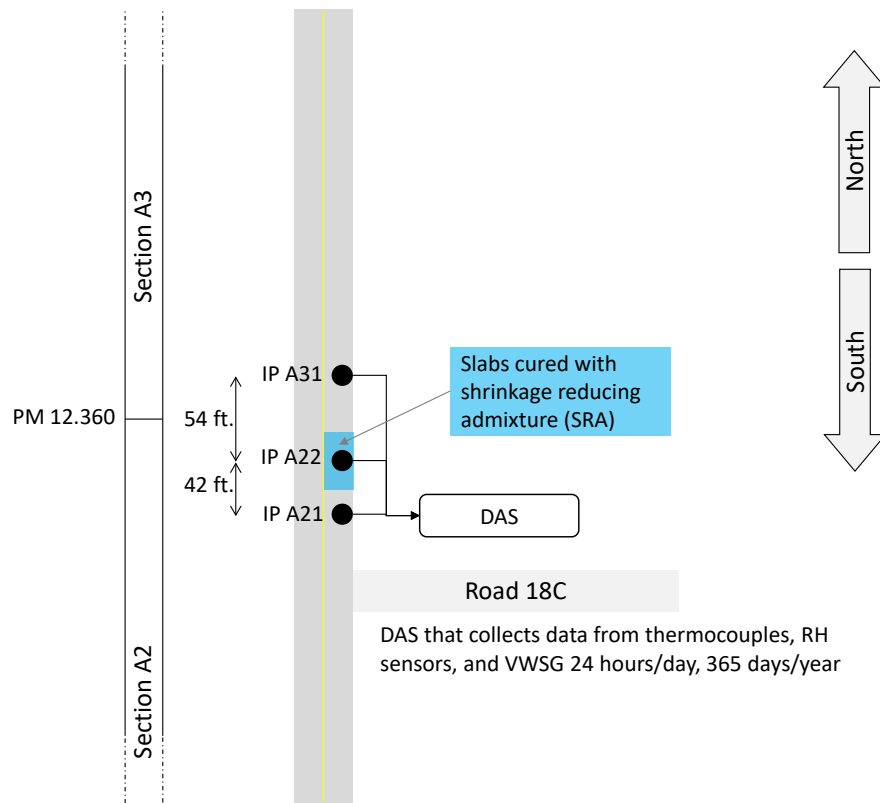


**Figure 5.2: Location of instrumented points (IP).**

On September 18, 2018, prior to the construction of Woodland SR 113 thin COA pilot, a set of trial slabs was built to test the procedure for installing different sensors in the concrete. The trial slabs were built at the UCPRC Davis laboratory site with the same concrete mixture that was used for the construction of the SR 113 overlay and were instrumented with VWSGs and thermocouples, shown in Figure 5.3.

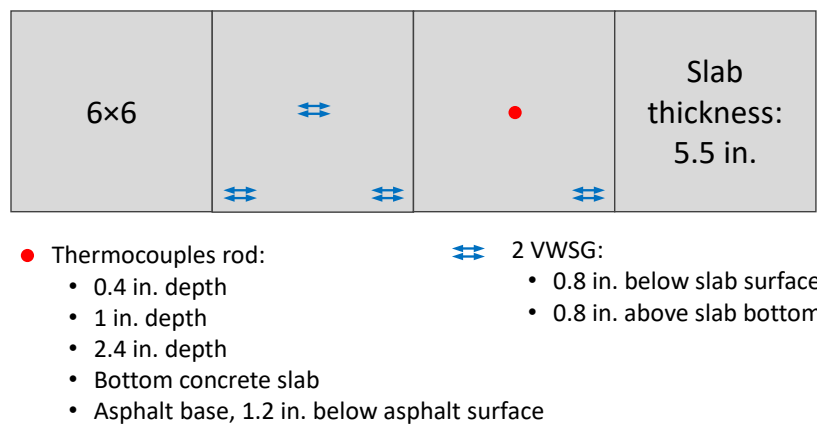


**Figure 5.3: Trial slab instrumentation layout.**

The strain and temperature records were used to estimate the drying shrinkage and the apparent CTE of the concrete of the slabs following the procedure described in a prior thin COA study (7).

### 5.1 Drying Shrinkage in the Thin COA Slabs

The drying shrinkage estimation from measurements on the trial slabs is shown in Figure 5.4. The series “Mean” represents the slab expansion/contraction (average of the top and bottom of the slab strains), while the series “Differential” represents the slab warping (i.e., top minus bottom of the slab strains). The negative sign of the mean shrinkage indicates slab contraction while the negative sign of the differential shrinkage indicates that the slab curvature is concave upwards (the drying shrinkage is greater at the top). The drying shrinkage estimated for a set of unrestrained shrinkage prisms (USPs) that were built during the construction of the trial slabs is shown as the series “USP.” These prisms were fabricated with the same concrete mixture used to build the trial slabs. The prisms were cured the same way as the trial slabs and then left outdoors near the trial slabs. They were used to measure the unrestrained deformations of the concrete since they were not bonded to any support.

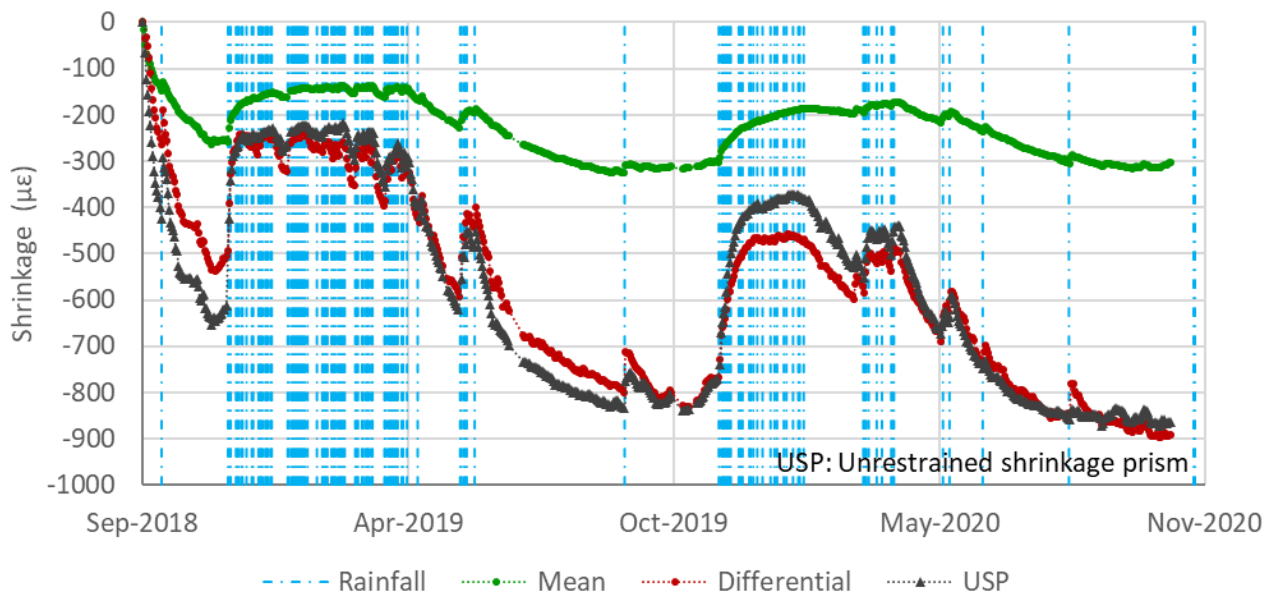
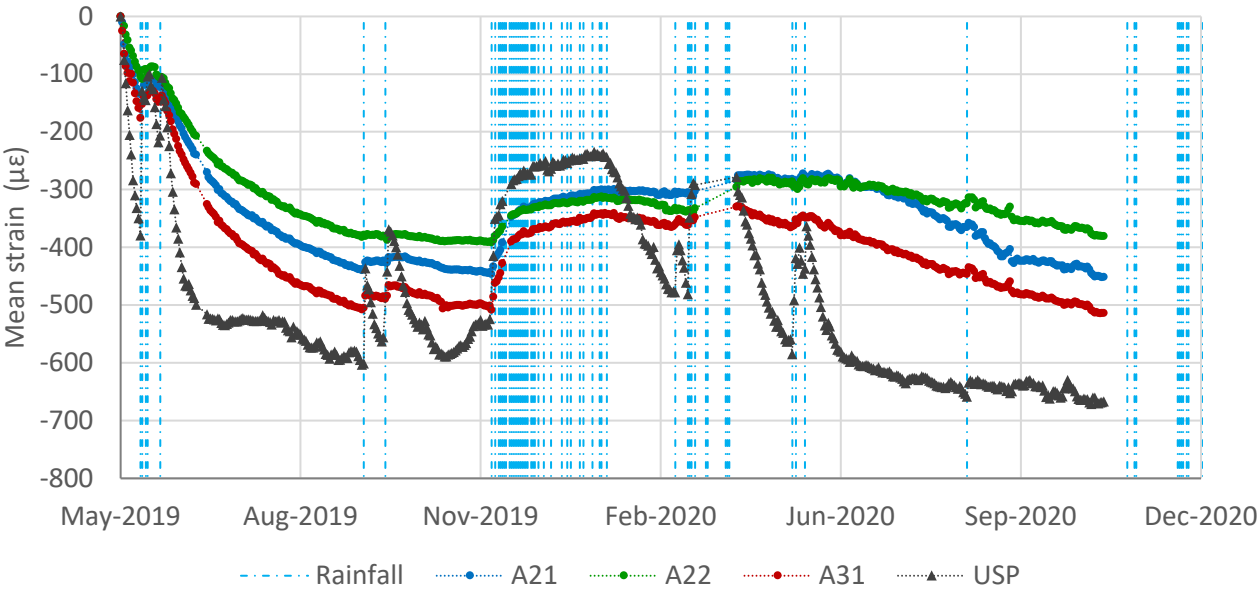
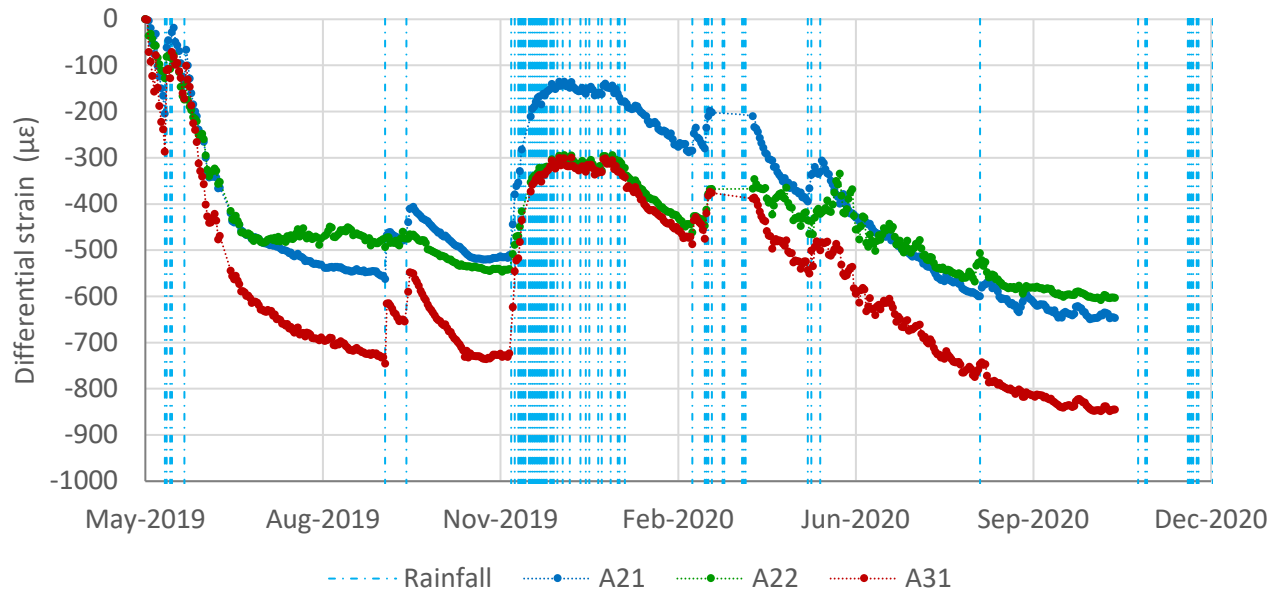


Figure 5.4: Drying shrinkage of the trial slabs.

The drying shrinkage estimation from measurements on the Woodland SR 113 thin COA slabs is shown in Figure 5.5 (mean drying shrinkage) and Figure 5.6 (differential drying shrinkage). The series “USP” in Figure 5.5 is the drying shrinkage estimated for the set of unrestrained shrinkage prisms that were fabricated during the construction of the SR 113 overlay. The prisms were fabricated with the same concrete mixture and cured with the same curing compound used in the concrete overlay, and they were left outdoors on the side of the road near the slabs on SR 113.



**Figure 5.5: Mean drying shrinkage of SR 113 slabs.**



**Figure 5.6: Differential drying shrinkage of SR 113 slabs.**

The trials slabs and SR 113 sections were subjected to very similar weather conditions since they were located close to each other, about 12 miles distance. In both locations, the slabs experienced very high levels of drying shrinkage, particularly during the summer. The differential drying shrinkage (top versus bottom of the slab) reached up to 800  $\mu\epsilon$  in the Woodland thin COA slabs and up to 900  $\mu\epsilon$  in the UCPRC Davis trial slabs. The total drying shrinkage strain reached values up to 750  $\mu\epsilon$  (contraction) at the surface of the slabs. Such high strain is comparable to the shrinkage estimated for the USPs located by the slabs and close to the 1000  $\mu\epsilon$  drying shrinkage measured for the same concrete mixture in the laboratory at 50% air RH following ASTM C157 (3). These results agree with the high drying shrinkage estimated in the previous Caltrans research project for similar slab sizes built with rapid-strength concrete mixtures (7).

## 5.2 Apparent Coefficient of Thermal Expansion of the Thin COA Slabs

The apparent CTE of the slabs was determined based on slab expansion-contraction and slab curling. In the first case, the apparent CTE is the ratio between changes in slab mean strain and changes in slab mean temperature. In the second case, the apparent CTE is the ratio between changes in slab curvature (top minus bottom of the slab strain measured with VWSGs) and changes in the slab equivalent linear

temperature difference (determined from thermocouple readings). In the two cases, the CTE is assumed to be constant within a day. Previous UCPRC research details the calculation procedure (7-9). The apparent CTE obtained for the trial slabs is shown in Figure 5.7. The series “USP” represents the apparent CTE determined for the unrestrained shrinkage prisms located outdoors by the trial slabs, and the series “Lab CTE” represents the CTE determined in the laboratory following AASHTO T336 (saturated concrete).

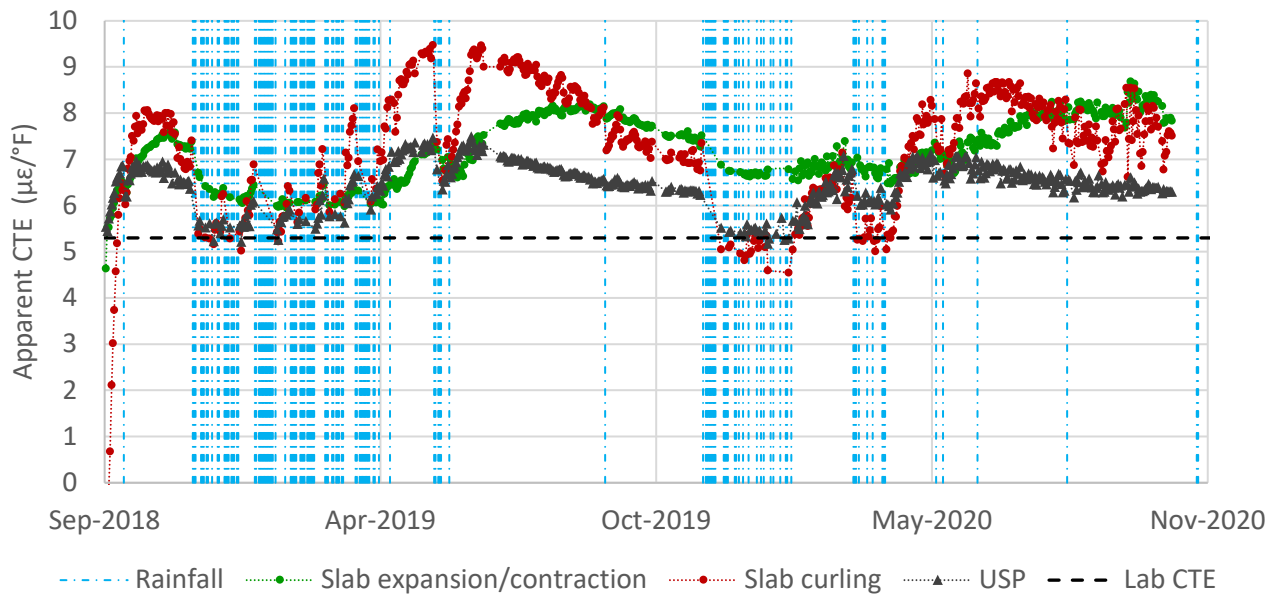


**Figure 5.7: Apparent CTE of the trial slabs.**

As shown in Figure 5.7, the apparent CTE of the slabs can differ considerably from the value determined in the laboratory under saturated conditions, following AASHTO T336. During dry periods (periods between rainfall events), the concrete CTE increases until reaching a maximum. Further drying beyond that maximum results in a drop in CTE. Compared to the laboratory CTE, the apparent CTE of the slabs reached values up to 60% greater for expansion and 76% greater for curling. The apparent CTE of the USPs reached values up to 38% greater than the laboratory CTE.

The pattern of change of the apparent CTE shown in Figure 5.7 agrees with the pattern observed in PPRC Project 4.58B (7). A similar evolution pattern has been reported for decades based on other laboratory studies (10,11).



### 5.3 SR 113 Slabs Restriction to Expand (Expansion Locking)

The observation of the strain measured with VWSGs in the SR 113 thin COA slabs indicated that the slabs were restricted from expanding in the longitudinal direction during the warm periods. Figure 5.8 and Figure 5.9 are examples showing the mean strain (average of the top and bottom of the slab) measured with VWSGs placed in the longitudinal and transverse directions for a short period of time during the summer (August 2020). The strain in the transverse direction changes according to changes in slab temperature. In contrast, the strain in the longitudinal direction only seems to follow the slab temperature during the coolest period of the day. After the coolest period of each day, the longitudinal strain barely changes as the temperature of the slab changes. This outcome suggests that the transverse joints gap closes and prevents the slabs from continuing to expand as the slab temperature increases. During the cold periods, longitudinal and transverse strains change as the slab temperature changes, shown in the examples in Figure 5.10, Figure 5.11, and Figure 5.12 (November 2019). The slab restriction to expanding is referred in this report as “expansion locking.”

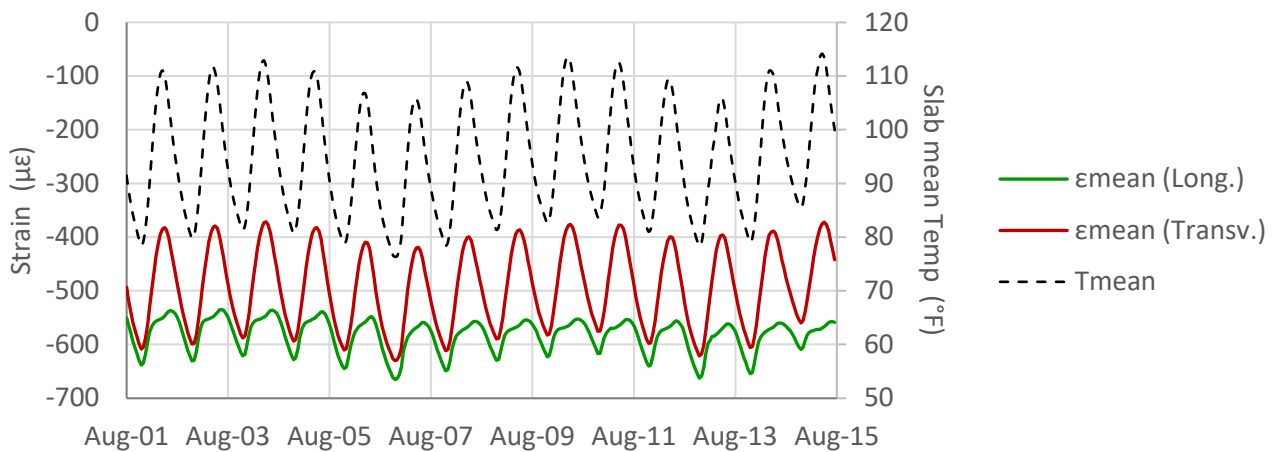
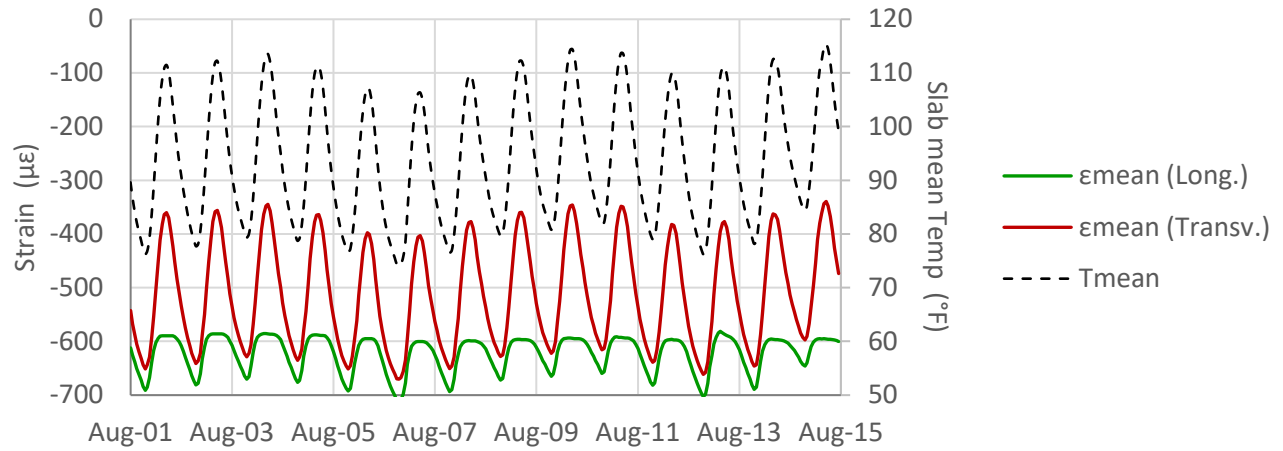
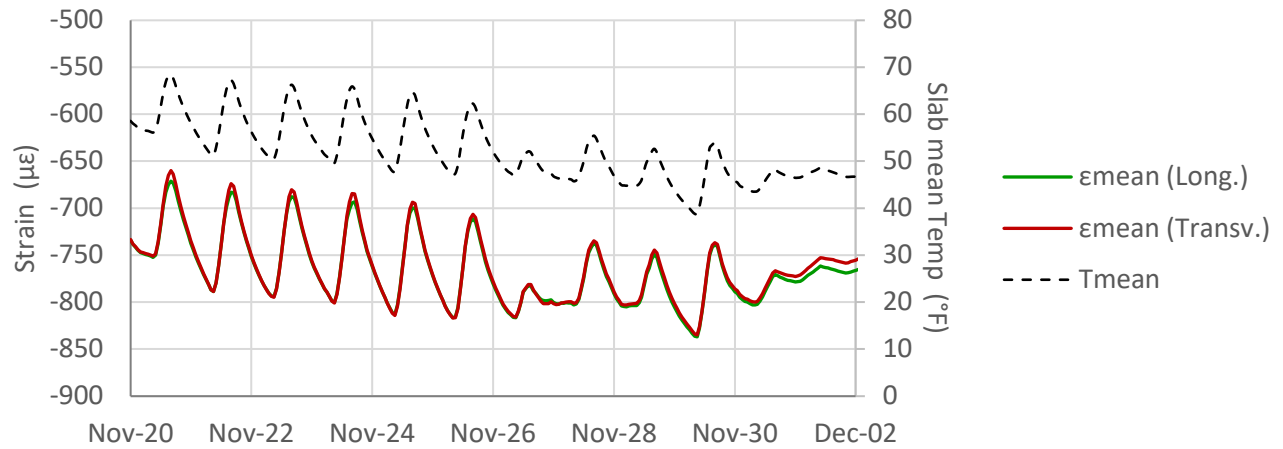


Figure 5.8: Example of slab expansion/contraction during warm season (SR 113, IP A21).



**Figure 5.9: Example of slab expansion/contraction during warm season (SR 113, IP A31).**



**Figure 5.10: Example of slab expansion/contraction during cold season (SR 113, IP A21).**

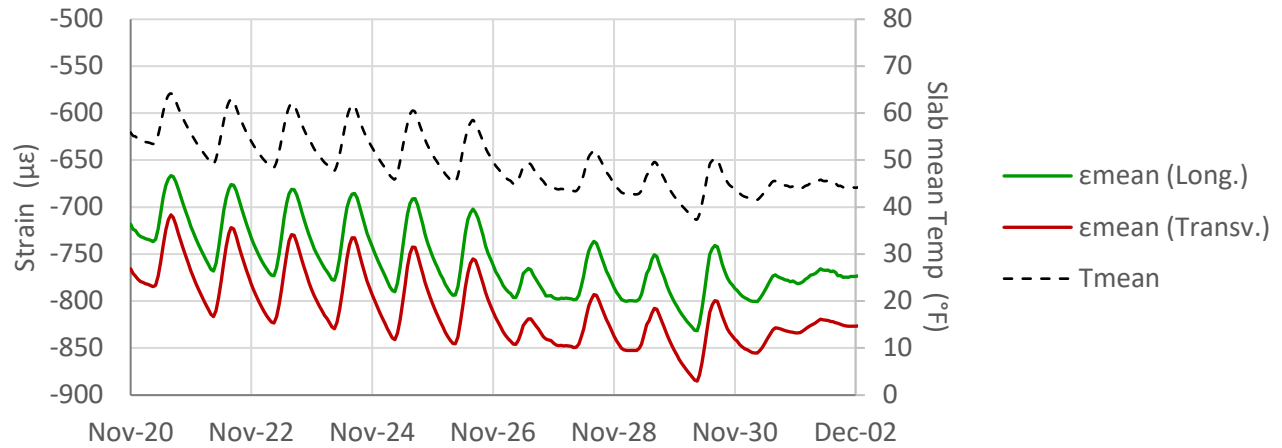


**Figure 5.11: Example of slab expansion/contraction during cold season (SR 113, IP A22).**

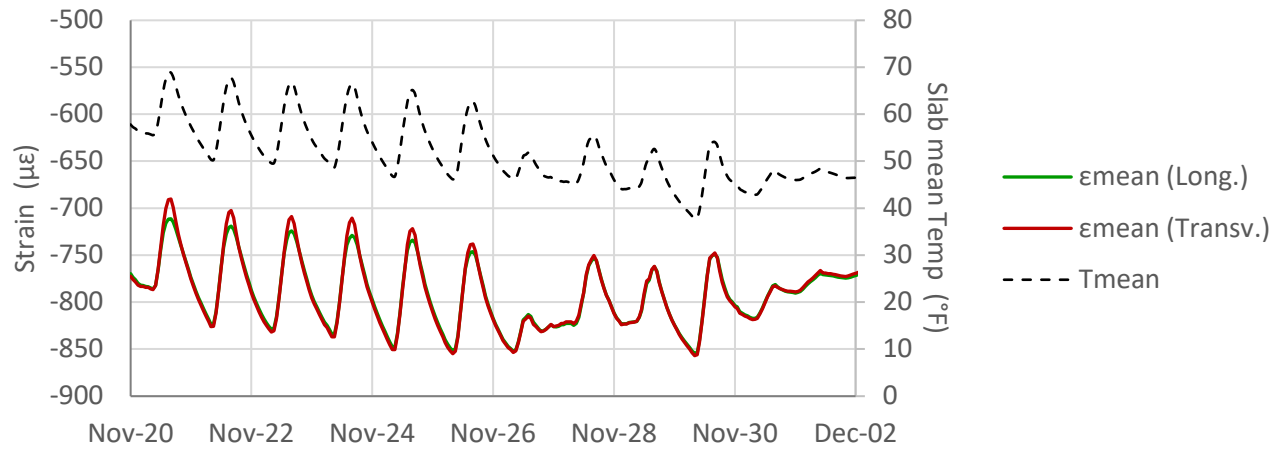


**Figure 5.12: Example of slab expansion/contraction during cold season (SR 113, IP A31).**

The evolution of the expansion locking during the year-and-a-half period presented in this report can be inferred from Figure 5.13, which shows the apparent CTE based on expansion/contraction of the slabs in the longitudinal and transverse directions. Overall, the apparent CTE in the longitudinal direction is much smaller than in the transverse direction, particularly during summer periods. During summer periods, the apparent CTE in the transverse direction increases due to concrete drying while the apparent CTE in the longitudinal direction cannot increase since the slabs are restricted from expanding. The expansion locking was more severe during the second summer (2020) than during the first summer (2019).

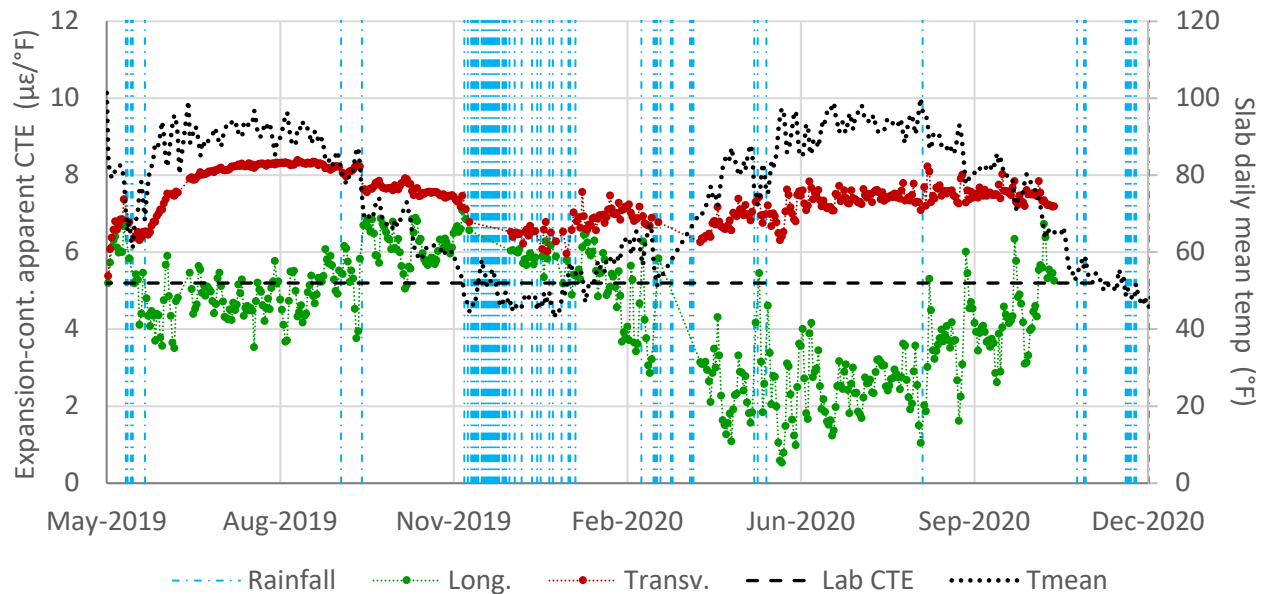


**Figure 5.13: Slab restriction effect on apparent CTE (SR 113, average all instrumented points [IP]).**

It is believed that the clogging of the transverse joints with dirt/dust played a main role in the expansion locking. The raw strain measured with VWSGs is shown in Figure 5.14. The data shown in this graph correspond to the average strain of all VWSGs installed in SR 113 slabs (three instrumented points, four pairs of VWSGs per instrumented point). The slabs experienced a net contraction after the construction. If the transverse joints had remained clean, the slabs should have been free to expand at any time. The fact that the expansion locking is much more severe during the second summer than during the first summer (Figure 5.13) is consistent with the transverse joints clogging during the 2019-20 rainfall season. Part of the dirt/dust might also have come from the grinding residue. (Note: The grinding of Segment A slabs took place in the second half of May 2019.)

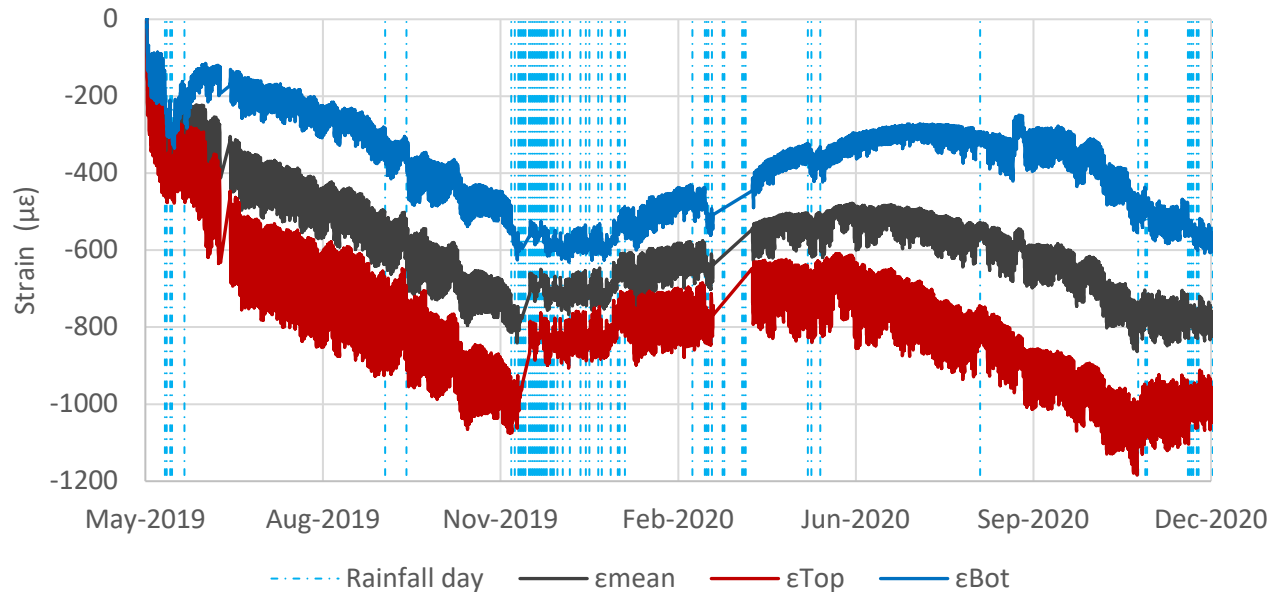


**Figure 5.14: Strain measured in SR 113 slabs (average all IP).**

Figure 5.14 includes the mean strain measured in the thin COA slabs (average of the top and bottom of the slab) together with the extrapolated strain at the top and bottom of the slabs. Figure 5.15 show that the slab contraction versus depth is not uniform, as expected. At the top of the slabs, the slabs contract more than at the bottom, mainly because of the drying shrinkage. Consequently, the compression forces that prevent the slabs from expanding in the longitudinal direction are most likely exerted at the bottom of the slabs. This is likely the reason why little joint spalling was observed in the SR 113 project. The long-term consequences of the slab expansion locking are hard to predict.

#### **5.4 Effect of Experiment Design Variables**

The selection of the three instrumented points (IP A21, IP A22, and IP A31) allowed for an experiment with two variables: slab thickness and curing procedure. IP A21 and IP A22 are located in Section A2 while IP A31 is located in Section A3 (Figure 5.2). The Section A3 slab thickness was originally planned to be 5 in., but the final thickness was 6 in., the same as in the rest of SR 113 project, due to a construction issue (3). Consequently, the effect of slab thickness could not be evaluated. IP A21 and IP A31 can be regarded as replicates because Section A2 and Section A3 only differ in the type of asphalt

base, and this factor was not expected to have considerable impact on the hydrothermal response of the slabs.

The primary curing procedure used in SR 113 thin COA consisted of the application of a standard curing compound (ASTM C309 Type 2, white pigmented, resin based) at a nominal rate of 150 ft<sup>2</sup>/gal. A second curing procedure was tried on a small portion of Section A2 (Figure 5.2). The second curing procedure consisted of the application of a shrinkage reducing admixture (SRA) spray prior to the curing compound. The SRA was applied at a rate of 8.5 oz. per yd<sup>2</sup>. This procedure was successfully used in a previous Caltrans PPRC Project, 4.58B (7). In that study, the SRA spray resulted in a 27% reduction in the differential drying shrinkage. For the SR 113 slabs, however, the application of the SRA spray did not seem to have any effect on the differential drying shrinkage, shown in Figure 5.6 (compare IP A22, where slabs were cured with SRA, to IP A21 where SRA was not applied).

Visual observation of the SRA spray application on the SR 113 slabs indicated that the SRA solution was not absorbed by the concrete surface (3). Based on the same visual approach, the COA slabs cured the same way for PPRC Project 4.58B fully absorbed the SRA solution. This outcome is believed to be due to differences between the concrete mixtures used in the two projects. In particular, it is believed to be related to differences in the water to total cementitious materials (w/cm) ratio and speed of cement hydration. The mixture treated with SRA in PPRC Project 4.58B, where the pavement was designed to be opened to traffic in 10 hours, had a low w/cm ratio, 0.33, and used a large dose of accelerator. Consequently, internal desiccation occurred shortly after concrete placement, and it is believed that the early internal desiccation helped the concrete to absorb the SRA solution in Project 4.58B. On the contrary, the mixture used in SR 113, designed to be opened to traffic in 24 hours, had an intermediate w/cm ratio, 0.43, and did not have accelerator.

## 6 SMOOTHNESS OF THE CONCRETE OVERLAY

The smoothness of the SR 113 thin COA project was evaluated with an inertial laser profiler. The first evaluation was conducted soon after the overlay construction, which took place in October and November 2018 (Segment B) and in April and May 2019 (Segment A). The smoothness was also evaluated after the blanket grinding operation, which took place in April 2019 on Segment B and in the second half of May 2019 on Segment A. Details of the post-construction smoothness and the outcome of the blanket grinding can be found in the earlier UCPRC thin COA project report (3). After the grinding operation, the smoothness of the SR 113 project was periodically evaluated, shown in Table 6.1.

**Table 6.1: Smoothness Evaluations of SR 113 Thin COA Project**

Date	Segment	Number of Passes	Descriptor	Label
2018-11-16	B	3	Before grinding	Pre-Grinding
2019-02-22	B	3	Before grinding	Pre-Grinding
2019-05-13	A	3	Before grinding	Pre-Grinding
2019-06-28	A and B	3	2 months after grinding (dry)	Post-Grinding (2 months)
2019-09-27	A and B	3	5 months after grinding (dry)	Post-Grinding (5 months)
2019-10-11	A and B	10	5 months after grinding (dry)	Post-Grinding (5 months)
2019-12-17	A and B	6	8 months after grinding (wet)	Post-Grinding (8 months)
2020-02-21	A and B	10	10 months after grinding (wet)	Post-Grinding (10 months)
2020-06-29/ 2020-06-30	A and B	13	14 months after grinding (wet)	Post-Grinding (14 months)
2020-10-07	A and B	4	17 months after grinding (dry)	Post-Grinding (17 months)

A minimum of three profiler passes were conducted in each smoothness evaluation (Table 6.1, column 3). The recorded data were analyzed with *ProVAL* software, with the main outcome being the International Roughness Index (IRI). While the IRI was obtained independently for left and right wheelpaths, the average value was considered for the analysis presented in this report. This average is referred to as mean roughness index (MRI) in Caltrans specifications, but it is referred to as the “IRI” in this report.

The IRI evolution pattern of the different SR 113 sections is shown in Figure 6.1. For each smoothness evaluation, the IRI value plotted for each section is the average of all passes. The graph shows that the

smoothness improved considerably (i.e., the IRI decreased) after the grinding. Then, it fluctuated considerably with an overall tendency to increase. In fact, the IRI increased about 50 in./mi. between the December 2019 and October 2020 evaluations. The results presented in Sections 6.1 and 6.2 show that these IRI changes were not related to any structural damage of the concrete overlay or faulting, but to slab curvature due to drying shrinkage.

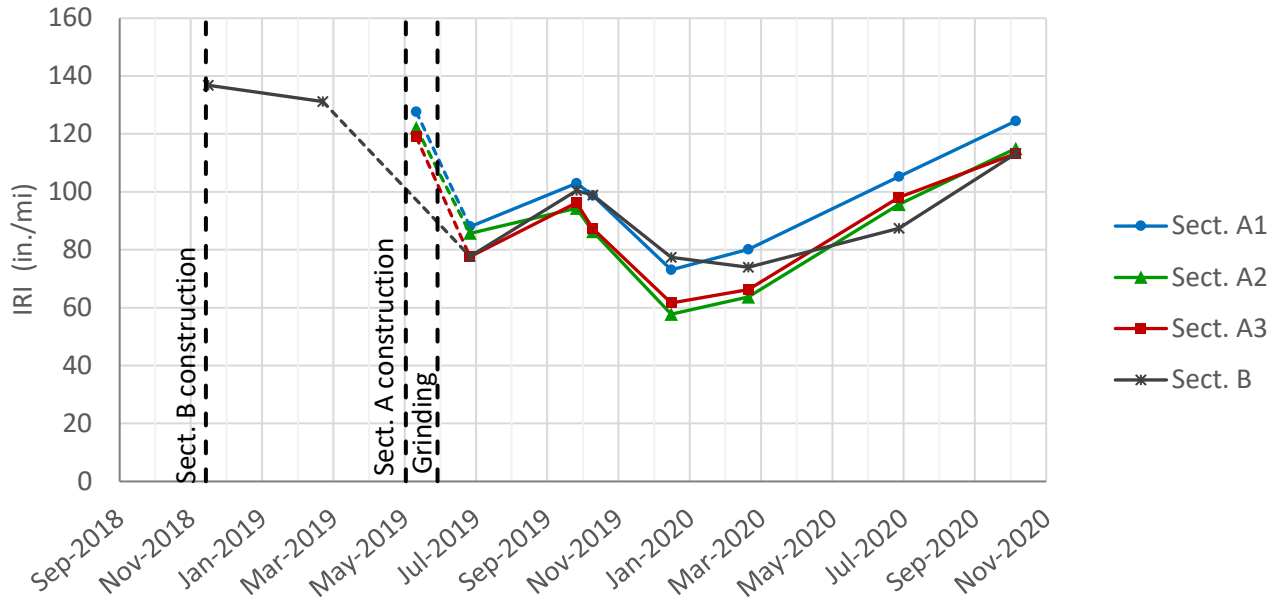


**Figure 6.1: Evolution of IRI.**

## 6.1 Effect of Slab Curvature on IRI

A number of studies show that daily and seasonal changes in slab curvature may considerably impact the IRI (12-14), and this impact was also observed in the SR 113 thin COA project. Figure 6.2 shows the IRI measured in Section A3 in the northbound direction. The IRI measured in each of the evaluations is plotted against the slab equivalent linear temperature difference (ELTD). The ELTD was measured with thermocouples embedded in the slabs. The points correspond to each of the profiler passes for each evaluation. For example, the evaluation “Post-Grinding (10 months)” included 10 passes of the profiler with the ELTD varying between -3°F and +12°F.



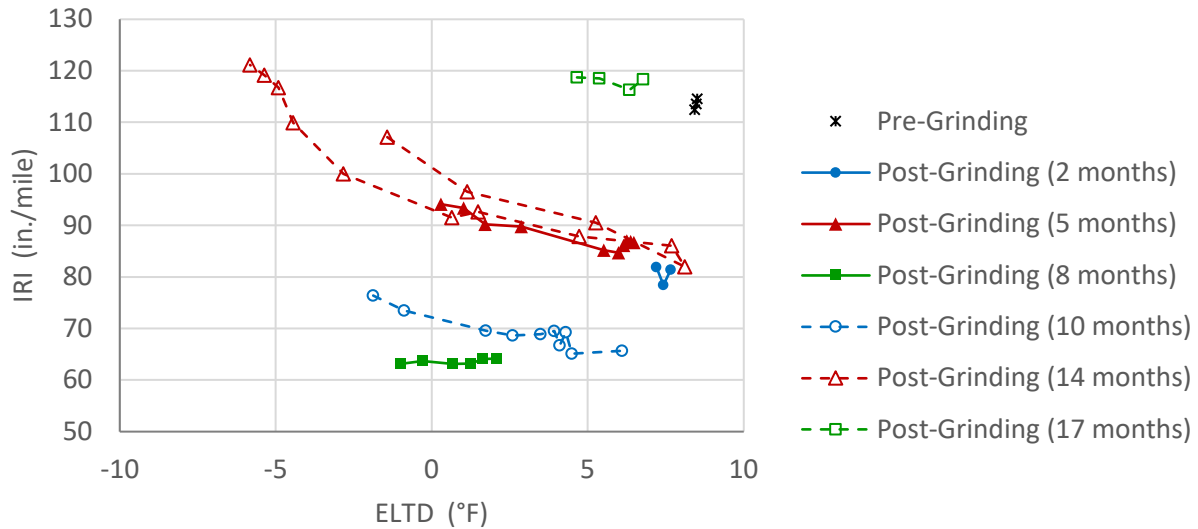


**Figure 6.2: Example of impact of slab temperature gradient on IRI (Section A3, North).**

The “Post-Grinding (14 months)” smoothness evaluation included 13 profiler passes conducted over a 24-hour period. An example of the measured IRI is shown together with the ELTD in Figure 6.3 and with slab curvature in Figure 6.4. The slab curvature was quantified as differential strain,  $\epsilon_{DIFF}$  (the difference between the top and bottom of the slab strains determined from VWSG readings). Figure 6.3 and Figure 6.4 indicate that the variation of the IRI is closer to the slab curvature variation than to the ELTD variation. This finding is not surprising because the ELTD does not directly impact the IRI, but it indirectly impacts it through the change in slab curvature. Another limitation of the ELTD is that the curvature of the slabs is not only related to thermal gradients but to differential drying shrinkage as well, which changes seasonally. This is the reason why the ELTD fails to explain IRI changes from one evaluation to another, shown in Figure 6.2. When the IRI data shown in Figure 6.2 are plotted against slab differential strain, all IRI evaluations collapse onto a single line, shown in Figure 6.5.

The single line in Figure 6.5 indicates that the changes in IRI were not related to any structural damage in the pavement but to changes in slab curvature. The slab curvature changes because of the changes in thermal gradient through the slab thickness and the changes in differential drying shrinkage. The data shown in Figure 6.5 is only an example, and a similar pattern was observed in the rest of the sections.

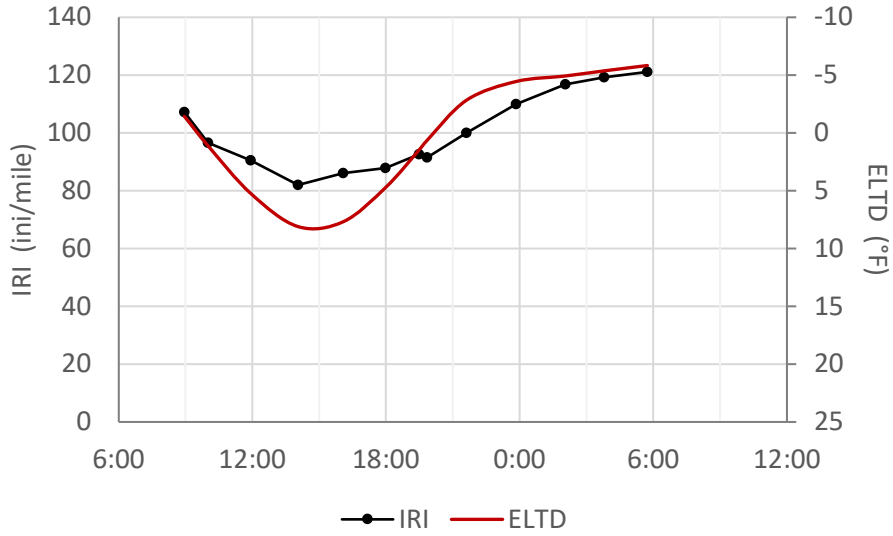


**Figure 6.3: Example of diurnal evolution of IRI and ELTD (Section A3, North, evaluation Post-Grinding [14 months]).**

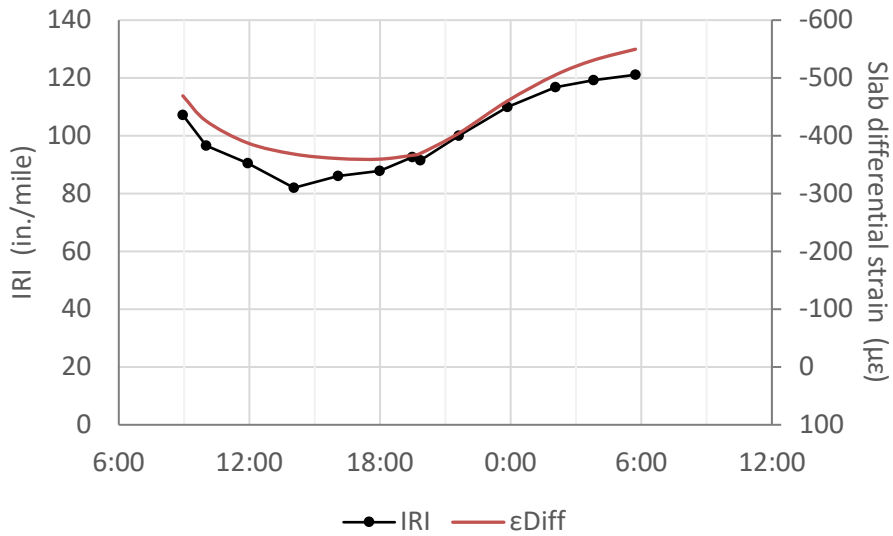


**Figure 6.4: Example of diurnal evolution of IRI and slab curvature (Section A3, North, evaluation Post-Grinding [14 months]).**

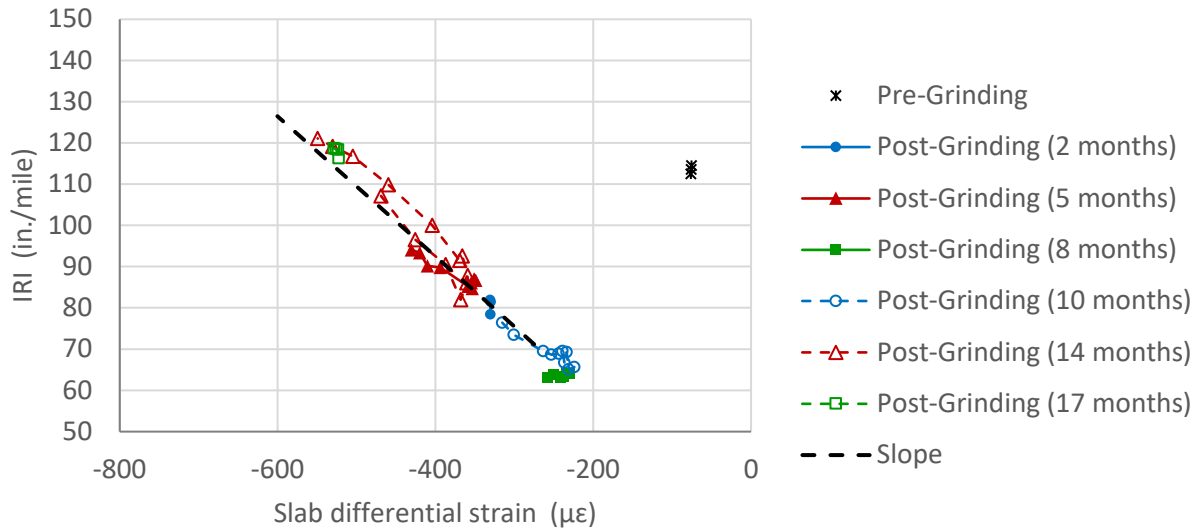


**Figure 6.5: Example of impact of slab curvature on IRI (Section A3, North).**

## 6.2 Evolution of Slab Curvature-Corrected IRI

The ratio between changes in IRI and differential strain ( $\Delta\text{IRI}/\Delta\epsilon_{\text{DIFF}}$ ) was around  $-0.150$  in./mi./ $\mu\epsilon$  for all COA sections (see Slope series in Figure 6.5). The  $-0.150$  value is close to the theoretical slope of  $-0.200$  in./mi./ $\mu\epsilon$  obtained with *ProVAL*. The theoretical slope was determined by generating synthetic profiles that included different curvature levels and analyzing the synthetic profiles with *ProVAL*. The slope of the IRI versus  $\epsilon_{\text{DIFF}}$  relationship ( $-0.150$  in./mi./ $\mu\epsilon$ ) was used to correct the measured IRI by removing the slab curvature effect, as explained in the following discussion.

Each pass of the inertial profiler has an associated slab curvature. As previously explained, the curvature was quantified with  $\epsilon_{\text{DIFF}}$ , the difference between the top and bottom of the slab strains based on VWSG readings. The average of the three instrumented points was used regardless of the section under consideration (A1, A2, A3, and B). Once  $\epsilon_{\text{DIFF}}$  and  $\Delta\text{IRI}/\Delta\epsilon_{\text{DIFF}}$  are known, the measured IRI can be extrapolated to an  $\epsilon_{\text{DIFF}}$  value that is constant in time,  $\epsilon_{\text{DIFF,REF}}$ , by applying Equation 6.1. Because the extrapolated IRI will not be affected by the changes in slab curvature, it is referred to as the “corrected IRI” in this report. The changes in the corrected IRI reflect changes in the surface profile that are not related to slab curvature changes but to faulting, slab rocking, slab settlement, cracking, and other non-recoverable phenomena.

$$\text{IRI}(\text{corrected}) = \text{IRI}(\text{measured}) + (\epsilon_{\text{DIFF}} - \epsilon_{\text{DIFF;REF}}) \cdot \frac{\Delta \text{IRI}}{\Delta \epsilon_{\text{DIFF}}} \quad (6.1)$$

A value of  $-275 \mu\epsilon$  was adopted for the reference differential strain ( $\epsilon_{\text{DIFF;REF}}$ ). This value is the minimum  $\epsilon_{\text{DIFF}}$  (in absolute value) measured during the profiler evaluations. The negative sign indicates that the slab curvature is concave upwards.

The evolution of the corrected IRI is shown in Figure 6.6, which shows that the IRI remained constant after the grinding operation. The fluctuation observed in Section B is most likely because the slab differential strain adopted for the curvature correction was not measured in Section B but in Section A2 and Section A3. The Section B slab curvature may differ from the curvature of the Section A2 and Section A3 slabs because the Section B overlay was built about six months before the Section A2 and Section A3 overlays, and the Section B slabs are slightly thicker than the Section A2 and Section A3 slabs (around 1 in. thicker).

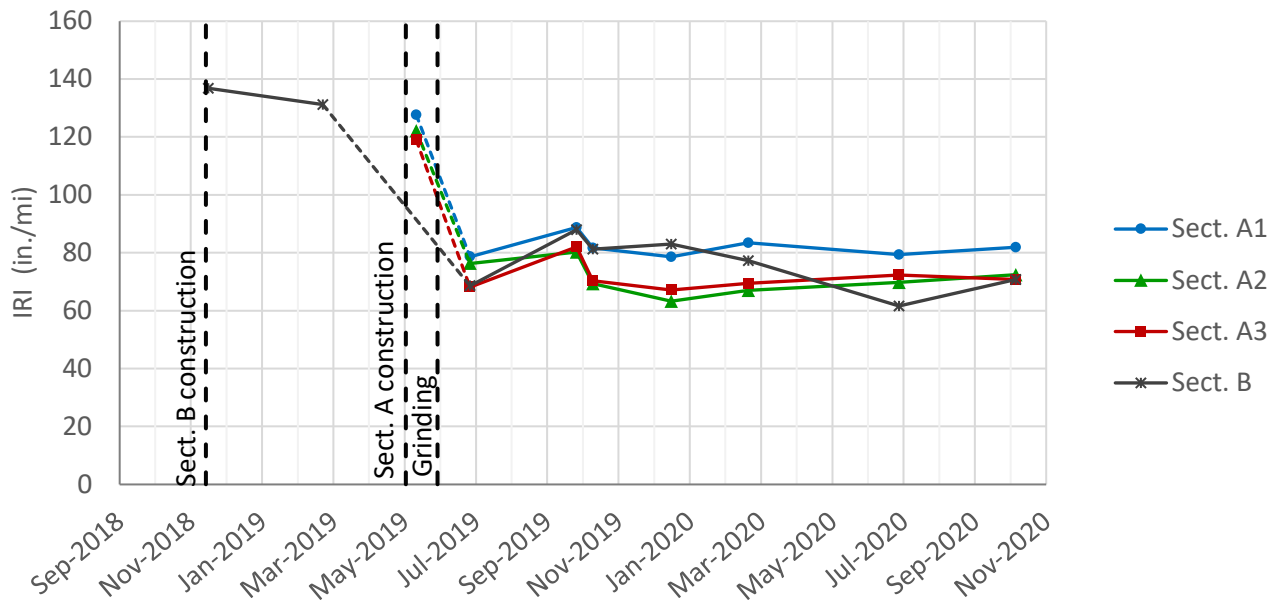


**Figure 6.6: Evolution of slab curvature-corrected corrected IRI.**

## 7 SURFACE MACROTEXTURE OF THE CONCRETE OVERLAY

The surface macrotexture was evaluated with a laser texturometer mounted on the same vehicle where the profiler is mounted. For this reason, the macrotexture was evaluated together with the smoothness. The texturometer data were processed to determine the mean profile depth (MPD) of the pavement surface. A limitation of the laser texturometer is that the texture is mainly due to the longitudinal tining and/or grinding and is consequently difficult to capture with the laser moving the longitudinal direction.

The MPD evolution is shown in Figure 7.1. As expected, the MPD increased after the grinding operation. The grinding operation leaves a surface with closely spaced grooves separated by ridges (Figure 7.2). After the grinding, the MPD slowly decreased, most likely due to the breaking of the tips of the concrete ridges left by the grinding operation.

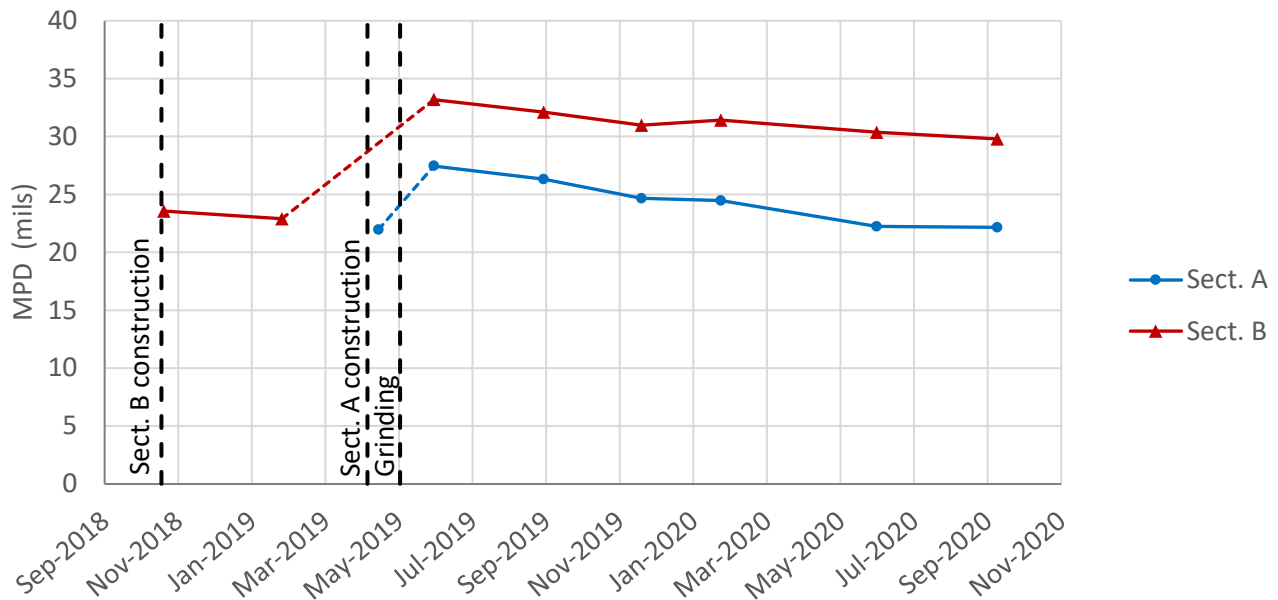


Figure 7.1: Evolution of the mean profile depth (MPD).



**Figure 7.2: Grinded concrete surface.**

## 8 STRUCTURAL EVALUATION OF THE THIN COA SECTIONS

---

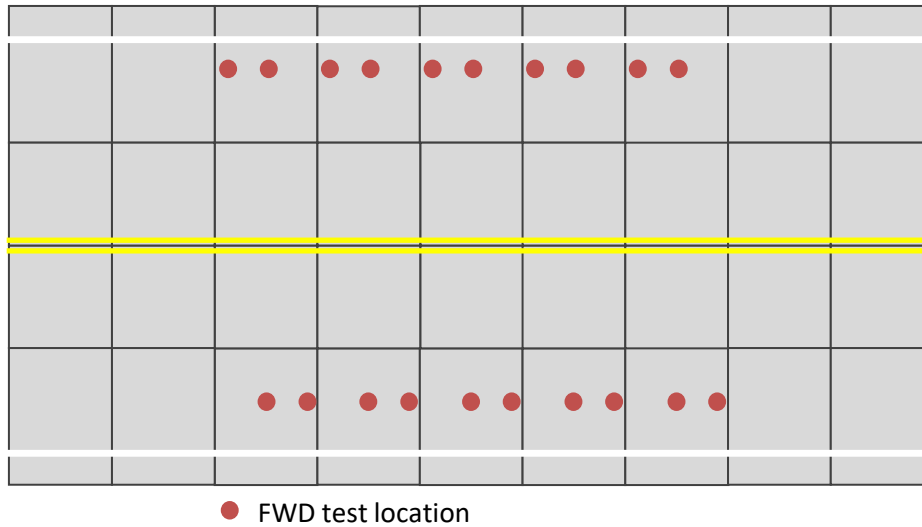
### 8.1 Evaluation of the Thin COA Sections Under Falling Weight Deflectometer Loading

The structural capacity of the thin COA was periodically evaluated with the FWD. The FWD evaluations had three main goals:

- Determine structural differences between sections (Figure 2.1) and FWD evaluations (Summer 2019, Winter 2019-20, and Summer 2020). The differences between FWD evaluations may indicate changes in the structural capacity of the COA. This goal is elaborated in Section 8.1.2.
- Backcalculate the structural parameters of the COA, in particular the slab-base bending stiffness and the subbase-subgrade modulus of subgrade reaction. This goal is elaborated in Section 8.1.3.
- Determine the LTE across the transverse joints. This goal is elaborated in Section 8.1.4.

#### 8.1.1 *Falling Weight Deflectometer Sections and Evaluations*

A total of 20 FWD sections were selected for periodic evaluation, 10 in the northbound direction and 10 in the southbound direction. Each FWD section comprised five consecutive slabs, and each slab was tested at two locations, slab center and leave joint, shown in Figure 8.1. The post mile (PM) of the different FWD sections is shown in Table 8.1. All FWD sections slabs were marked with paint so that they can be located easily for future periodic evaluations.



Note: The figure shows two FWD sections, one in each direction.

**Figure 8.1: Example of FWD section layouts.**

**Table 8.2: Location of FWD Sections**

FWD Section	Segment	Test Section <sup>a</sup>	PM
A-NB1 and A-SB1	A	A1	12.050
A-NB2 and A-SB2	A	A2	12.356
A-NB3 and A-SB3	A	A2	12.364
A-NB4 and A-SB4	A	A3	12.374
A-NB5 and A-SB5	A	A3	12.512
B-NB1 and B-SB1	B	B	14.842
B-NB2 and B-SB2	B	B	15.460
B-NB3 and B-SB3	B	B	16.173
B-NB4 and B-SB4	B	B	16.872
B-NB5 and B-SB5	B	B	17.570

<sup>a</sup> Test sections (A1, A2, A3, and B) shown in Figure 2.1.

Three FWD evaluations were conducted. The dates of the three FWD evaluations are shown in Table 8.2.

**Table 8.3: FWD Evaluations Dates**

FWD Evaluation	Date
Summer 2019	August 19-21, 2019
Winter 2019-20	January 28-30, 2020
Summer 2020	August 10-11, 2020



In each of the three FWD evaluations, each of the 20 FWD sections was tested twice, in the morning and in the afternoon. The duplicate testing was conducted to capture two thermal conditions of the slabs: relatively cold in the morning and relatively warm in the afternoon.

**8.1.2 Structural Differences Between Sections and Evaluations**

The box plots of the deflections measured at the center of the slabs in each of the sections and for each of the FWD evaluations (Summer 2019, Winter 2019-20, and Summer 2020) are shown in Figure 8.2. Similarly, the LTE and deflections measured at the transverse joints are shown in Figure 8.3 and Figure 8.4, respectively. The deflections and LTE in all figures correspond to an FWD loading of 15.7 kips.

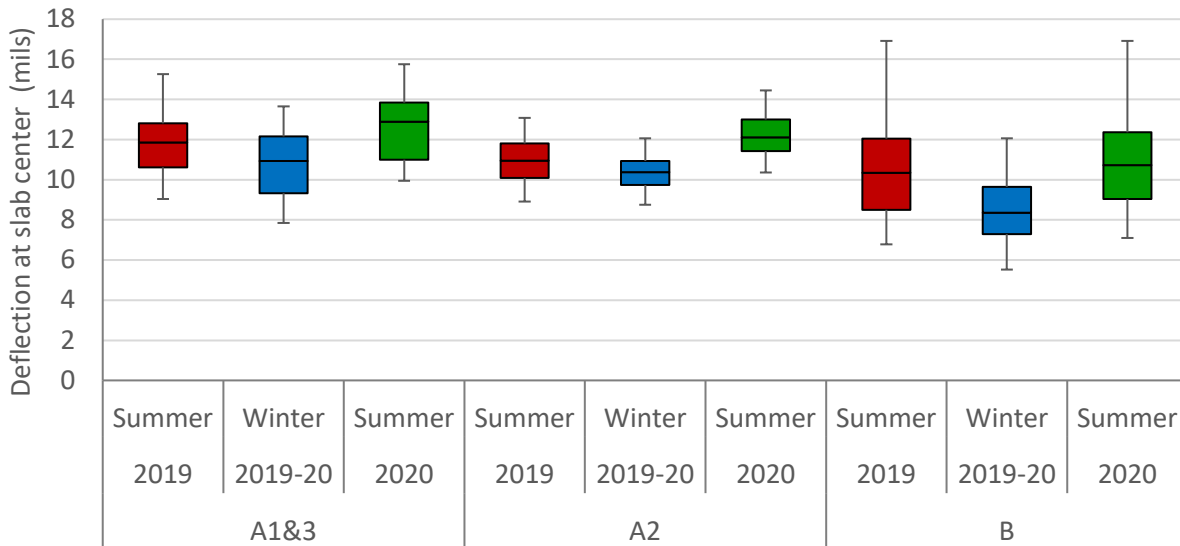


**Figure 8.2: Deflection at slab center (FWD loading = 15.7 kips).**

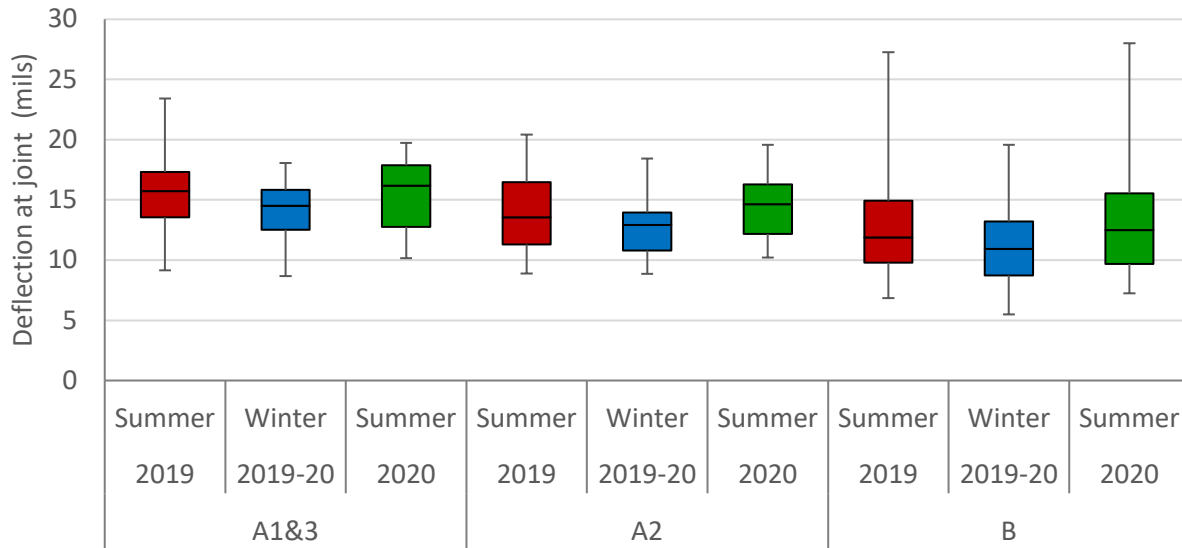


**Figure 8.3: Deflection at transverse joint (FWD loading = 15.7 kips).**

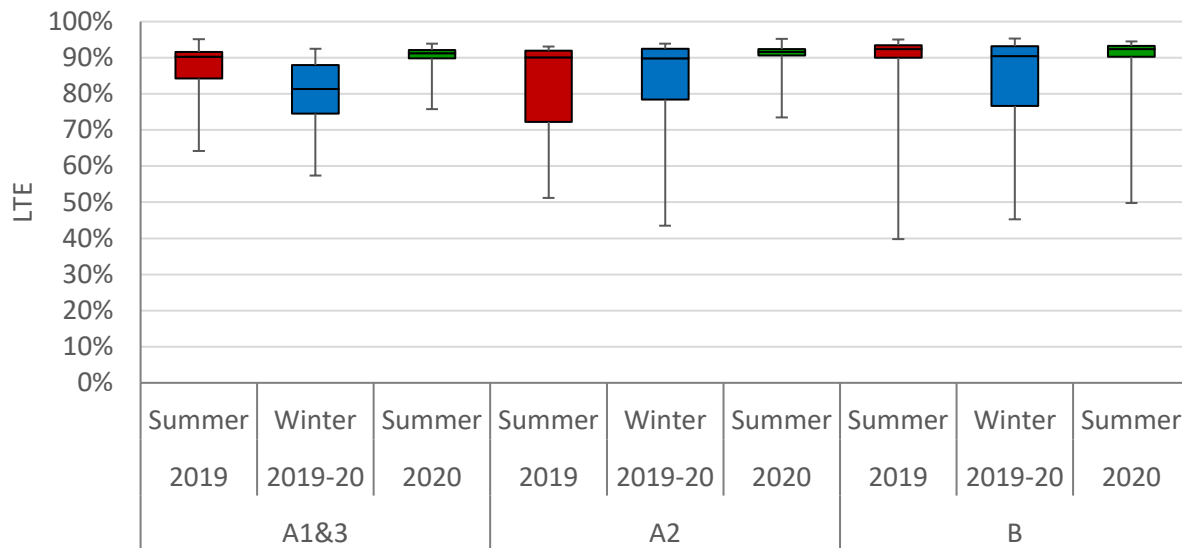


**Figure 8.4: Transverse joint LTE (FWD loading = 15.7 kips).**

The data presented in Figure 8.2 to Figure 8.4 suggest a seasonal variation of the slab structural responses under the FWD loading. The deflections and LTE are higher in the summer than in the winter, and the analysis of variance (ANOVA) indicates that the differences between the two seasons are statistically significant. The LTE is higher in the summer than in the winter because the transverse joints close as the slabs expand due to the high summer temperatures (15). The deflections are larger in the

summer than in the winter likely because the underlying support of the slabs is lost as the slabs curl (concave upward) during summer due to the drying shrinkage. This belief is supported by the fact that the backcalculated modulus of subgrade reaction was smaller in the summer than in the winter (Section 8.1.3).

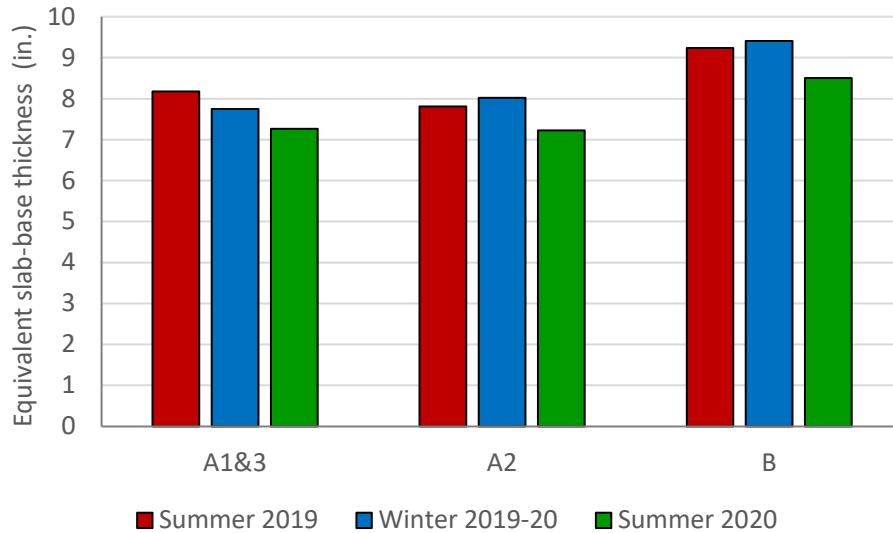
The data presented in Figure 8.2 to Figure 8.4 do not show evident differences between structural sections. Deflections are slightly smaller in Section B than in Sections A1, A2, and A3, and the ANOVA indicates that the differences between the two groups of sections (A and B) are statistically significant. This outcome is likely due to the higher overlay thickness of Section B compared to the other sections. Measurements taken manually on the slab edges just after the overlay construction indicated that the Section B overlay thickness was 1 to 3 in. thicker than the 6 in. target (1). The same manual measurements indicated that the overlay thickness in Sections A1, A2, and A3 was 6 to 7 in., close to the 6 in. target. The ANOVA indicates that the LTE differences between sections are not statistically significant.

### **8.1.3 Backcalculation of the Structural Parameters of the Thin COA Structure**

The structural parameters of the thin COA were backcalculated by using the AREA method adapted for short slabs (16). This backcalculation procedure determines two structural parameters: the slab bending stiffness and the modulus of subgrade reaction. The bending stiffness of a slab depends on its modulus of elasticity and its thickness. Because the bending stiffness is known from laboratory testing, the thickness can be determined. Conceptually, the thickness determined this way represents the concrete slab-asphalt base bilayer structure. This bilayer structure is referred to as the “equivalent slab” in this report. The backcalculated modulus of subgrade reaction represents, conceptually, the combination of the subbase and the subgrade.

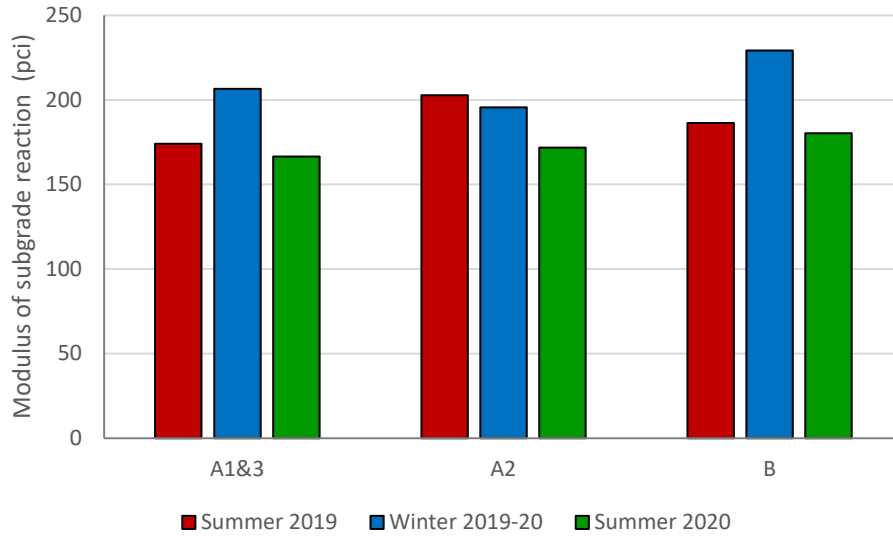
The backcalculated equivalent slab thickness is shown Figure 8.5. Because the concrete overlay was built thicker in Section B than in the sections A1, A2, and A3, the equivalent slab thickness is larger in Section B than in the Sections A1, A2, and A3. The differences between the actual thickness of the concrete overlay (6 to 7 in. in Section A1 to Section A3 and 7 to 9 in. in Section B) and the values shown in Figure 8.5 are due, in theory, to the contribution of the asphalt base bonded to the slab. Because

Figure 8.5 values are not much larger than the actual thickness of the concrete overlay, it may be concluded that the asphalt base bonded to the slab does not contribute much structurally. This conclusion was supported by the fact that the condition of the asphalt base that remained after milling was very poor (3).



**Figure 8.5: Backcalculated thickness of the slab-base bilayer structure.**

The backcalculated modulus of subgrade reaction is shown in Figure 8.6. While the backcalculated values do not differ much between sections, they are larger in the winter than in the summer. This finding is consistent with a loss of slab support during the summer as compared to the winter because the slab-base system is in contact with the underlying materials less in the summer than in the winter, most likely a consequence of the warping created by the drying shrinkage. As shown in Figure 5.5, the warping of the slabs during Summer 2019 and 2020 resulted in the top of the slabs shrinking 400 to 500  $\mu\epsilon$  compared to the bottom of the slabs. It is evident that such warping has a negative impact on the slab underlying support, and it would explain, at least in part, why the backcalculated modulus of subgrade reaction is higher in the winter than in the summer.



**Figure 8.6: Backcalculated modulus of subgrade reaction of the subbase-subgrade system.**

#### **8.1.4 Load Transfer Efficiency of the Transverse Joints**

On average, the LTE of the transverse joints remained relatively high. In the summer evaluations, the average LTE (the average of five joints from 20 FWD sections) was around 88% while in the winter evaluation the average LTE was 82%, shown in Figure 8.7. While the average LTE was relatively good, it still reached values as low as 40% in some tests. No distinction is made between different sections since the ANOVA indicated that the LTE differences between sections are not statistically significant. While Figure 8.7 includes the LTE box plots, Figure 8.8 includes the cumulative histograms. The LTE of the transverse joints was mainly over 80%, but it also reached considerably low values (below 70%) in some tests, particularly during the winter evaluation. In the winter evaluation, around 20% of the FWD tests resulted in less than 70% LTE.

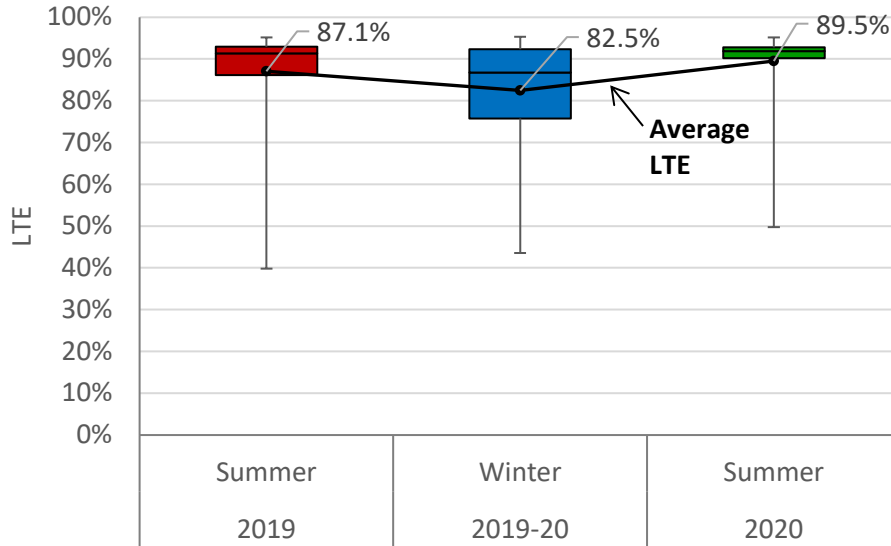


**Figure 8.7: Seasonal evolution of transverse joint LTE.**

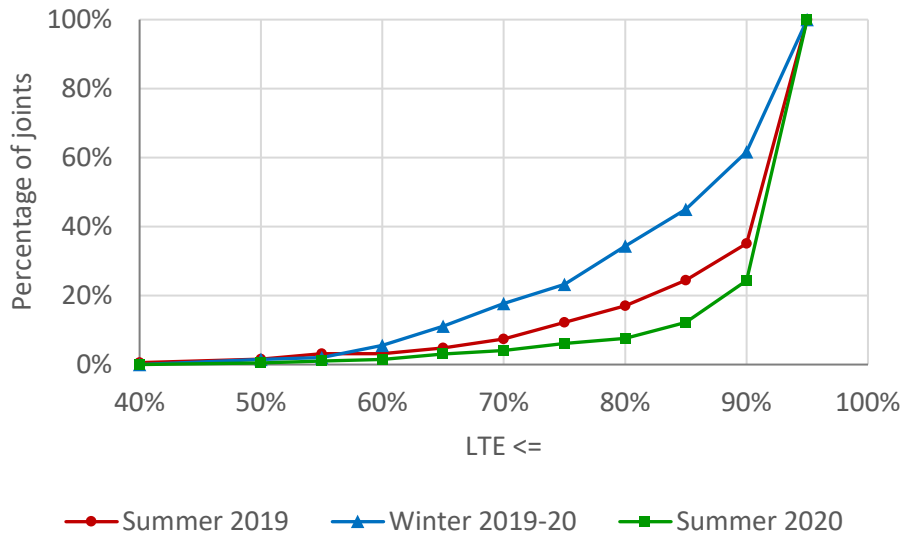


**Figure 8.8: LTE histogram.**

The relatively low LTE values obtained for some of the tested joints contrast with the LTE measured in the COA sections with 6x6 slabs in PPRC Project 4.58B, an earlier Caltrans research project (17). The LTE of the 4.58B sections were systematically over 70% before the accelerated load testing with the Heavy Vehicle Simulator (HVS), shown in Figure 8.9. Further, the LTE of the 4.58B sections showed hardly any seasonal variation, shown in Figure 8.10. This figure includes a comparison between the LTE

measured in the SR 113 and 4.58B sections. Based on this comparison, the LTE of the SR 113 sections has a very strong seasonal variation. Also, while the majority of the FWD tests conducted on the 4.58B sections resulted in a relatively narrow LTE range, from 80% to 90%, the tests conducted on SR 113 resulted in a much wider range, regardless of the testing season. In the three FWD evaluations conducted on SR 113, the LTE varied from very high values, over 90%, to values as low as 40%.

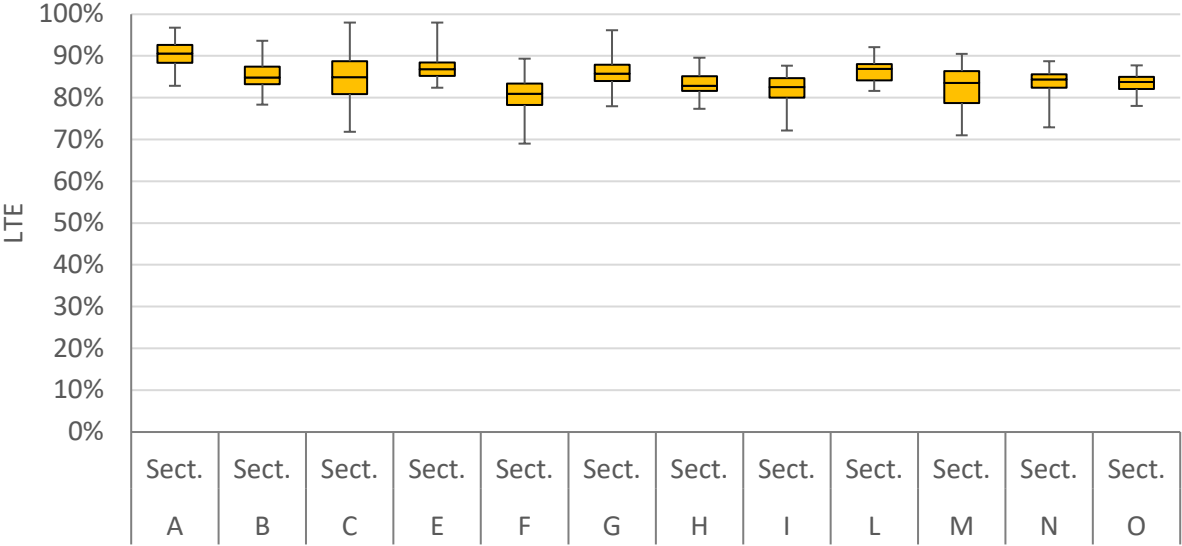


**Figure 8.9: LTE measured in 4.58B thin COA sections with 6x6 slabs (pre-HVS testing evaluation).**

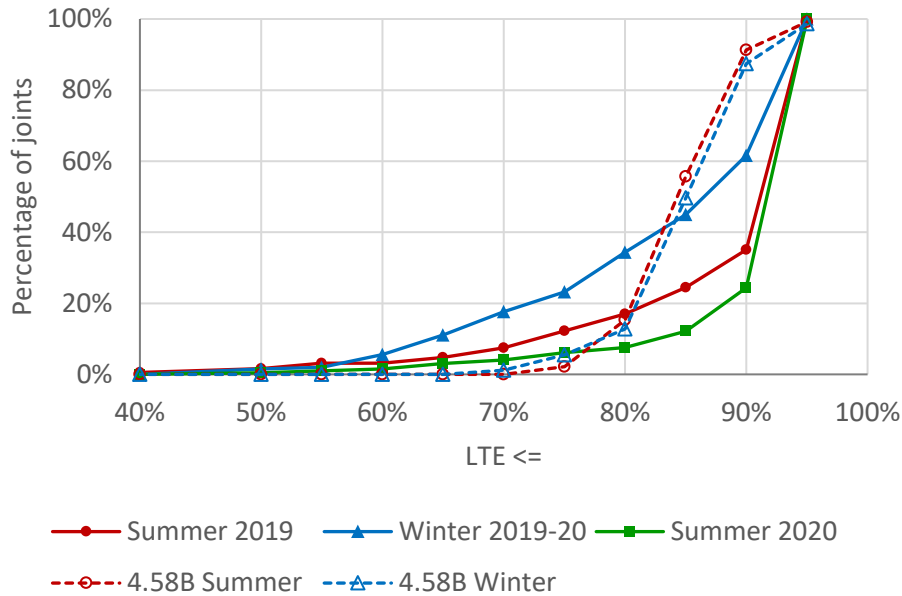


**Figure 8.10: Comparison between LTE of SR 113 and 4.58B thin COA sections with 6x6 slabs.**

The low LTE obtained in some of the tests conducted on SR 113 sections is a concern since poor-performing joints may result in premature slab cracking and faulting. Research, presented in the following discussion, was conducted in order to determine the reason or reasons why the LTE reached low values for some of the tests and why the LTE showed high seasonal variation.

**8.1.5 LTE-Deflection High-Low Pattern**

The analysis of FWD deflections and LTE showed a high-low pattern where transverse joints with good and poor LTE (low and high deflection, respectively) alternated, shown in Figure 8.11. This figure includes all FWD tests (20 FWD sections, three FWD evaluations). For some of the FWD sections, the joint numbers (1 to 5) were shifted by minus 1 so the assigned number of the poor LTE joints would be even numbers and the good LTE joints would be odd numbers. The different performance of the joints with poor and good LTE is also shown in Figure 8.12, where the performance of the joints with poor LTE showed a strong seasonal variation.



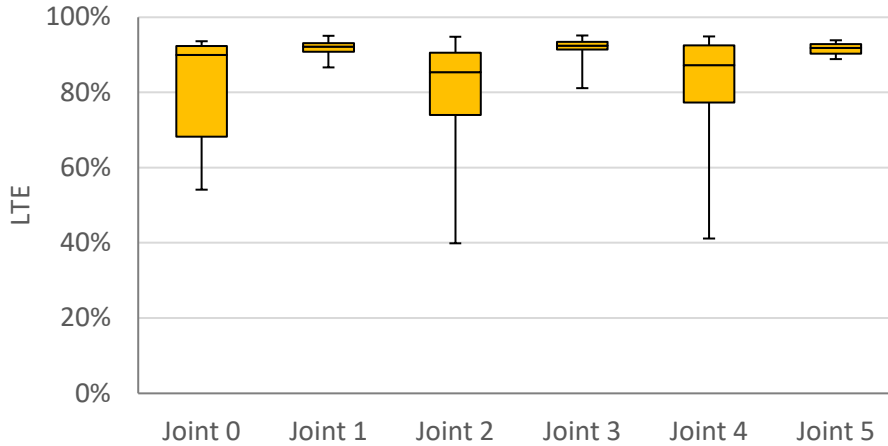


**Figure 8.11: LTE high-low pattern (all FWD sections, three evaluations).**

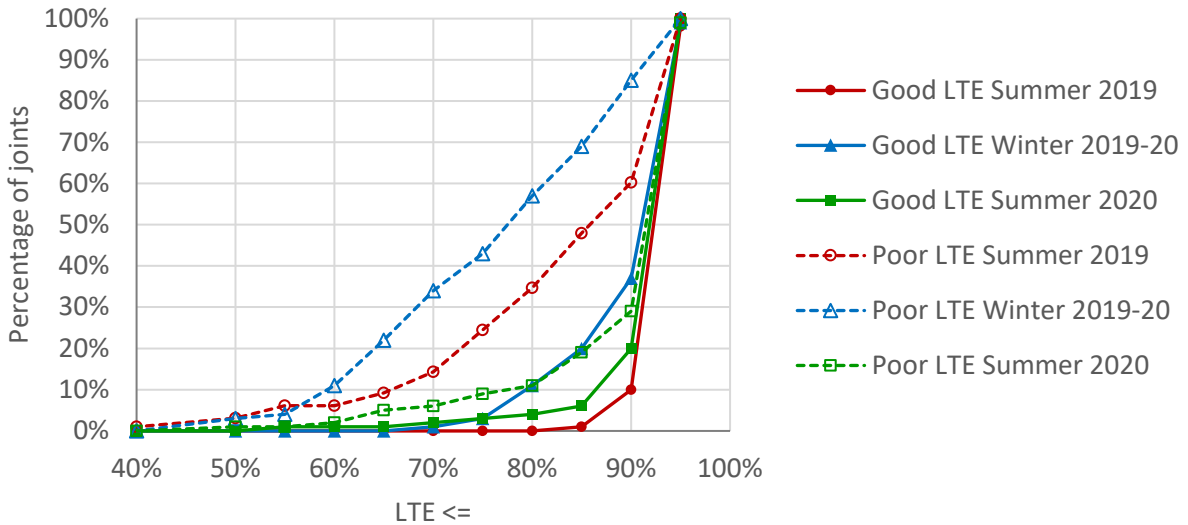


**Figure 8.12: LTE histogram of joints with good and poor LTE performance.**

## 8.2 Transverse Joint Deployment

The LTE-deflection high-low pattern raised the question of whether all the transverse joints had deployed, and this was the motivation for the coring campaign presented in Chapter 3. As previously discussed, three locations were evaluated by coring two consecutive transverse joints, one with good LTE and one with poor LTE. In two of the three locations that were evaluated, the joint with good LTE had not deployed, which resulted in an effective slab length of 12 ft. In the third case, the two

transverse joints had deployed, but the LTE-deflection high-low pattern was clear. In this third case, the “dominant joints” are most likely absorbing the opening of the adjacent joints. Because of its larger opening, a dominant joint would result in smaller LTE than adjacent joints.

The difference between deflection at the slab center and the transverse joint is an indicator of transverse joint deployment. For the three FWD locations evaluated, when the transverse joint with good LTE did not deploy, the deflection was almost the same at the slab center and the transverse joint, shown in Figure 8.13 (left). When the transverse joint with good LTE deployed, there was some difference between the deflection at the slab center and the transverse joint, shown in Figure 8.13 (right). A total of 40% of the FWD sections presented a deflection pattern close to the one shown in Figure 8.13 (left). In these sections, most likely only one of every two transverse joints deployed. The remaining 60% of the FWD sections presented a pattern close to the one shown in Figure 8.13 (right). Most likely, all the transverse joints deployed in these FWD sections. In summary, it is estimated that around 80% of the transverse joints deployed (100% of the joints of 60% of the FWD sections plus 50% of the joints of 40% of the FWD sections).

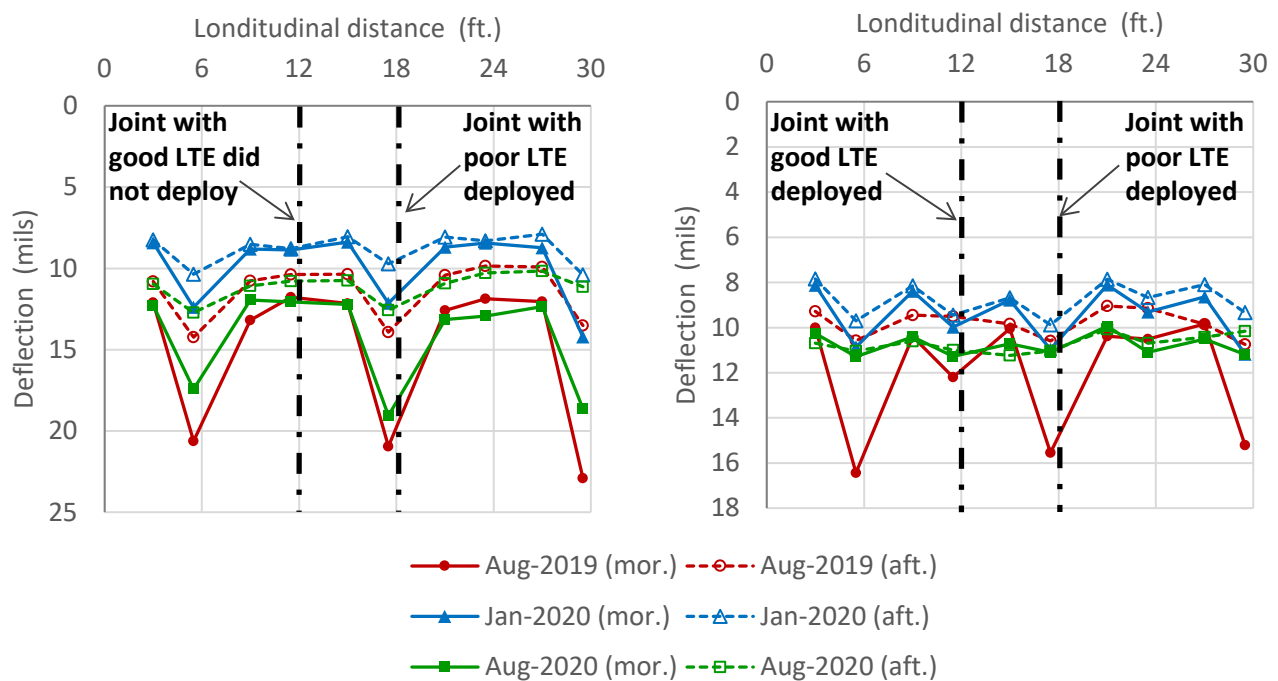


**Figure 8.13: FWD assessment of joint deployment (left, FWD Section B-NB3; right, Section A-SB1).**

It should be noted that while all the transverse joints seemed to have deployed in 60% of the FWD sections, these sections still showed a clear LTE-deflection high-low pattern (e.g., Figure 8.13, right). The high-low pattern was equally noticeable in the FWD sections where only one of every two transverse joints deployed (12 ft. long slabs) and the FWD sections where all the transverse joints deployed (6 ft. long slabs). This conclusion is supported by the data shown in Figure 8.14 where the joints with poor LTE showed similar performance regardless of the level of transverse joint deployment (i.e., regardless of the effective slab length). Again, this finding indicates that the LTE-deflection high-low pattern is not only related to the lack of joint deployment but also to a more general phenomenon, the presence of dominant joints.

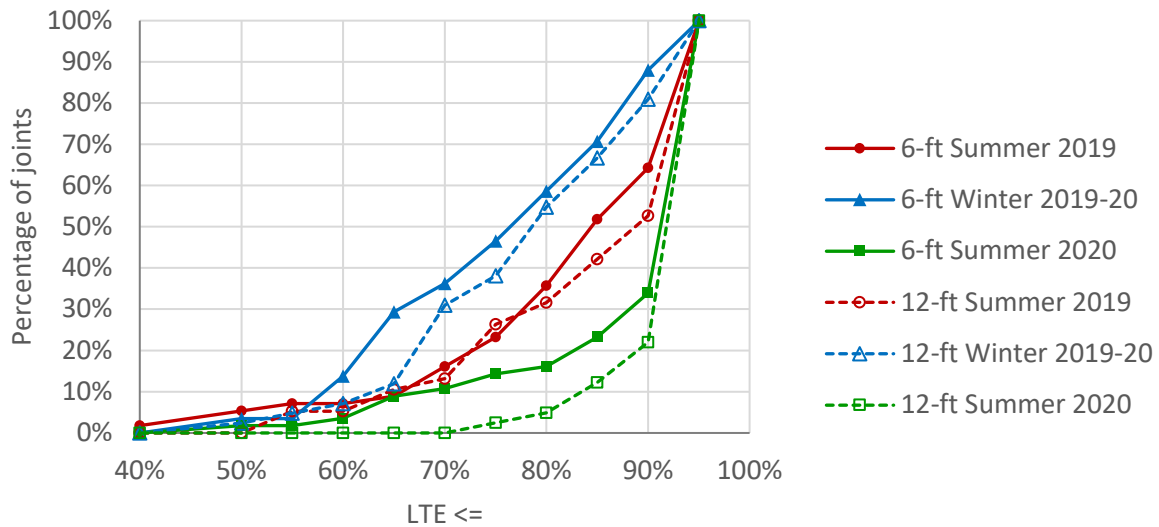


**Figure 8.14: LTE histogram of joints with poor LTE performance.**

This research tested the hypothesis that the COA transverse joints that deploy first remain wider and result in a lower LTE than the other joints over the entire life of the pavement, or at least for a considerable portion of it. This hypothesis is validated below. The Woodland SR 113 thin COA was tested by mapping the openings of the Segment A southbound lane transverse joints six days after the overlay construction. The transverse joints that had already deployed are marked with an arrow (→) in Figure 8.15. Only the portions of the Segment A southbound lane that correspond to the FWD sections are shown in this figure. Also marked (with dashed line) in the figure are the joints with poor LTE in the FWD testing. This figure shows that every other transverse joint performed poorly, which resulted in

the LTE-deflection high-low pattern previously discussed. Interestingly, the layout of the LTE-deflection high-low pattern of all the FWD sections can be predicted based on the layout of the transverse joints that deployed early. In other words, the transverse joints that deployed early became dominant joints that absorb the opening of adjacent transverse joints and, consequently, perform poorly. In addition, the LTE-deflection high-low pattern of the northbound and southbound lanes matched. The two lanes were paved independently—first the southbound lane and then the northbound lane a week later. The matching indicates that the opening and closing of southbound lane transverse joints triggered the deployment of the northbound lane transverse joints. This phenomenon is similar to the “sympathy cracking” that has been described in the context of early-age cracking of concrete pavements (18).

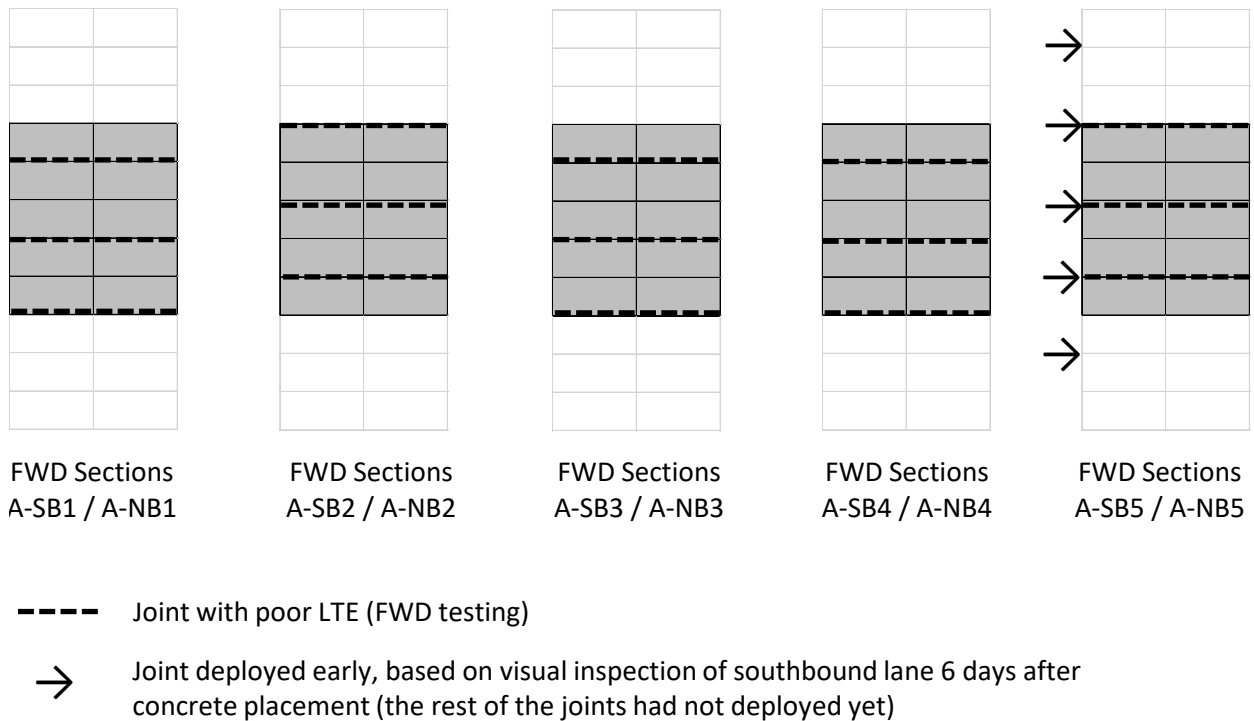


**Figure 8.15: Early joint deployment and LTE comparison.**

### 8.3 Ambient Environment Effects on Load Transfer Efficiency

As previously discussed, the performance of the joints with poor LTE showed strong seasonal variation, with the LTE being higher in the summer than in the winter (Figure 8.12). This finding was expected, and it can be attributed to the closing of the transverse joints during the summer as the slabs expand

due to the warm temperatures (15). For a single day, the effect of the slab temperature on the LTE can be determined by comparing the LTE in the morning to the LTE in the afternoon, shown in the Figure 8.16 example, which includes data for the FWD Section B-NB3. Only one of every two transverse joints deployed in this section (Joint 1, Joint 3, and Joint 5). The LTE of these joints increased from the morning to the afternoon, and this increase is attributable to the closing of the transverse as the slab temperature increases. A similar pattern was observed in the other FWD sections.

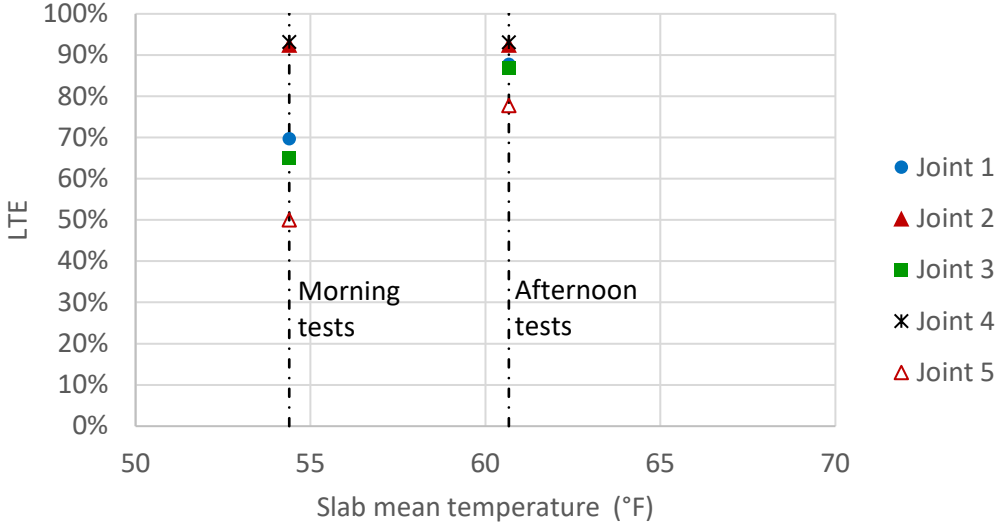


**Figure 8.16: Example of LTE variation versus slab temperature (FWD Section B-N3, Winter 2019-20 evaluation).**

Using the same example (FWD Section B-N3), the LTE measured in all FWD evaluations is shown in Figure 8.17. The LTE-temperature trend observed for any particular deployed joint (Joint 1, Joint 3, or Joint 5) in the winter does not match the trend observed in the summer. Consequently, a direct relationship between slab mean temperature and LTE does not exist. Other researchers, however, have found a good correlation between LTE and slab mean temperature in different seasons (15,19).

This study attempted to predict LTE using the slab longitudinal strain measured with VWSGs instead of the mean temperature. Because the slab longitudinal strain is a direct measure of slab expansion/contraction, which is linearly related to transverse joint opening, it was expected that using the slab longitudinal strain would explain diurnal and seasonal variations of LTE better than the mean

temperature of the slabs. Unfortunately, that was not the case, so a direct relationship does not exist between transverse joint opening and LTE. The same outcome was obtained for the FWD sections.

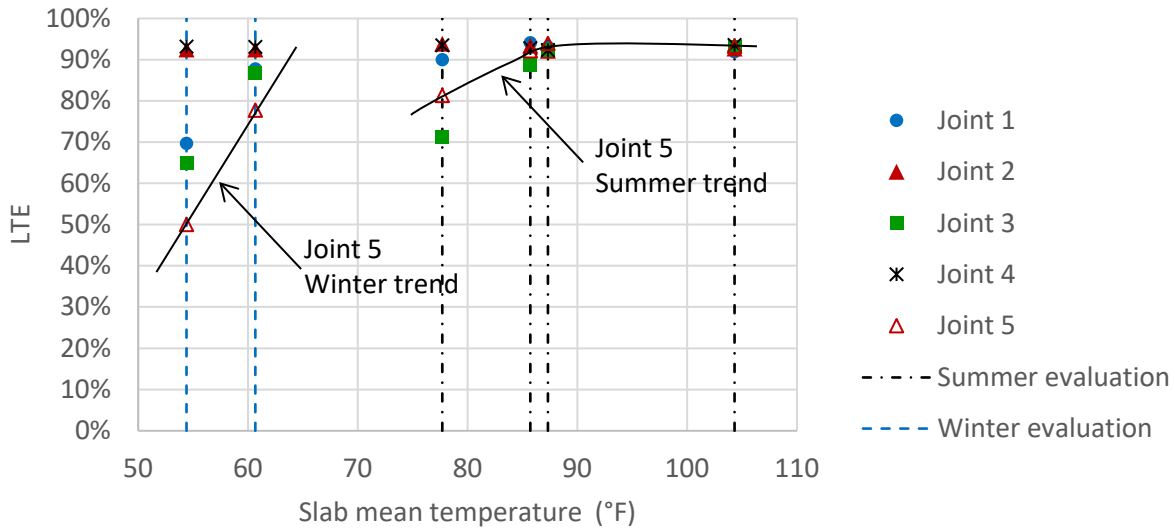


**Figure 8.17: Example of LTE variation versus slab temperature (FWD Section B-N3).**

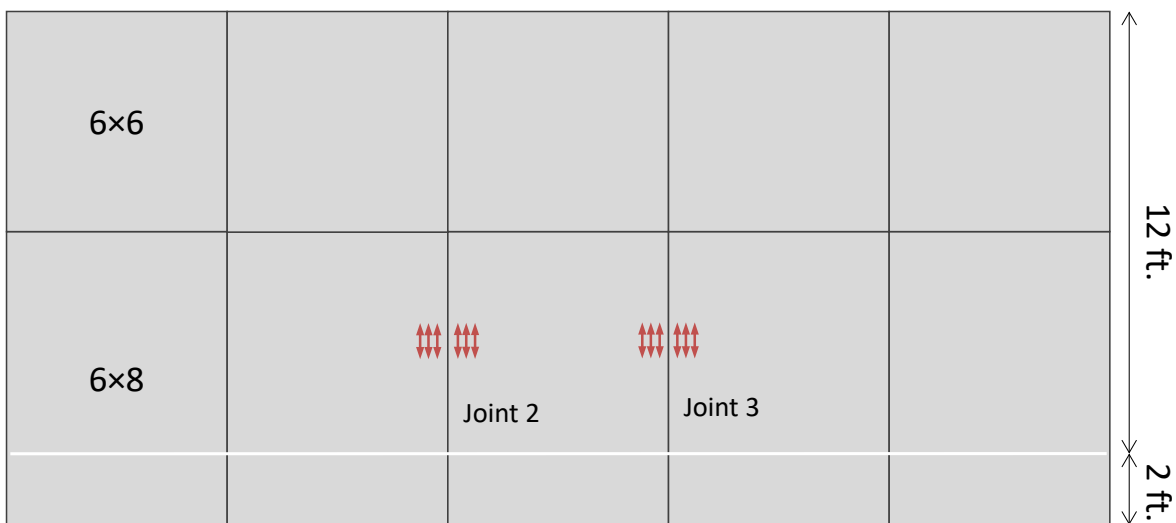
#### 8.4 Evaluation of the Thin COA Sections Under Truck Loading


The structural capacity of the thin COA was periodically evaluated under truck loading, an evaluation referred to as real load testing (RLT). The RLT evaluations had four main goals:

- Determine structural differences between sections (Figure 2.1) and RLT evaluations (Summer 2019, Winter 2019-20, and Summer 2020). The differences between RLT evaluations may indicate changes in the structural capacity of the COA. This goal is discussed in Section 8.2.3.
- Evaluate the structural contribution of the asphalt base bonded to the concrete slabs. This goal is discussed in Section 8.2.4.
- Determine if the COA structure responded to truck loading as expected. This goal is discussed in Section 8.2.5.
- Estimate the concrete cracking safety factor by comparing the estimated concrete tensile stresses under truck loading versus the estimated concrete tensile strength. This goal is discussed in Section 8.2.6.

### 8.4.1 Real Load Testing Evaluations

The Woodland SR 113 thin COA sections were instrumented with resistive strain gauges to measure the structural response under traffic loading. The strain gauges were installed at several depths, shown in Figure 8.18. This instrumentation was installed at four locations, two in Section A2 and two in Section A3, shown in Figure 8.19. Each of the locations is referred to in this report as an instrumented point (IP). IP A21, IP A22, IP A31, and IP A32 correspond to the FWD Sections A-NB 2, 3, 4, and 5, respectively (Table 8.1).<sup>1</sup>



-  3 SG:
  - 1 in. below slab surface
  - 1 in. above slab bottom
  - Interface RHMA-G/Old HMA (only in Section A2: Instrumented points 21 & 22)

**Figure 8.18: Instrumentation layout.**

<sup>1</sup> The instrumentation installation is described in previous UCPRC research (3).

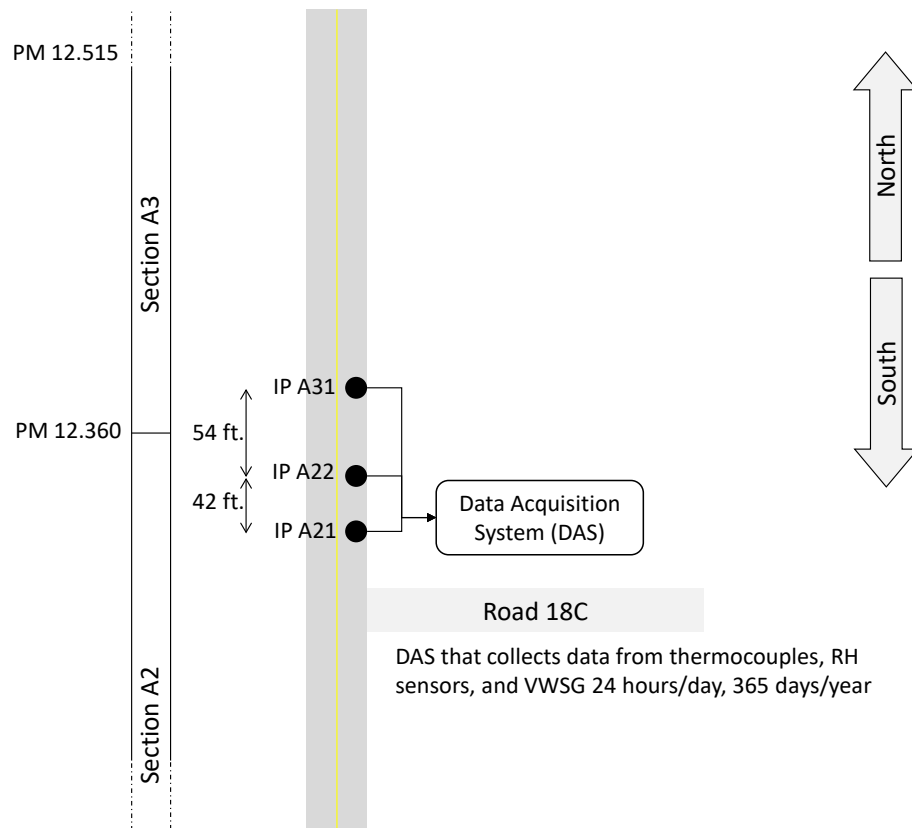


**Figure 8.19: Location of instrumented points (IP).**

Three RLT evaluations were conducted, during which a truck with known axle weights ran multiple times over the instrumented points. The dates of the three RLT evaluations are shown in Table 8.3.

**Table 8.4: Real Load Testing Evaluation Dates**

Real Load Testing (RLT) Evaluation	Date
Summer 2019	August 7, 2019
Winter 2019-20	January 31, 2020
Summer 2020	August 18, 2020

The same truck model with a similar load was used for the three RLT evaluations (Figure 8.20). The truck has three single axles. The three single axles were each weighed with a portable scale. The weights of the three axles (steering, drive, and truck axles) were around 9.6, 20.6, and 19.1 kips, respectively. The offset (the distance between the wheel edge and white strip) was measured by using a tape measure placed on the pavement surface, shown in Figure 8.20. An operator standing by the test sections recorded the offset of each truck pass. The majority of the passes were conducted at 45 mph.



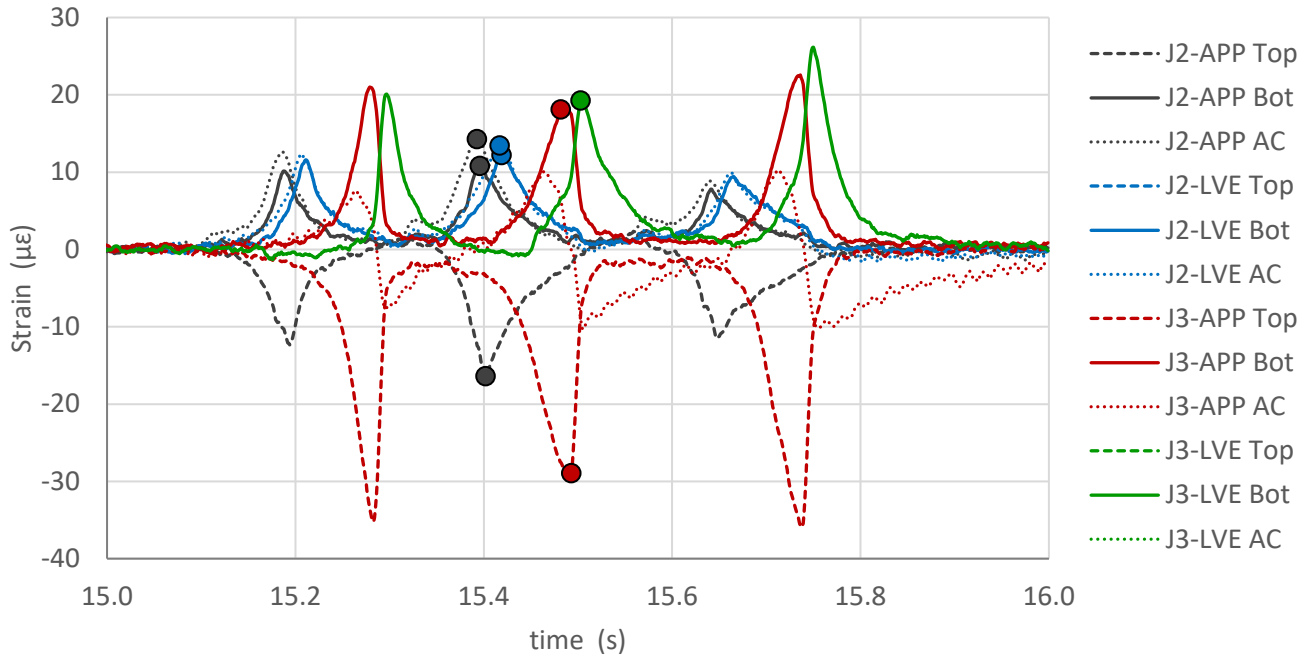


**Figure 8.20: Experiment truck passing over instrumented slab (IP A21).**

In each of the three RLT evaluations, between 80 and 110 truck passes were recorded starting early in the morning (around 8:00 a.m.) and ending late in the afternoon (around 5:00 p.m.). The goal of testing during a relatively long time period was to capture the effects of changes in the slab temperature profile. The resistive strain gauge data were recorded with two National Instruments portable data acquisition systems—one for IP A21, IP A22, and IP A31 and one for IP A32. The slab temperature data were collected by a Campbell Scientific permanent data acquisition system (Figure 8.19).

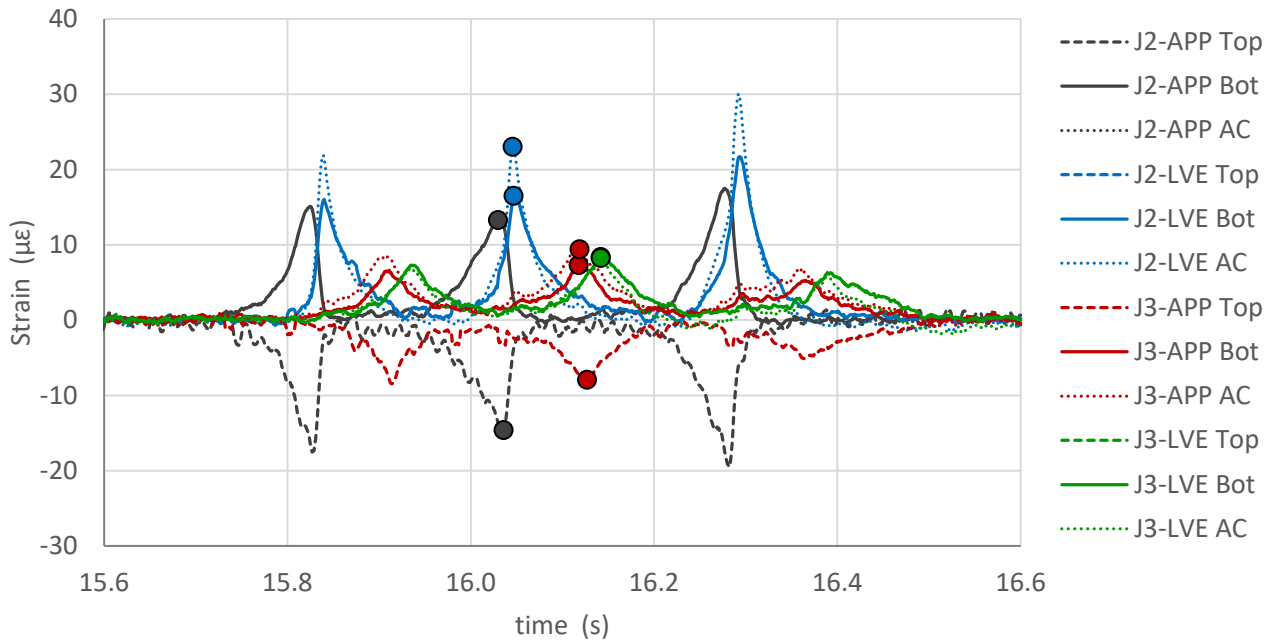
#### **8.4.2 Processing of Strain Data**

Figure 8.21 includes an example of the data collected with the resistive strain gauges installed at IP A21. The example corresponds to truck pass number 1 from the Summer 2019 evaluation. In the series labels, the number after “J” is the joint number (the location of each joint shown in Figure 8.18). “APP” refers to the approach side of the joint and “LVE” refers to the leave side of the joint. The gauge depths are indicated by “Top” and “Bot,” the slab top and bottom, and “AC,” the asphalt base. The three pulses observed for each gauge in Figure 8.21 correspond to the three axles of the truck. The peak values of the second pulse (the drive axle of the truck) are marked with circles. Figure 8.22, Figure 8.23, and Figure 8.24 include examples that correspond to IP A22, IP A31, and IP A32, respectively.



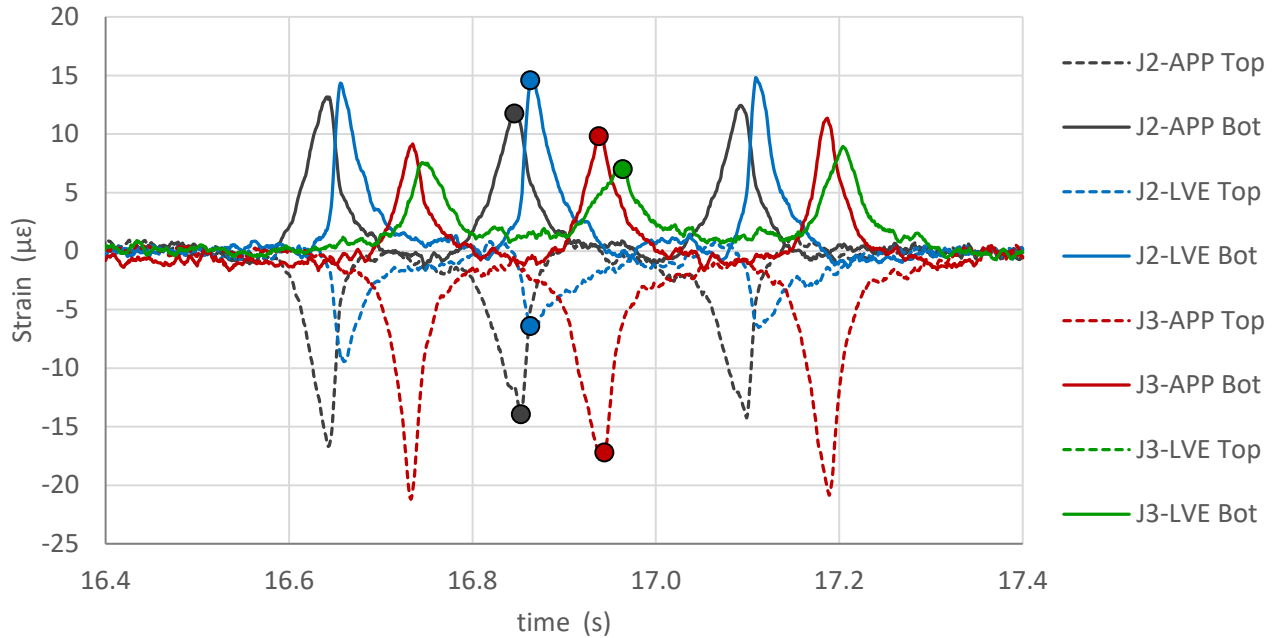
Notes: Series name includes joint number (after “J”), location (APP or LVE for approach or leave side of the joint, respectively), and depth (top [Top] or bottom [Bot] of the slab).

**Figure 8.21: Example of data collected with resistive strain gauges (Section A2, IP A21, Pass 01, Summer 2019).**



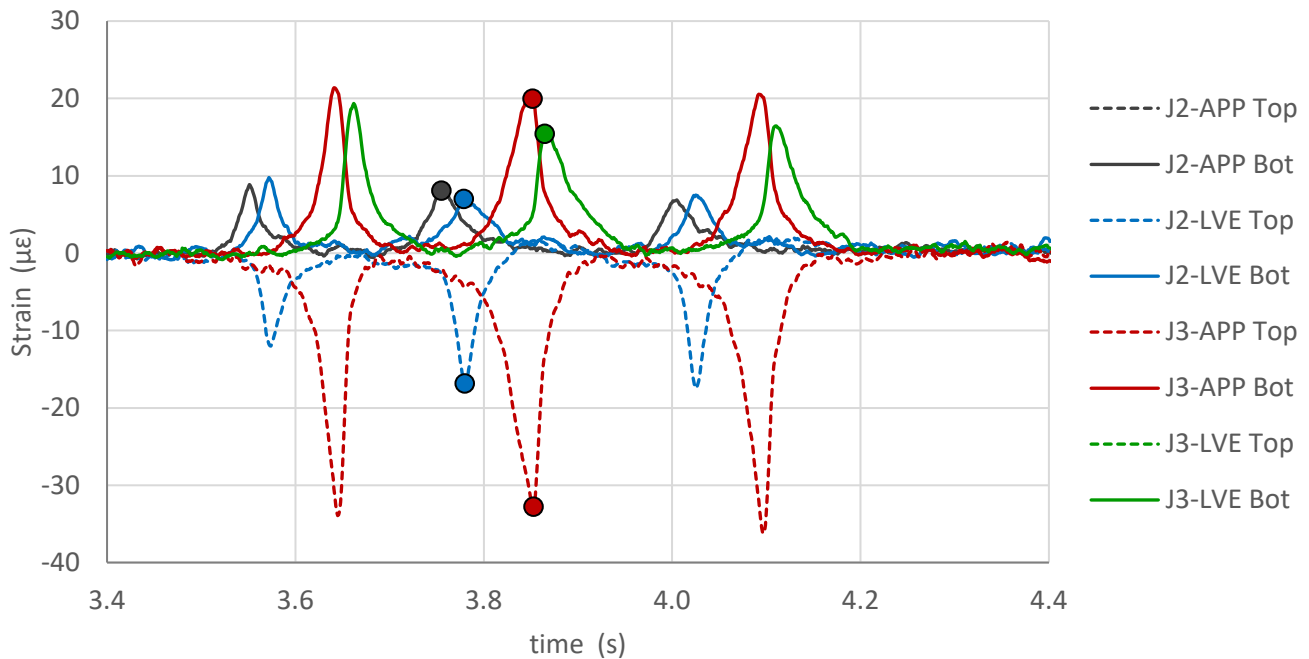
Notes: Series name includes joint number (after “J”), location (APP or LVE for approach or leave side of the joint, respectively), and depth (top [Top] or bottom [Bot] of the slab).

**Figure 8.22: Example of data collected with resistive strain gauges (Section A2, IP A22, Pass 01, Summer 2019).**



Notes: Series name includes joint number (after “J”), location (APP or LVE for approach or leave side of the joint, respectively), and depth (top [Top] or bottom [Bot] of the slab).

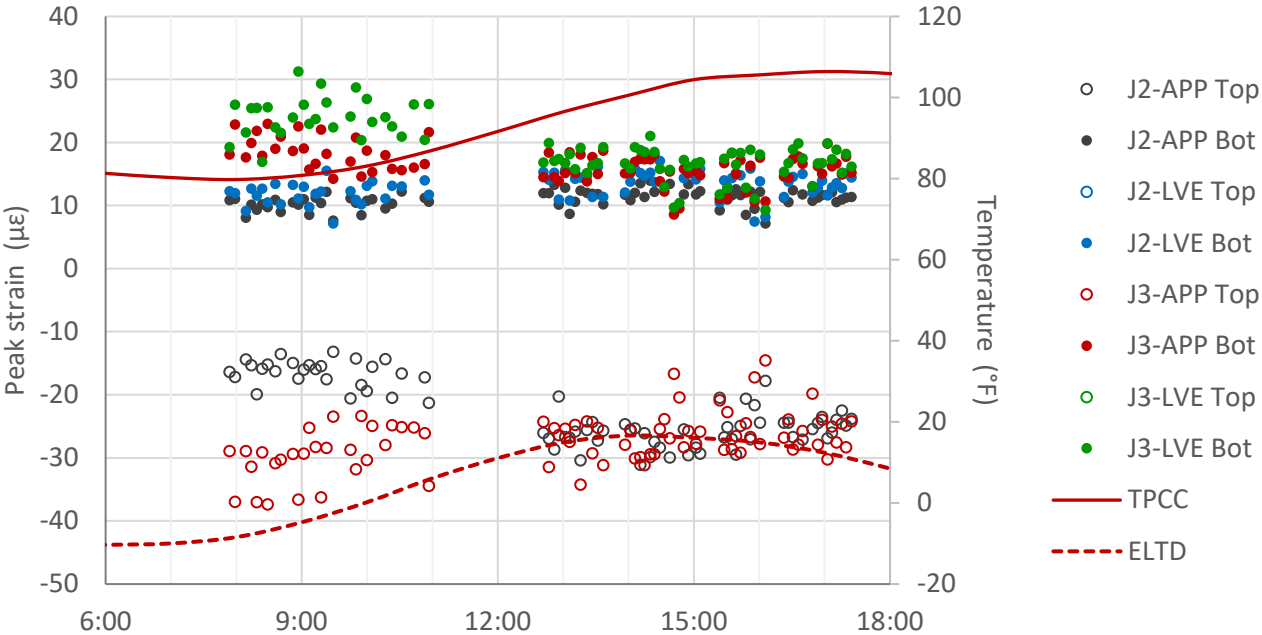
**Figure 8.23: Example of data collected with resistive strain gauges (Section A3, IP A31, Pass 01, Summer 2019).**



Notes: Series name includes joint number (after “J”), location (APP or LVE for approach or leave side of the joint, respectively), and depth (top [Top] or bottom [Bottom] of the slab).

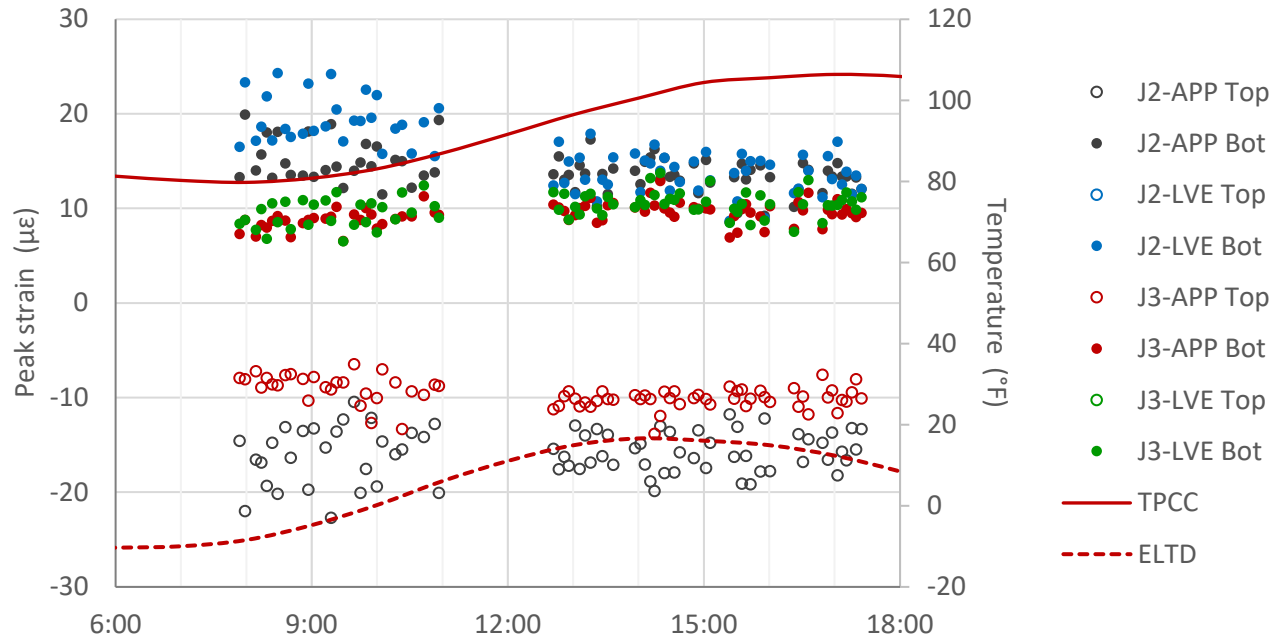
**Figure 8.24: Example of data collected with resistive strain gauges (Section A3, IP A32, Pass 33, Summer 2019).**

The first step in the data analysis included the extraction of the peak values that corresponded to the truck’s drive axle (the second pulse in Figure 8.21 to Figure 8.24). As examples, the peak values extracted for the different instrumented points in the Summer 2019 evaluation are shown in Figure 8.25 to Figure 8.29. Also shown are the mean temperature of the portland cement concrete (TPCC) slabs and the equivalent linear temperature difference (ELTD). TPCC and ELTD are determined from the temperature measured with the thermocouples installed at different depths in the concrete slabs.



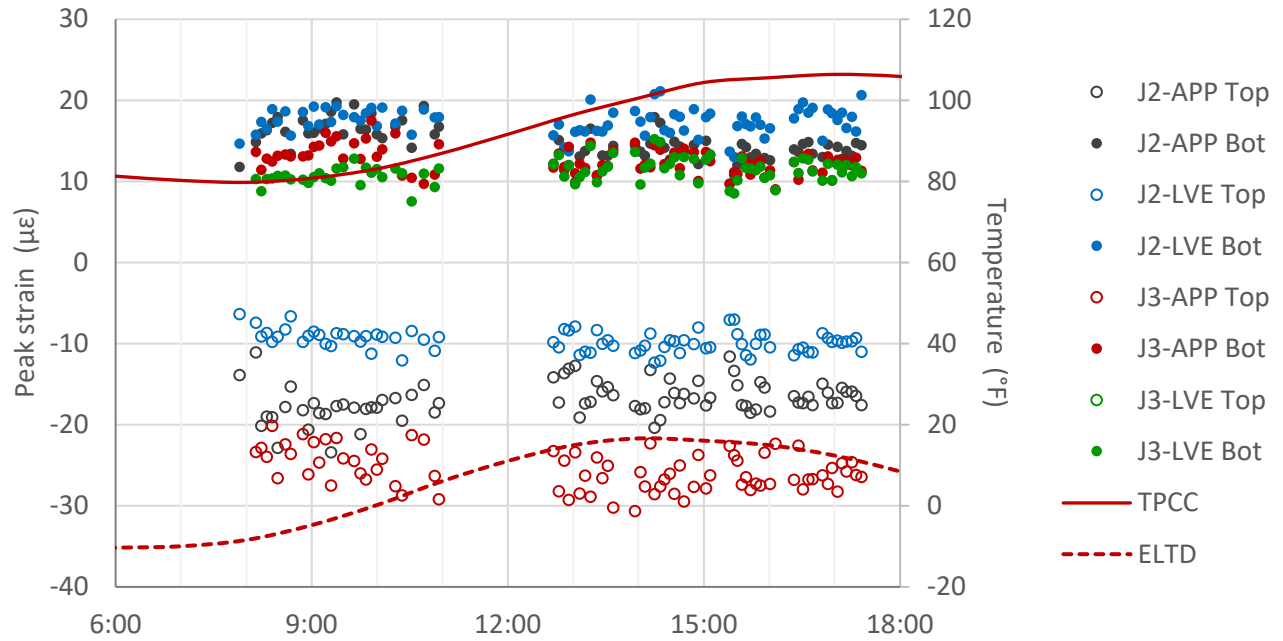
Notes: For clarity, the strain measured in the asphalt base has been omitted from the figure; hollow circles are at slab top, filled circles at slab bottom. Series name includes joint number (after “J”), location (APP or LVE for approach or leave side of the joint, respectively), and depth (top [Top] or bottom [Bot] of the slab).

**Figure 8.25: Peak strain registered under the drive axle of the truck (Section A2, IP A21, Summer 2019).**



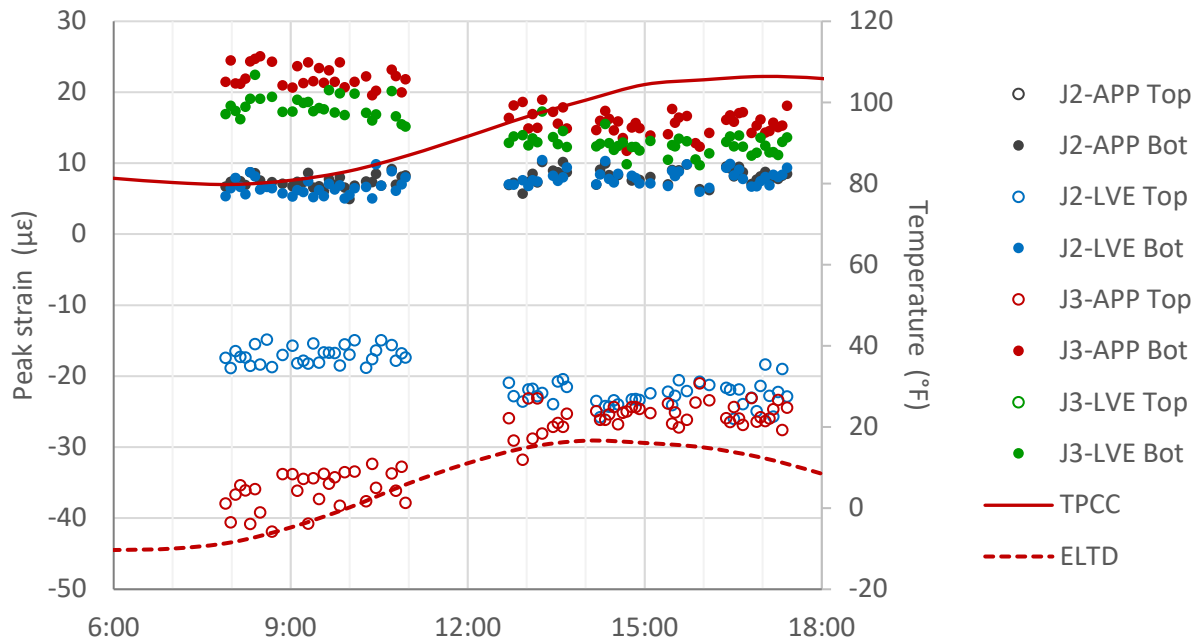
Notes: For clarity, the strain measured in the asphalt base has been omitted from the figure; hollow circles are at slab top, filled circles at slab bottom. Series name includes joint number (after “J”), location (APP or LVE for approach or leave side of the joint, respectively), and depth (top [Top] or bottom [Bot] of the slab).

**Figure 8.26: Peak strain registered under the drive axle of the truck (Section A2, IP A22, Summer 2019).**



Notes: Series name includes joint number (after “J”), location (APP or LVE for approach or leave side of the joint, respectively), and depth (top [Top] or bottom [Bot] of the slab).

**Figure 8.27: Peak strain registered under the drive axle of the truck  
(Section A3, IP A31, Summer 2019).**



Notes: Series name includes joint number (after “J”), location (APP or LVE for approach or leave side of the joint, respectively), and depth (top [Top] or bottom [Bot] of the slab).

**Figure 8.28: Peak strain registered under the drive axle of the truck (Section A3, IP A32, Summer 2019).**

Based on the approach described in Section 8.1.5, only one of every two transverse joints deployed at IP A21 and IP A22. The different performance of deployed and undeployed joints can be clearly seen in Figure 8.25 (IP A21) and Figure 8.26 (IP A22). Early in the morning, when slab temperature is low and the LTE of the deployed joints is poor, the strain measured at the deployed joints (Joint 3 in IP A21 and Joint 2 in IP A22) is higher than the strain measured at the undeployed joints. During the day, as the slab temperature and the LTE of the deployed joints increase, the strain measured at the deployed joints decreases in absolute value. At the same time, as the slab ELTD increases (the slab curls concave downward), the strain measured at the undeployed joints increases in absolute value. At the end of the day, the strains measured at the two types of joints converge. A similar pattern is shown for IP A32 in Figure 8.28 despite all its transverse joints having deployed.

Once the peak values were extracted, a linear regression model was used to fit the measured peaks with each of the gauges in the three RLT evaluations. For example, six models were used to fit the data shown in Figure 8.28, one for each of the gauges. The TPCC, ELTD, and wheel offset variables were included in the regression model. Once fitted, the models were used to estimate three characteristic

peak values: morning, midday (when ELTD = 0), and afternoon. The morning value corresponds to the slab thermal conditions of the morning, when the RLT started; the midday value corresponded to the time of the day when ELTD is zero; and the afternoon value corresponded to the slab thermal conditions that existed at the end of the RLT. A wheel offset of 3 ft. (the center of the dual wheel is 3 ft. from the white strip) was adopted for determining the characteristic values. For the Summer 2019 RLT evaluation (Figure 8.25 to Figure 8.28), slab thermal conditions were 80°F TPCC and -8.4°F ELTD in the morning, 83°F TPCC and 0°F ELTD at midday, and 106°F TPCC and +8.5°F ELTD in the afternoon. These characteristic values were used in the analysis presented in the following section.

### **8.4.3     *Structural Differences Between Sections and Evaluations***

Three types of transverse joints were present in the SR 113 thin COA:

1. Deployed joints with good LTE
2. Deployed joints with poor LTE
3. Undeployed joints

The types of joint present at the different instrumented locations, shown in Figure 8.29, were determined based on FWD testing, following the approach described in Section 8.1.5, and partially validated with coring.



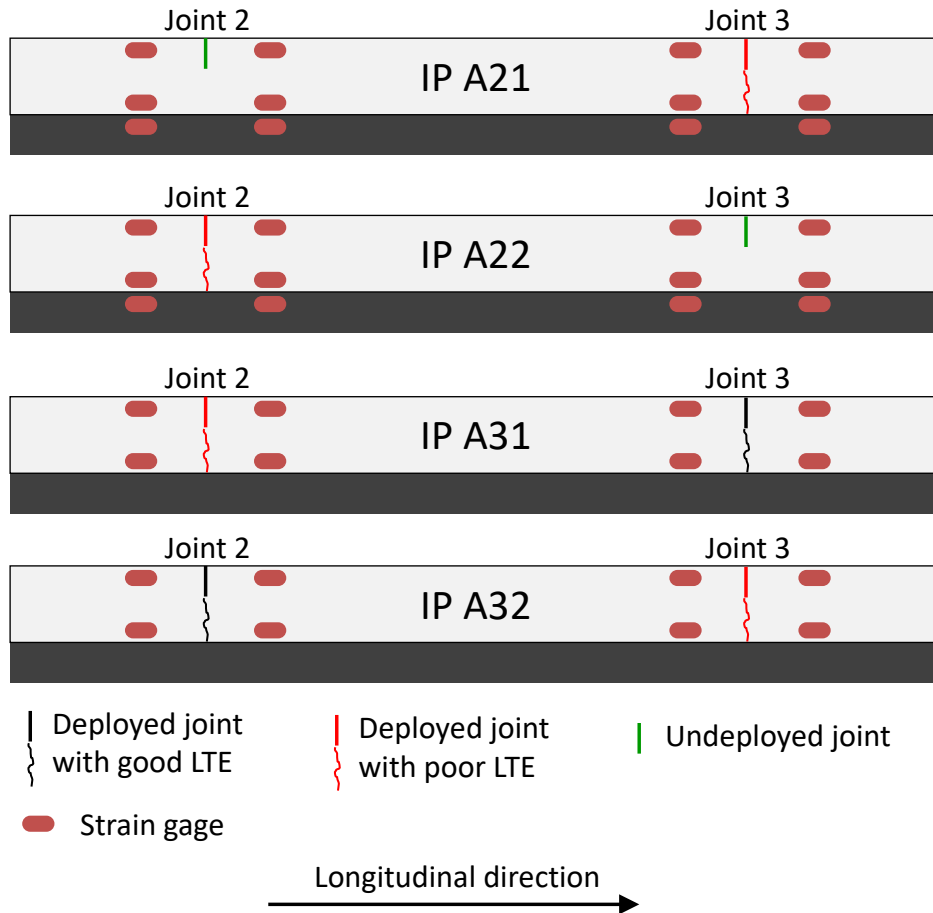
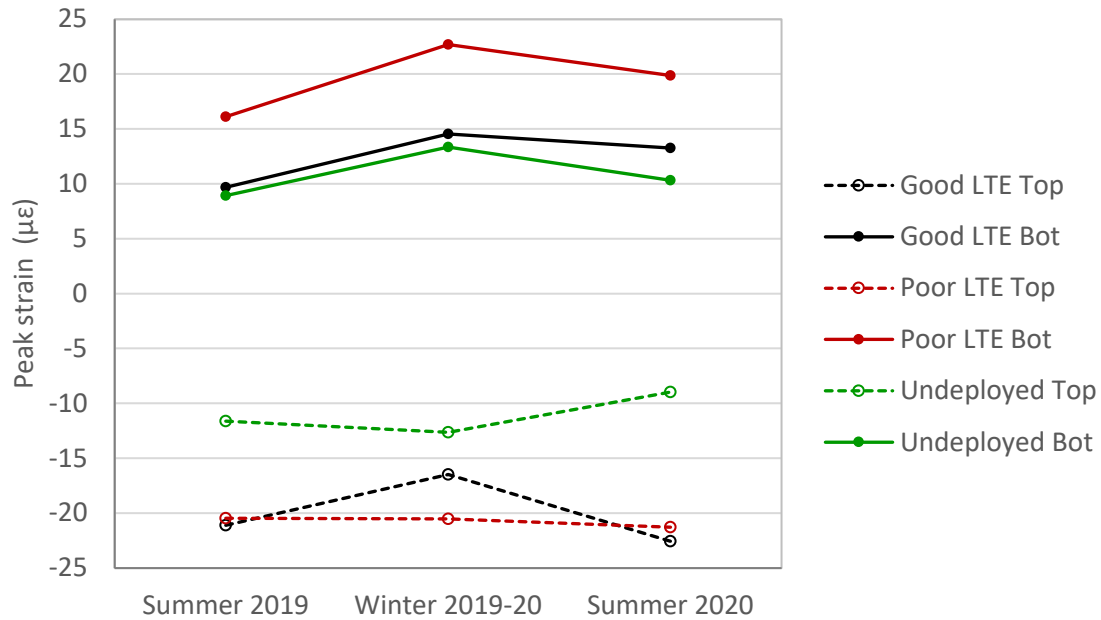


**Figure 8.29: Layout of the different types of joints.**

The midday (ELTD = 0) peak strain measured for each joint type in the three RLT evaluations is shown in Figure 8.30. Each series is the average of all joints of the same type in the four instrumented points. No distinction is made between sections since the ANOVA indicated that the differences between the two sections (IP A2 versus IP A3) were not statistically significant.



Notes: Positive strain is tension; negative strain is compression.

**Figure 8.30: Midday (ELTD = 0) peak strain registered under truck second axle.**

The ANOVA of the midday (ELTD = 0) peak strain measured at the bottom of the concrete slabs (the series ending in “Bot” in Figure 8.30) indicates the following:

- The effects of RLT time (Summer 2019, Winter 2019-20, and Summer 2020) and type of joint (good LTE, poor LTE, and undeployed) are statistically significant. Figure 8.31 shows the ANOVA table (the joint type factor is “LTE2”). Similar ANOVA conducted for the strain measured at the top of the slabs indicates that the joint type effect is statistically significant but the RLT effect is not.
- The strain at the deployed joints (good and poor LTE) increases about 3 to 4 µε between Summer 2019 and Summer 2020. This increase is related to the loss of some strain gauges between the two evaluations. The ANOVA indicates that the differences are not statistically significant. This finding suggests that the structure of the COA had not changed considerably between Summer 2019 and Summer 2020.

### Tests of Between-Subjects Effects

Dependent Variable: Val2

Source	Type III Sum of Squares	df	Mean Square	F	Sig.
Corrected Model	816.651 <sup>a</sup>	8	102.081	12.040	.000
Intercept	8334.277	1	8334.277	982.999	.000
RLT	190.669	2	95.335	11.244	.000
LTE2	657.456	2	328.728	38.772	.000
RLT * LTE2	12.627	4	3.157	.372	.827
Error	288.266	34	8.478		
Total	10696.100	43			
Corrected Total	1104.918	42			

a. R Squared = .739 (Adjusted R Squared = .678)

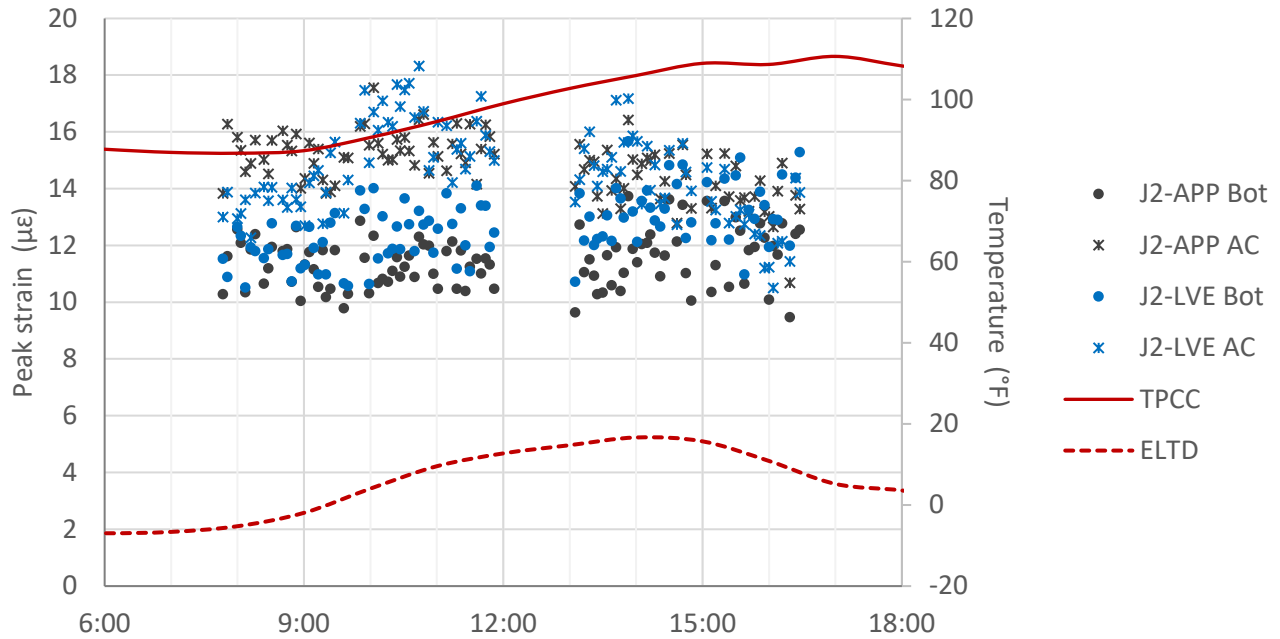
**Figure 8.31: ANOVA table of midday (ELTD = 0) peak strain registered under truck second axle at the bottom of the concrete slabs.**

#### **8.4.4 Evaluation of the Structural Contribution of the Asphalt Base**

The bonding between concrete slab and asphalt base can be evaluated by comparing the strains that the truck loading produces at the top of the asphalt base and the bottom of the concrete slabs. The strain in the asphalt must be of a magnitude similar to, or higher than, the strain at slab bottom if these two layers are bonded. This comparison could be conducted for the SR 113 Section A2 because this section was instrumented with strain gauges located at the interface between the old milled HMA and the new RHMA-G (Figure 2.1). Two instrumented points were located in Section A2 (IP A21 and IP A22).

Only one of every two transverse joints deployed at IP A21 and IP A22 and, consequently, two types of transverse joints were present: undeployed joints and deployed joints with poor LTE (Figure 8.29). The strain measured in the asphalt base differed between the two types of joints. At the undeployed joints, the asphalt strain was higher than the concrete strain in the three RLT evaluations, shown in the Figure 8.32 example. The four asphalt strain gauges located at the undeployed transverse joints of IP A21 and IP A22 showed this outcome, which indicates good bonding and that the concrete slab and base are acting as a monolithic composite section. In contrast, three of the four strain gauges located at the transverse joints with poor LTE registered either compression peaks or erratic strain under the

truck pass. This finding indicates that the slab and asphalt base were not bonded, which corresponds with the concrete-asphalt debonding present in the coring of the joints with poor LTE.



Notes: Series name includes joint number (after “J”), location (APP or LVE for approach or leave side of the joint, respectively), and depth (bottom [Bot] is slab bottom and AC is asphalt concrete base).

**Figure 8.32: Comparison between peak strains registered under truck second axle at slab bottom and asphalt base (Section A2, IP A21, Summer 2020)**

The structural contribution of the asphalt base bonded to the concrete slab can be evaluated by comparing the strains that the truck loading produces at the top and bottom of the concrete slab. If the structural contribution of the asphalt base bonded to the slab is significant, the strain at the bottom of the slab must be of a smaller magnitude than the strain at the top of the slab. Overall, the strains measured in the SR 113 thin COA sections at slab the top and bottom were similar to each other in absolute value, regardless of joint type. On average, the strain at the bottom of the slabs was 83% of the strain at the top. This finding indicates that the structural contribution of the asphalt base bonded to the concrete slabs is not much and corresponds with the poor condition of the asphalt base that remained after the milling operation (3).

#### **8.4.5 Modeling Thin COA Structural Response Under Truck Loading**

The structure of thin COA is typically modeled as slabs resting on a liquid foundation. This modeling can be conducted by using general purpose finite element method (FEM) programs such as *Abaqus* or FEM programs specifically developed for concrete pavements such as *ISlab*. The *ISlab2005* program was used to model the Woodland SR 113 thin COA. The goal of the modeling was to determine if the strain measured in the COA matched the expected values. Differences between the measured and predicted strains may indicate structural deficiencies of the COA, among other things.

The *ISlab2005* model's parameters were set as follows:

- Concrete stiffness: 5.4, 5.9, and 6.1 million psi for the Summer 2019, Winter 2019-20, and Summer 2020 evaluations, respectively. These values are based on laboratory testing of the concrete sampled during the construction of the overlay.
- Asphalt stiffness: 400,000 psi, regardless of the season. This value is based on FWD testing conducted before asphalt milling.
- Concrete CTE:  $5.2 \mu\epsilon/^\circ\text{F}$ . This value is based on laboratory testing of the COA mixture.
- Concrete thickness: 5.5 to 7.0 in., with a 6 in. average. These values are based on coring conducted after the COA construction (3).
- Asphalt thickness: 1 to 6 in., with a 3 in. average. These values are based on coring conducted after the COA construction (3).
- Modulus of subgrade reaction: 250 pci. This value is based on FWD testing.
- Concrete-asphalt bonding: fully bonded.
- Transverse joints load transfer efficiency: 99% (*ISlab* definition) for joints with good LTE and variable (depending on concrete temperature) for joints with poor LTE. An LTE of 99% in *ISlab* is roughly equivalent, for this particular COA structure, to 92% LTE with the FWD testing definition.<sup>2</sup>
- Load: 20,600 lb. single axle with dual wheels (weight of the drive axle of the RLT truck).
- Built-in curling:  $-10^\circ\text{F}$  ELTD.

---

<sup>2</sup> FWD LTE is equal to deflection at 12 in. radial distance divided by deflection under the load plate.

Because concrete and asphalt thicknesses varied considerably along the project, three modeling scenarios were considered:

- Average thickness: 6 in. concrete slab and 3 in. asphalt base. This scenario is referred to as “Model” in the following figures.
- Low strain: 7 in. concrete slab and 6 in. asphalt base. This scenario is referred to as “Model↓” in the following figures.
- High strain: 5.5 in. concrete slab and 1 in. asphalt base. This scenario is referred to as “Model↑” in the following figures.

The three types of joints (good LTE, poor LTE, and undeployed) were modeled independently. No section distinction was made since the only difference between the sections was the type of asphalt in the top 1.5 in. of the base (new RHMA-G in Section A2 and old HMA in Section A3) and the impact of this difference is minimal. This assumption corresponds with the fact that the ANOVA did not show statistically significant differences between the two sections.

The comparison between the model and measured strains is presented in Figure 8.33 for joints with good LTE and in Figure 8.34 for joints with poor LTE. The comparison for undeployed joints is shown in Figure 8.35. In the three cases, the measured strain fell within the range predicted by the model (Model↓ to Model↑). While Figure 8.31 to Figure 8.33 correspond to the first RLT evaluation, Summer 2019, the same outcome was obtained for the rest of the evaluations.

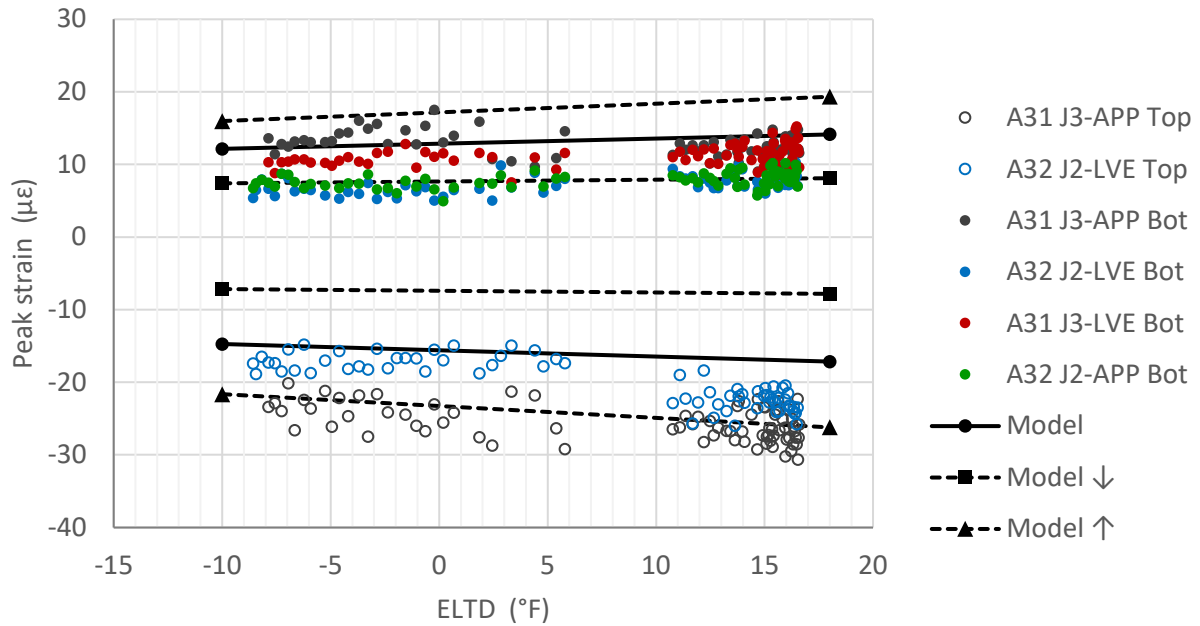
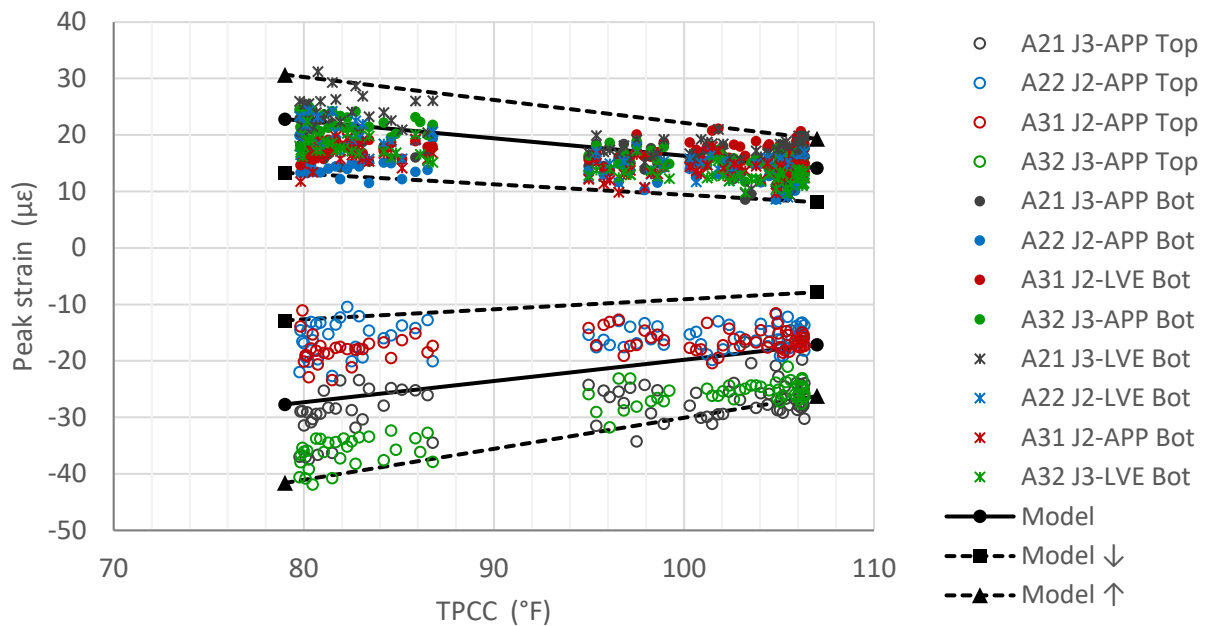


**Figure 8.33: Comparison between model and measured peak strain for joints with good LTE (Summer 2019).**



Note: TPCC (temperature portland cement concrete) is the mean temperature of the slabs.

**Figure 8.34: Comparison between model and measured peak strain for joints with poor LTE (Summer 2019).**

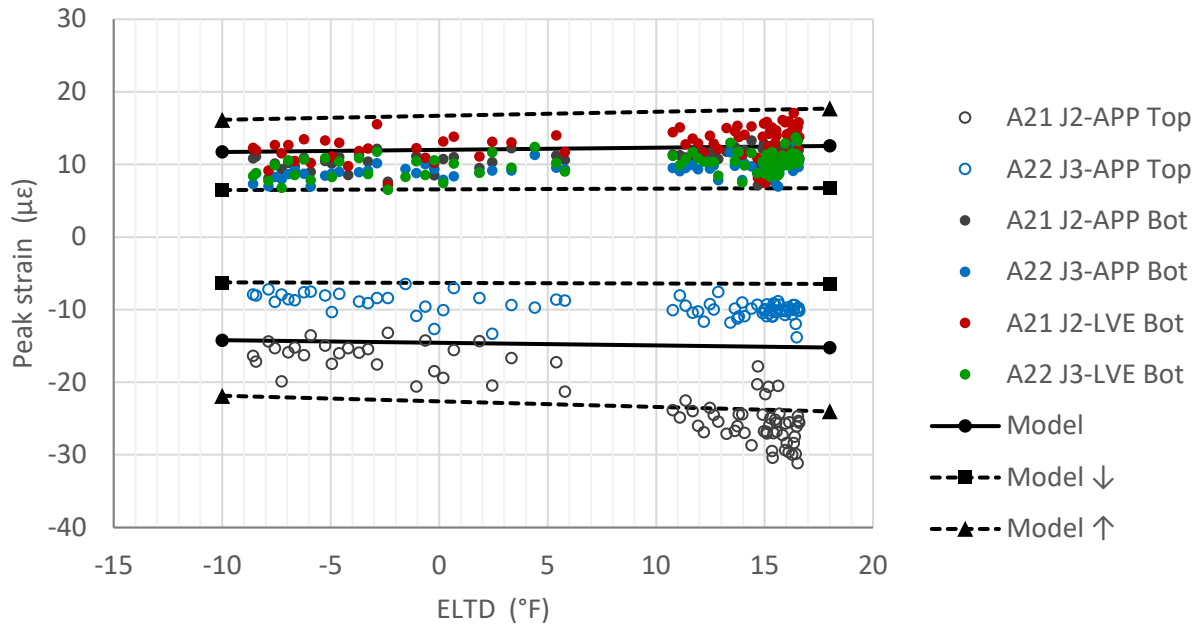


**Figure 8.35: Comparison between model and measured peak strain for undeployed joints (Summer 2019).**

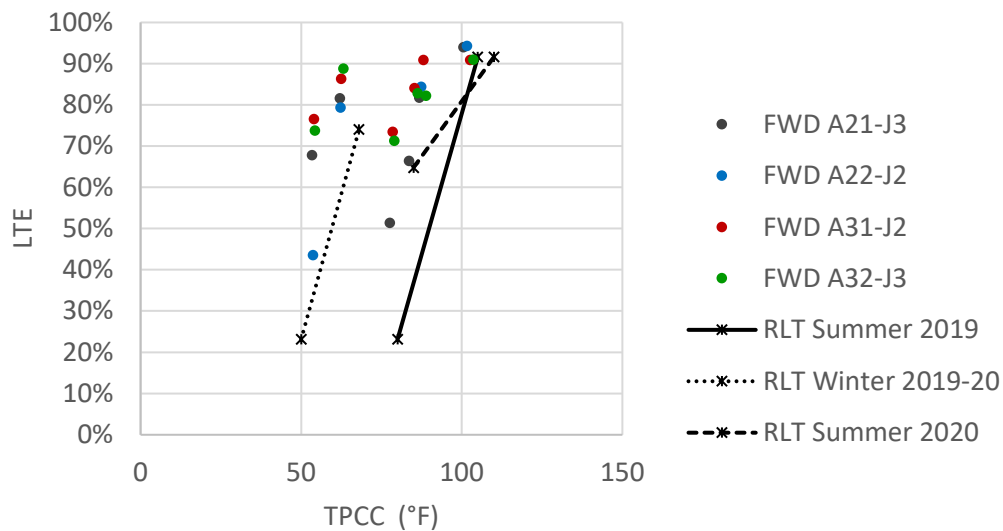
As shown in Figure 8.31 to Figure 8.33, the strain measured at joints with good LTE and undeployed joints is plotted versus ELTD while the strain measured at joints with poor LTE is plotted versus TPCC (temperature portland cement concrete—i.e. mean temperature of the slabs). ELTD is an indication of slab curvature, and slab curvature affects the strain measured at the transverse joints under truck loading. The higher the ELTD (the more the slabs are curled concave downward), the higher the strain (in absolute value) under truck loading. TPCC is an indication of slab expansion-contraction, which affects the LTE of the transverse joints. The higher the TPCC, the higher the LTE and the lower the strain (in absolute value) under truck loading. The effect of TPCC is minimal on the joints with good LTE since the LTE is always high, and this is why the strain at these joints is plotted versus ELTD (Figure 8.33 and Figure 8.35). On the contrary, the effect of TPCC on the LTE of the joints with poor LTE is very high, and this is why the strain at these joints is plotted versus TPCC (Figure 8.34).

The LTE of transverse joints with poor LTE was determined in a trial-and-error iteration process with *ISLab2005*. The goal of the iteration process was to match the strain measured in the field. For the Summer 2019 data shown in Figure 8.34, the *ISLab2005* transverse joints LTE had to be set to 25% in order to match the strains measured at the 80°F slab temperature (early morning). This LTE



corresponds to around 23% of the LTE based on the FWD testing definition of LTE. Meanwhile, the LTE had to be set to 99% in order to match the strains measured at 108°F slab temperature (late afternoon). A similar process was followed with the other two RLT evaluations.

Figure 8.36 includes a comparison between the LTE measured in the FWD testing at the joints with poor LTE and the LTE determined from the strain measured under truck loading using the approach described previously. It is clear that the FWD testing considerably overestimates the effective LTE of the transverse joints under truck loading.



Note: TPCC (temperature portland cement concrete) is the mean temperature of the slabs.

**Figure 8.36: Comparison between FWD LTE and effective LTE under truck loading for joints with poor LTE.**

#### 8.4.6 Monte Carlo Simulation of the Concrete Tensile Stresses Under Truck Loading

The strain that truck loading creates at the bottom of the concrete slabs can be regarded as a function of axle loading and slab thermal conditions (TPCC and ELTD) with a random component. The random component represents the variability between slabs of the SR 113 thin COA and can be estimated by considering the gauge-to-gauge variability, which can be seen in many of the figures previously presented (for example, in Figure 8.33 to Figure 8.35).

The modeling and experimental data indicate that truck loadings produce maximum stresses in the SR 113 thin COA when TPCC (slab mean temperature) reaches minimum values. This outcome is due to the fact the LTE of the transverse joints with poor LTE decreases as the TPCC decreases. The minimum TPCC registered during the first year of the SR 113 thin COA was 40°F. The measured strain can be extrapolated to this specific temperature by using the linear regression models that were calibrated to the data for each strain gauge (Section 8.4.2). This extrapolation results in an estimation of the strain that the truck second axle (20.6-kip single axle) would produce in the slabs under such unfavorable thermal conditions (TPCC = 40°F). These strain values can be used to estimate the distribution of the tensile stresses that truck loading produces at the bottom of the slabs.

A Monte Carlo simulation was conducted to simulate the pass of a 22-kip single axle (10% overloading) on SR 113 during the coldest expected conditions (i.e., when TPCC = 40°F). Some details of the simulation include the following:

- Strain at the bottom of the concrete slabs is assumed to be normally distributed. Strains at the joints with good and poor LTE are estimated independently of each other.
- Strain at the bottom of the slabs under the 20.6-kip single axle when TPCC equals 40°F:
  - Joints with good LTE: 27.1  $\mu\epsilon$  average and 5.6  $\mu\epsilon$  standard deviation
  - Joints with poor LTE: 11.0  $\mu\epsilon$  average and 6.1  $\mu\epsilon$  standard deviation
- Strain under the 22-kip single axle is assumed to be the strain under the 20.6-kip truck second axle multiplied by 22/20.6.
- Concrete age is assumed to be one year.
- Concrete flexural strength is assumed to be normally distributed with a 950 psi average and 68.6 psi standard deviation. These values are based on laboratory testing of the concrete mixture at the one-year age.
- Concrete modulus of elasticity is assumed to be 6.0 million psi based on laboratory testing of the concrete mixture at the one-year age.
- The number of random slabs generated is 1,000. Strain under truck loading changes from one slab to the next. Concrete flexural strength also changes from one slab to the next.

The outcome of the Monte Carlo simulation, presented in Figure 8.37, is the distribution of the tensile stresses at the bottom of the slabs when the 22-kip single axle runs on SR 113 thin COA during very cold weather. Tensile stresses in the figure have been corrected by the actual flexural strength of the concrete ( $\text{stress} \cdot \text{FS} / 950$ , where FS is the flexural strength of each slab) so that they can be directly compared to the 950 psi average flexural strength. The tensile stresses are below 50% the flexural strength of the concrete, even under the unfavorable conditions assumed in the Monte Carlo simulation that included a 10% overloaded axle and the minimum slab temperature expected in the SR 113 thin COA.

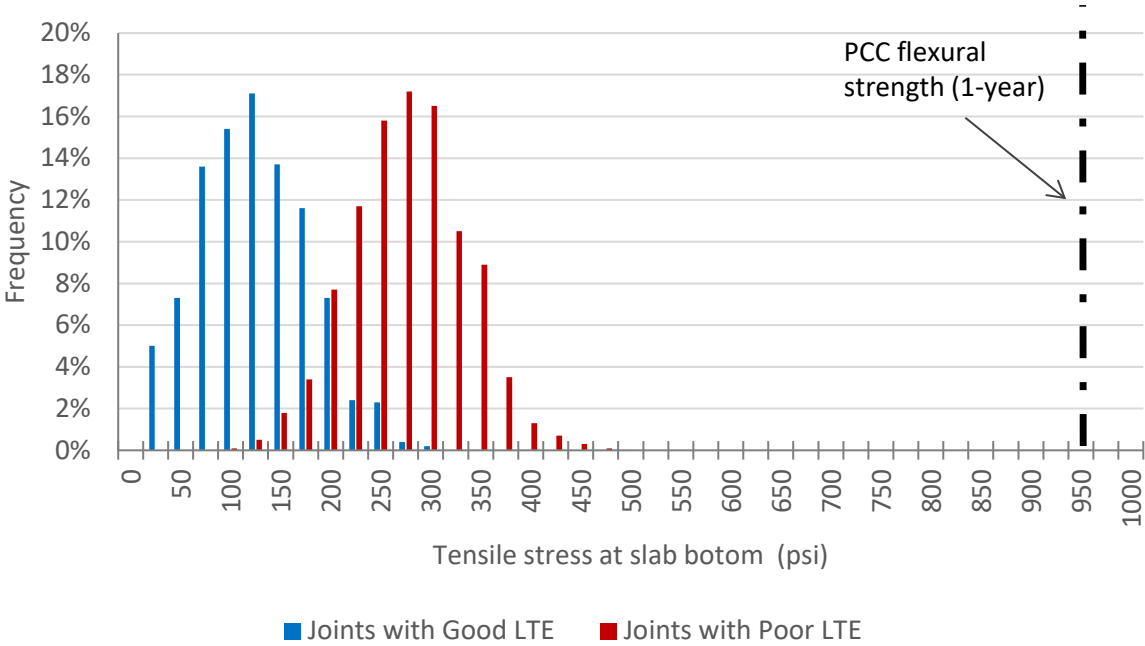


**Figure 8.37: Monte Carlo simulation of 22-kip single axle running on SR 113 thin COA during minimum TPCC conditions (TPCC = 40°F, 1-year age)**

## 9 CONCLUSIONS AND RECOMMENDATIONS

---

This report presents the initial performance (for around 18 months) of the Woodland SR 113 thin COA project. The performance was evaluated by different means, including periodic visual inspections and longitudinal profiler evaluations; FWD testing; real load testing (RLT), where the concrete strains under truck loading were recorded; and continuous monitoring of slab temperatures and drying shrinkage deformations.

### 9.1 Conclusions

The main conclusion from the evaluation of the initial performance of the SR 113 thin COA is that no structural damage has taken place. This conclusion is supported by the following findings:

- Visual inspection of the COA did not indicate any cracking, faulting, or any other structural distress.
- While the smoothness varied considerably during the period evaluated in this report, the variation was caused by changes in slab curvature due to thermal gradients through the slab depth and concrete drying shrinkage.
- FWD deflections and LTE remained stable between the August 2019 and August 2020 evaluations.
- The structural response of the COA under truck loading remained stable between the August 2019 and August 2020 evaluations.

Other important conclusions from the initial evaluation of SR 113 thin COA performance include the following:

- The visual inspection did not find any material-related distress or slab migration.
- The smoothness of the concrete overlay indicates high diurnal and seasonal variations. The diurnal variation was caused by changes in slab curvature due to thermal gradients, and the seasonal variation was caused by changes in slab curvature due to concrete drying shrinkage.
  - The IRI changed up to 40 in./mi during a 24-hour period.
  - The IRI changed close to 60 in./mi during one year.

- Calculations based on *ProVAL* and slab curvature measurements with VWSGs correspond with the high diurnal and seasonal variations of the IRI measured in the SR 113 thin COA.
- The differential drying shrinkage (top versus bottom of the slab) reached very high values, up to 800  $\mu\epsilon$ , in the Woodland COA slabs. Considering that the CTE of the concrete was 5.2  $\mu\epsilon/^\circ\text{F}$  (under saturated conditions, AASHTO T 336), the ELTD that matches such differential shrinkage is 150 $^\circ\text{F}$ .
- The strain measured with VWSGs in the SR 113 thin COA slabs indicates that the slabs are restricted from expanding in the longitudinal direction during the warm periods. The restriction was more severe during the second summer (2020) than during the first summer (2019).
- The surface macrotexture, quantified as MPD, was around 23 mils after the construction of the concrete overlay, which was later textured with longitudinal tining. The macrotexture increased to around 30 mils after the blanket grinding and then decreased slowly due to the traffic action.
- The LTE of the transverse joints showed a clear high-low pattern with alternating joints with good and poor LTE.
  - While the LTE of the joints with good performance remains stable over 80%, the LTE of the joints with poor performance show a strong seasonal variation and the LTE is highly affected by the mean temperature of the slabs.
  - Around 30% of the joints with poor performance show less than 70% LTE during the winter evaluation.
  - The LTE high-low pattern is partly related to the lack of deployment of some transverse joints.
  - FWD testing, complemented with visual inspection and coring, indicates that around 80% of the transverse joints deployed. The joints seemed to deploy soon after the overlay construction, and FWD testing suggests that no further transverse joint deployment occurred after the first summer.
  - The lack of transverse joint deployment is partly related to the low ratio of saw-cut depth to slab thickness, attributable to the extra thickness of the slab above the design

thickness and a relatively shallow cut. The coring conducted at three locations indicates that the ratio was between 0.22 and 0.25 (smaller than the one-third target).

- In addition to the lack of deployment of some transverse joints, the LTE high-low pattern seems to be related to a more general phenomenon: the presence of dominant joints that absorb the opening of the adjacent joints (deployed or not deployed). Because of its larger opening, a dominant joint would show smaller LTE than the adjacent joints.
  - Visual inspection of the initial transverse joint deployment indicates that the dominant joints deployed earlier than the adjacent joints.
  - While the northbound and southbound lanes were paved on different days, the location of the dominant joints in the two lanes match. The matching indicates that the opening and closing of the first-paved lane transverse joints triggered the deployment of the second-paved lane transverse joints.
- FWD testing and RLT do not indicate differences between the SR 113 sections other than slightly smaller deflections in Segment B compared to Segment A, due to its higher slab thickness. However, both FWD testing and RLT indicate statistically significant differences between joints with good and poor LTE.
  - The analysis of the strain measured in SR 113 thin COA sections under RLT indicates that the COA structure is performing as expected, considering the LTE high-low pattern and the lack of deployment of some of the transverse joints. Based on the measured strain, the LTE of the joints with poor LTE is much lower than the LTE measured with the FWD at the same joints.
  - The analysis of the RLT strain data indicates that the structural contribution of the asphalt base bonded to the concrete slab is very little. On average, the absolute value of the strain measured under track loading at the bottom of the slabs is 83% of the absolute value of the strain measured at the top of the slabs.
  - Visual examination of cores, supported with the analysis of the RLT strain data, indicates that debonding occurred at the transverse joints with poor LTE. The debonding extended around 10 to 20 in. away from the transverse joints regardless of the type of asphalt base. In the sections with rubberized gap-graded hot mix asphalt (RHMA-G) base, the debonding occurred around 0.2 to 0.4 in. below the top of the RHMA-G surface. This indicates that the upward movement

of the slab from the large thermal and drying shrinking curling effects resulted in tensile stresses in the RHMA-G that were greater than its tensile strength, which was less than the tensile strength of the concrete/RHMA-G bond. In the sections with old HMA base, the debonding took place at the concrete-asphalt interface.

- The pass of a 22-kip single axle (10% overloaded) was simulated with the Monte Carlo simulation approach. The simulation indicated that the COA tensile stresses are below 50% the flexural strength of the concrete at the one-year age, despite the simulation assuming the lowest slab temperature (40°F) expected in the SR 113 thin COA, which resulted in the lowest expected performance of the transverse joints.
- The analysis of the strain measured in SR 113 thin COA sections under RLT indicates that the FWD testing considerably overestimates the effective LTE of the transverse joints under truck loading.

## 9.2 Recommendations

The following recommendations are based on the evaluation of the initial performance of the SR 113 thin COA:

- Consider the use of SRA, as a concrete admixture, in COA projects in dry climate regions. The use of this admixture is expected to reduce drying shrinkage to 50%, which will have a positive impact on smoothness seasonal stability and will diminish the risk of concrete cracking and transverse joint faulting.
- Closely monitor saw-cutting operations to ensure the ratio between saw-cut depth and slab thickness does not fall below one-third, particularly when the overlay thickness is at the top of the 4 to 7 in. range typically used in COA.
- Consider delaying the post-construction blanket grinding operation, if this operation is needed, until one full summer has passed. Slab curvature variations due to drying shrinkage will diminish after the first drying cycle.
- Monitor seasonal variation of the IRI in other COA pilots in the Caltrans road network.
- Evaluate transverse joint LTE in other COA pilots in the Caltrans road network to determine if the LTE high-low pattern observed in the SR 113 thin COA is also present in these other pilots.

- The use of tie bars and the effect of slab thickness could not be evaluated in the Woodland SR 113 thin COA pilot. It is recommended that future Caltrans COA pilots evaluate the effect of these two design variables.



## 10 REFERENCES

---

1. Mateos, A., Harvey, J.T., Paniagua, F., Paniagua, J., and Wu, R. 2019. *Development of Improved Guidelines and Designs for Thin Whitetopping: Summary, Conclusions, and Recommendations* (UCPRC-SR-2018-01). Davis and Berkeley, CA: University of California Pavement Research Center. [escholarship.org/uc/item/5g04q2mb](https://escholarship.org/uc/item/5g04q2mb).
2. Mateos, A., Harvey, J.T., Paniagua, F., Paniagua, J., and Wu, R. 2019. "Accelerated Testing of Full-Scale Thin Bonded Concrete Overlay of Asphalt." *Transportation Research Record* 2673, no. 2: 404–414.
3. Mateos, A., Harvey, J.T., Millan, M.A., Wu, R., Paniagua, F., Cisneros, J., and Paniagua, J. 2021. *Concrete Overlay on Asphalt Pilot Project at Woodland SR 113: Construction* (UCPRC-RR-2020-01). Davis and Berkeley, CA: University of California Pavement Research Center. [escholarship.org/uc/item/86f4f3sr](https://escholarship.org/uc/item/86f4f3sr).
4. California Department of Transportation. n.d. "Caltrans Pavement Climate Regions." Accessed November 10, 2020. [dot.ca.gov/-/media/dot-media/programs/maintenance/documents/office-of-concrete-pavement/climate/pavement-climate-regions-100505-a11y.pdf](https://dot.ca.gov/-/media/dot-media/programs/maintenance/documents/office-of-concrete-pavement/climate/pavement-climate-regions-100505-a11y.pdf).
5. Burnham, T. 2019. "Early Loading Pavement Research at MnROAD and NRRRA." Presented at Spring 2019 National Concrete Consortium Conference, Denver, CO, April 2–4, 2019.
6. Miller, J.S. and Bellinger, W.Y. 2014. *Distress Identification Manual for the Long-Term Pavement Performance Program* (FHWA-HRT-13-092). Washington, DC: Federal Highway Administration. [fhwa.dot.gov/publications/research/infrastructure/pavements/ltp/13092/13092.pdf](https://fhwa.dot.gov/publications/research/infrastructure/pavements/ltp/13092/13092.pdf).
7. Mateos, A., Harvey, J.T., Wu, R., Paniagua, F., and Paniagua, J. 2020. *Development of Improved Guidelines and Designs for Thin Whitetopping: Environmental Response of Full-Scale BCOA Sections* (UCPRC-RR-2017-03). Davis and Berkeley, CA: University of California Pavement Research Center. [escholarship.org/uc/item/14t4f662](https://escholarship.org/uc/item/14t4f662).
8. Mateos, A., Harvey, J.T., Bolander, J., Wu, R., Paniagua, J., and Paniagua, F. 2019. "Field Evaluation of the Impact of Environmental Conditions on Concrete Moisture-related Shrinkage and Coefficient of Thermal Expansion." *Construction and Building Materials* 225: 348–357.
9. Mateos, A., Harvey, J.T., Bolander, J., Wu, R., Paniagua, J., and Paniagua, F. 2020. "Structural Response of Concrete Pavement Slabs Under Hygrothermal Actions." *Construction and Building Materials* 243: 118261.
10. Meyers, S.L. 1951. "How Temperature and Moisture Changes May Affect the Durability of Concrete." *Rock Products* 54, no. 8: 153–162.
11. Jeong, J.H., Zollinger, D.G., Lim, J.S., and Park, J.Y. 2012. "Age and Moisture Effects on Thermal Expansion of Concrete Pavement Slabs." *Journal of Materials in Civil Engineering* 24, no. 1: 8–15.

12. Chang, G., Rasmussen, R., Merritt, D., Garber, S., and Karamihas, S. 2010. *Impact of Temperature Curling and Moisture Warping on Jointed Concrete Pavement Performance* (FHWA-HIF-10-010). Washington, DC: Federal Highway Administration. [fhwa.dot.gov/pavement/concrete/pubs/hif10010/hif10010.pdf](http://fhwa.dot.gov/pavement/concrete/pubs/hif10010/hif10010.pdf).
13. Chang, G., Karamihas, S., Rasmussen, O., Merritt, D., and Swanlund, M. 2008. "Quantifying the Impact of Jointed Concrete Pavement Curling and Warping on Pavement Unevenness." Presented at the 6th Symposium on Pavement Surface Characteristics, Portoroz, Slovenia, October 20–23, 2008.
14. Karamihas, S.M., and Senn, K. 2012. *Curl and Warp Analysis of the LTPP SPS-2 Site in Arizona* (FHWA-HRT-12-068). Washington, DC: Federal Highway Administration. [fhwa.dot.gov/publications/research/infrastructure/pavements/ltp/13040/13040.pdf](http://fhwa.dot.gov/publications/research/infrastructure/pavements/ltp/13040/13040.pdf).
15. Rufino, D.M. 2003. "Mechanistic Analysis of In-Service Airfield Concrete Pavement Responses." PhD diss. University of Illinois at Urbana-Champaign. [ideals.illinois.edu/items/84505](http://ideals.illinois.edu/items/84505).
16. King, D. and Roesler, R. 2014. "Backcalculation Procedure for Bonded Concrete Overlays of Asphalt Pavement." *Transportation Research Record* 2457: 72–79.
17. Mateos, A., Harvey, J.T., Wu, R., Paniagua, F., and Paniagua, J. Forthcoming. *Development of Improved Guidelines and Designs for Thin Whitetopping: HVS Testing of Full-Scale BCOA Sections* (UCPRC-RR-2017-06). Davis and Berkeley, CA: University of California Pavement Research Center.
18. Voigt, Gerald E. 2002. "Early Cracking of Concrete Pavement — Causes and Repairs." Presented at 2002 Federal Aviation Administration Airport Technology Transfer Conference.
19. Harvey, J.T., Kohler, E., Santero, N., Bian, Y., Mancio, M., and Cruz, C. *Summary Report on Dowel Bar Retrofit for Rigid Pavements* (Summary Report: UCPRC-SR-2008-03). Davis and Berkeley, CA: University of California Pavement Research Center.